Spark Assisted Chemical Engraving: A Novel Approach for Quantifying the Machining Zone Parameters Using Drilling Forces

Jana Daher Abou Ziki

A Thesis
In the Department
of
Mechanical and Industrial Engineering

Presented in Partial Fulfillment of the Requirements
For the Degree of
Doctor of Philosophy (Mechanical and Industrial Engineering) at
Concordia University
Montreal, Quebec, Canada

CONCORDIA UNIVERSITY
SCHOOL OF GRADUATE STUDIES

This is to certify that the thesis prepared

By: Jana Daher Abou Ziki

Entitled: Spark Assisted Chemical Engraving: A Novel Approach for Quantifying the Machining Zone's Parameters Using Drilling Forces

and submitted in partial fulfillment of the requirements for the degree of

Doctor of Philosophy (Mechanical Engineering)

complies with the regulations of the University and meets the accepted standards with respect to originality and quality.

Signed by the final examining committee:

Dr. R. Glitho — Chair

Dr. P. Koshy — External Examiner

Dr. S.S. Li — External to Program

Dr. P. Wood-Adams — Examiner

Dr. A. Dolatabadi — Examiner

Dr. G. Cusanelli — Examiner

Dr. R. Wuthrich — Thesis Supervisor

Approved by: _____
Dr. A. Dolatabadi , Graduate Program Director

June 26, 2014

_____
Dr. C. Trueman, Interim Dean
Faculty of Engineering and Computer Science

Abstract

Spark Assisted Chemical Engraving: A Novel Approach for Quantifying the Machining Zone Parameters Using Drilling Forces

Jana Daher Abou Ziki, Ph.D
Concordia University, 2014

Glass has stirred human interest since the dawn of history due to its unique properties including its high mechanical strength, transparency, thermal and chemical properties. With the great technological advancement that we are witnessing today in the micro-technology field, glass micro-machining has already found applications in the optical, electronics, and biomedical applications. In fact, such applications require high-aspect-ratio structures of defined wall flatness and surface roughness.

There exist nowadays several glass micro-machining technologies that are being developed to meet this demand. These are based on thermal (laser), chemical (dry and wet etching), and mechanical (ultrasonic, abrasive and diamond-tool drilling) processes. Spark Assisted Chemical Engraving (SACE) is a non conventional glass micro-machining technology which is based on discharge generation at the tool tip. This is known to heat up the glass surface. Today, the machining mechanism is highly questionable where it is explained differently by many researchers in the field. This is due to the fact that the basic understanding about the process and the local variables in the machining zone is still missing. Although research about SACE drilling has allowed achieving deeper and smaller holes, these results remain specific to certain machining conditions. In fact, they are achieved experimentally by trial and error due to limited knowledge about the process fundamentals. Therefore, it can be said that SACE machining is still blind where the idea of doing feed-back drilling has not

been explored sufficiently. These are the basic reasons of why SACE glass machining remains in laboratories and is never applied in industry.

The aim of this work is to unveil basic information about the SACE machining process and the local parameters in the machining zone. For this purpose, a methodology is developed for measuring the local machining zone parameters based on the force exerted on the tool during machining. Measurement errors caused by tool bending, wear and thermal expansion are quantified and considered while measuring and analysing the machining forces. Thus, in a first step, the machining force is characterized and analysed to get a deeper understanding about its origin and the reasons of its formation. This signal is used in a second step to extract information about local variables including the machining gap size, the local glass surface temperature and the origin of its texture. Based on the understanding of the machining process that this work brings, a thermal model is built which describes heat transfer to the glass surface. The agreement between calculations and measurements ensures the validity of both the model and measurement methodology. Based on the results, the machining mechanism is explained as a thermal assisted etching process. Machining can exist in two modes based on the electrolyte state (aqueous or molten) which depends on the local flushing. Force signal readings showed that tool-glass bonding can occur during machining which may hinder the drilling progress. Based on the understanding that this work brought about the machining mechanism and the factors that influence it, force feedback algorithms are built with the aim to establish a balance between local heating and flushing. The efficiency of the various algorithms in enhancing the drilling performance was compared and assessed based on the resulting drilling time. The knowledge acquired allowed building algorithms that succeeded in drilling high-aspect-ratio holes up to 1:9 while using very small tools (70 μm diameter) without breakage. The resulting drilling time is dramatically reduced to few seconds compared to several minutes in the state-of-the-art SACE drilling.

Acknowledgements

I take the opportunity to acknowledge the support and assistance of the people who had faith in this work and without which this thesis would not have been as much successful.

Deserving of special mention is my supervisor, Professor Rolf Wüthrich, who believed in my work and gave me his trust to lead my research in the direction I was comfortable with. Your guidance, knowledge, and help were instrumental in the advancement of my research.

A great thank you goes to Posalux SA and their team especially Dr. Giuseppe Cusanelli, the Technology Manager, and Mr. Philippe Grize, the Chief Operation Officer, for their financial and moral support. I am as well grateful to the Natural Sciences and Engineering Research Council (NSERC) and the Fonds de recherche du Québec-Nature et technologies (FQRNT) for their financial support.

I would like to thank my colleagues, especially Lucas Hof and Andrew Morrison, for the useful project discussions. Also I thank the technicians Gilles Huard and Robert Oliver for their aid in resolving technical issues in the machine set-up.

A big thank you goes to my mother, Lydia, for motivating me throughout my graduate studies and for her efforts to always maintain a comfortable study and working atmosphere for me at home. Your support is priceless mom! I would also like to send a warm-hearted thank you to my dad, Daher, and my brothers, Maen and Nassir, for the tremendous energy they gave me towards pursuing my studies with big success and for helping me get over the difficulties I encountered during this period of my life. You've been my inspiration.

Last but not least, a deep thank you from the bottom of my heart goes to my husband, Firas, for always being there for me, for his endless love, understanding and encouragement. I am grateful to have you in my life...

Jana Daher Abou Ziki

To my parents and to my husband I dedicate this work.

Contents

List of Figures

List of Tables

List of Symbols

Latin Symbols

a_1, a_2	Length of the horizontal plate
b	Width of the hinge
B	Flexible structure damping
B_{cl}	Closed loop damping
C	Tool tip heat capacitance
C_p	Specific heat of the work-piece
d	Tool diameter
D	Controller's derivative term
e	Thickness of the hinge
E	Material's modulus of elasticity
f	Tool feed-rate
$f_a(t)$	Force exerted on the structure by the voice-coil actuator
F	Drilling force
g	Machining gap
I	Current flowing between the electrodes
$\bar{I}$	Mean current
I_A	Moment of inertia of the flexible structure
I^{crit}	Critical current
I_d	Mean discharge amplitude
k_φ	Hinge's angular stiffness
K	Flexible structure stiffness
K_{cl}	Closed loop stiffness
K_{tool}	Tool stiffness
L	Tool length
L_o	Tool length dipped in the electrolyte
M	Flexible structure mass
n_d	Mean number of discharges per time

p	Etching rate
P	Controller's proportional term
P_{min}	Minimum heat required to machine
P_o	Heat transferred to the glass surface
q_i	Heat generated by the discharges
r	Tool radius
r_h	Radius of the hinge
R	Equivalent thermal resistance of R_{liq} and R_{tool}
R_g	Thermal resistance inside the machining gap
R_l	Electrolyte thermal resistance
R_{tool}	Tool thermal resistance
t_o	Time needed to heat the glass surface
T	tool temperature
T_M	Glass machining temperature
T_a	Ambient temperature
T_{ME}	Electrolyte salt's melting point
U	Machining voltage
U^{crit}	Critical voltage
U_d	Water decomposition potential
z	Motion of the tool-electrode fixation
Z	Motion of the Z-stage (depicting as well the hole depth)
Z_o	Arbitrary origin of the coordinate system
Z_i	Position where the work-piece surface is detected
z_i	Depth at which the middle region starts

Greek Letters

ΔL	Change in tool length
ΔT	change in tool temperature
Δx	Distance between two consecutive tori
Δy	Torus height
α	Work-piece thermal diffusivity
α_l	Tool coefficient of linear expansion
ζ	Damping ratio
η	Work-piece viscosity
κ	Normalized heat power
λ	Work-piece thermal conductivity

λ_g	Thermal conductivity of the material inside the machining gap
λ	Work-piece thermal conductivity
λ_l	Electrolyte thermal conductivity
λ_{tool}	Tool thermal conductivity
ρ	Work-piece density
ρ_{tool}	Tool-electrode density
σ_{tool}	Tool specific heat
τ_d	Mean discharge duration
φ	Angular motion
ω_o	Flexible structure eigenfrequency
ω_{cl}	Closed loop frequency

Acronyms

CNC	Computer Numerical Control
EDM	Electrical Discharge Machining
ECM	Electro Chemical Machining
ECAM	Electro Chemical Arc Machining
ECDM	Electro Chemical Discharge Machining
ECSM	Electro Chemical Spark Machining
MEMS	Micro-Electro-Mechanical Systems
PD	Proportional-Derivative
PID	Proportional-Integral-Derivative
SACE	Spark Assisted Chemical Engraving
SEM	Scanning Electron Microscope
WEDG	Wire Electro Discharge Grinding

Chapter 1

Introduction

When you follow your bliss...
doors will open where you would not
have thought there would be doors; and
where there wouldn't be a door for anyone else.
(-Joseph Campbell)

Glass, which exists in its natural form since millions of years ago, is one of the most complex as well as the most interesting materials present on our planet. It is commonly agreed that glass is a material on the frontier between ordered and disordered matter. Its unique properties including its transparency, chemical resistance and high mechanical strength and thermal resistivity make it suitable for several applications. With the current flow of technology towards component miniaturization, fabrication of micro-devices, some of which require glass components, has become essential. Glass is the preferable material to be used in micro-total-analysis-systems (μTAS) applications due to its optical transparency compared to silicon (Daridon et al., 2001). Its properties make it a suitable for manufacturing photonics devices like optical wave-guides and interconnects and for manufacturing components for watches and electrical circuits requiring through glass via (TGV). Moreover, it enters into the fabrication of micro-fluidic devices (Wu et al., 2013) including biomedical ones where it is the mostly used substrate for manufacturing DNA arrays (Khan Malek et al., 2007). Glass is also a promising material for power delivering devices like micro-solid oxide fuel cells (Evans et al., 2009).

Intense research has been devoted for micro machining structures on glass substrates where several technologies are being developed for this purpose. There exists several glass micro-machining technologies nowadays. These can be divided into thermal (laser), chemical (etching) and mechanical (ultrasonic and abrasive machining). However, each of these

techniques has its own limitations. Laser micro-machining is fast in terms of machining time but has the problem of heat affected zones and surface cracks (Thoe et al., 1998) and of obtaining flat walls (Babnik et al., 2013). Etching by HF is highly hazardous and requires special facilities. In addition, chemical etching techniques are slow and expensive, especially in the case of fabricating high-aspect-ratio-structures where complex masks are required (Bu et al., 2004). Mechanical drilling is not the optimal choice for glass machining due to glass brittleness where long drilling time result (Egashira and Masuzawa, 1999; Baek et al., 2013) and rough machined surfaces are formed (Baek et al., 2013; Park et al., 2002; Zhang et al., 2005). Ultrasonic machining causes deteriorated surface quality (surface cracks) and a poor surface finish (Thoe et al., 1998) while other mechanical machining techniques like sawing can just produce simple structures (Plaza et al., 2003). A promising solution to this challenge is using non-traditional machining processes such as for example ultrasonic-drilling combined with chemical etching (Choi et al., 2007).

SACE or Spark Assisted Chemical Engraving is one among several technologies for micro-machining non-conducting materials, mainly glass, based on electrochemical discharges. It was first introduced in 1968 by Kurafuji and Suda, for drilling micro-holes in glass, where they called it electrical discharge drilling (Kurafuji, 1968). In the beginning, SACE was often compared with electrochemical machining (ECM) and electrical discharge machining (EDM), until (Cook et al., 1973) showed that SACE is significantly different from ECM and EDM. The authors suggested calling the process *discharge machining of nonconductors*. The machining process takes place in an electrochemical cell that is composed of two electrodes dipped in an electrolyte (NaOH or KOH). When a voltage greater than the water decomposition potential is applied between the two electrodes, water is split into hydrogen and oxygen. Bubbles start to form around the tool-electrode, which is the thinner one. As the voltage increases, the current increases in a proportional manner. When the voltage reaches a critical value, bubbles coalesce to form a gas film and electrical discharges are generated (Wüthrich and Fascio, 2005). SACE technology has already been applied by some research groups in the micro technology (Esashi et al., 1990) and nanotechnology fields (Lal et al., 2008) to fabricate micro-sensors and nanoparticles on the lab-scale.

1.1 Motivation and Challenges

The state-of-the-art SACE drilling proved its ability to drill deep holes. Recent attempts by (Jui et al., 2013) resulted in 1:11 aspect ratio holes but drilling was performed at a low tool feed-rate ($1\,\mu$m/s) while applying a high machining voltage both of which result in a deteriorated machining quality. Two SACE drilling configurations have been used and

discussed in the literature so far: gravity-feed and constant-velocity-feed drilling. In the first one, a constant force is applied to the tool where machining proceeds while the tool contacts the glass surface. In the second, the tool is moved towards the glass surface at a constant feed-rate (see Chapter 2).

For both strategies it is challenging to use tools smaller than 400μm in diameter due to the frequent tool-glass surface contact resulting in tool bending, and sometimes even tool breakage. For tools of about 400 μm diameter, drilling rate can reach 100 μm/s for depths up to 100 μm, while it is significantly reduced for holes deeper than 200 μm (Wüthrich, 2009). Latest SACE research succeeded in identifying zones where drilling can proceed with little forces and minimal heat affected zones. Maillard et al. (2007) showed that depending on the machining parameters (voltage, tool rotational speed, tool feed-rate) holes with deformed entrance, jagged contours and deteriorated surface quality can result. Nevertheless, these studies remain limited as they explored the issue of reduced machining rate and deteriorated machined surfaces only for certain machining conditions. Other approaches were done to improve the machining performance including superposing tool movements while feeding the tool towards the glass like adding tool-rotation (Gautam and Jain, 1998), using pulsed voltage supply (Kim et al., 2006), using various tool-electrode geometries (Lee et al., 2004; Zheng et al., 2007) and circulating the electrolyte by adding ultrasonic vibrations (Han et al., 2009) and magnetic fields C-P Cheng (2010). Despite that some of these methods improved drilling performance, the reasons behind limited machining are not explored and remain fuzzy. As of today, one has to admit that the knowledge about SACE is still limited and scanty. For example, it is not yet possible to know the allowable values of machining parameters that result in a good surface quality, within an acceptable range of variation, for different tool sizes, hole depths and machining voltages. As a direct consequence of this lack of knowledge, SACE machining is still a blind process and not yet suitable to be used for industrial production of micro-devices.

To take control over the SACE machining process, the reasons behind surface non uniformities and cracks have to be first identified. Hence, a deep understanding of the machining mechanism and the phenomena occurring locally in the machining zone is necessary. So far, it is believed that SACE machining is a combination of thermal and chemical effects (Jalali et al., 2009). However, the machining mechanism has never been clearly understood. It is commonly agreed that during SACE machining the glass is attacked chemically by the OH radicals, supplied from the alkaline solution, which break the Si-O-Si bond. The high energy discharges emitted through the gas film cause the tool temperature to reach 500 °C, quantified by using thermocouples (Kellogg, 1950), by doing spectroscopic measurements (Reghuram, 1994), and based on estimating the glass viscosity in the machining zone

(Wüthrich, 2009; Jalali et al., 2009). However, no measurement or estimation of the local glass temperature, which could give valuable information about the machined surface properties, has been carried out.

Not only is the temperature of the machined surface layer unknown, but also its nature. One study showed that after machining the surface is softened (Didar et al., 2009). However, no attempt was done to investigate the surface layer's nature. Several relevant questions come to mind: Is the surface layer a recast layer, like in the case of electrical discharge machining of metals? Does it have different properties than those of the bulk? What is the surface layer composed of and how thick is it? Can it be textured and how? Is the tool in contact with surface layer during machining or there exists a gap between the two? In case this gap exists, what is its typical value?

Answering these questions is challenging. The straight forward idea of using camera vision to observe the local phenomena happening in the machining zone is not possible due to the turbulence created by the irregular formation and breakdown of the gas film. The successful approach to use the current signal for measuring the tool-work piece gap during machining of conductive work-pieces, failed to give any outcome for SACE (Wüthrich et al., 2006b). Hence, a proper monitoring signal is needed to extract information about local parameters in the machining zone while machining. This idea has never been proposed in the field of SACE prior to this work. Hence, a methodology to measure the corresponding entities during the machining process is required.

1.2 Contributions

In this work, it is proposed to use the force exerted on the tool-electrode during machining in order to extract information about the machining zone and the machining status. The collected data is further supported by thermal analysis in order to extract information about the local temperature. This methodology results in the following contributions to the research field of SACE:

1.2.1 Methodology to measure and characterize forces during SACE machining

The drilling forces are measured for various machining conditions. A methodology to characterize these forces is developed where it is shown that the machining limiting factors are the surface heating at low depths (lower than 100 μm) and hole flushing at high depths (higher than 200 μm). The appearance of forces (force regions) for holes drilled when applying dif-

ferent machining conditions are identified in function of the hole depth. Based on these results, a dimensionless curve of normalized tool feed-rate versus hole depth is constructed, where normalization is done by considering the effect of local heating and flushing. This plot allows choosing the applied machining conditions such that for a desired drilling depth minimal machining forces result. This approach proves to be very successful to obtain a deeper knowledge about the process and to improve the drilling efficiency. It was further shown that the tool can bond to the glass surface during machining where this effect could only be known using the force signal.

1.2.2 The tool-surface gap

Based on the force signal, a methodology to measure the tool-surface gap is developed. The gap is measured for different machining conditions where the heat is identified to be a key for its formation. A thermal model that quantifies the gap in relation to the heat transfer from the tool to the glass surface is therefore constructed. The model is based on the hypothesis that the maximal machining gap is reached when the temperature between the tool and the surface drops below the electrolyte salt melting point. The match obtained between the calculated gap and the measured one, ensures the validity of both the model and the gap measurement method.

1.2.3 Novel exploration of the local machined surface properties and the machining mechanism

The machining temperature and mechanism

The machining temperature, which was an open question in the field, was found to be dependant on the machining configuration and geometry. In fact, machining can occur in two modes depending on how well flushing progresses:

- For enhanced flushing, especially on the glass surface (for depths lower than 100 μm), the electrolyte is still aqueous and etching can occur. In this case the glass machining temperature is around the electrolyte vaporisation temperature (between 100 and 200 °Cfor KOH and NaOH depending on the aqueous solution concentration).

- For high depths, the tool is in frequent contact with the glass surface where the electrolyte may be in a molten or aqueous state depending on how well flushing is. For limited flushing, the machining temperatures is higher than the electrolyte salt melting

temperature (around 318 °C for NaOH and 406 °C for KOH) and can reach the tool temperature. In this case etching progresses more efficiently.

For high depths however, as the flushing is limited, machined material and bubbles can accumulate beneath the tool reducing heat transfer to the glass surface. For a temperature higher than the electrolyte vaporisation temperature and lower than that of the electrolyte salt melting temperature, no machining occurs as the electrolyte is solidified.

Based on these results, the machining mechanism is clarified to be mainly due to high temperature etching by OH radicals that break the Si-O-Si bonds and physical bombardment of the surface with high energy discharge channels that result in formation of surface craters. Results show that glass may be gradually re-formed on the surface during the drilling process as the product of etching is a glass forming melt.

Origin of the surface texture

The local flow of the electrolyte in the machining gap proved to be the reason for the observed surface patterns. The local flow is caused by: the gas film continuous breakdown and reformation and by the tool motion (rotation). For reduced machining gap the local electrolyte flow patterns are imprinted onto the machined surface, and they are less pronounced for higher machining gap. Since the flow is affected by the electrolyte properties, changing the electrolyte viscosity proves to influence the resulting texture that can range from smooth (high viscosity) to feathery-like (low viscosity). Kelvin-wake patterns were observed for 2D machining while using electrolyte with low viscosity similar to that of water (Reed and Milgram, 2002).

1.2.4 Development of force feed-back strategies for SACE drilling

Based on the understanding that this work brought about the machining mechanism and the factors that influence it, the potential of using force feedback algorithms to enhance the drilling performance is investigated. Different force algorithms are built based on the goal of balancing both local heating and flushing. The algorithms succeeded in drilling high-aspect-ratio holes up to 1:9 while using very small tools (70 μm diameter) without breakage. The resulting drilling time is dramatically reduced to few seconds compared to several minutes in the state-of-the-art SACE drilling. The developed knowledge and the preliminary force-feedback algorithms are transferred to the company Posalux SA. This company is the first one in the world that manufactured a SACE machine, that was put this year on the market.

1.3 Outline of Thesis

The present research work is divided into two parts. The first part presents the methodology used to quantify the measurement errors and the machining gap. The corresponding measurements where matched with theoretical models. The significance of this work is demonstrated in the second part by presenting the potential of preliminary built force feedback algorithms on enhancing the SACE machining performance.

A review of the knowledge about SACE drilling, mainly the drilling configurations and the machining mechanism, from today and travelling back in time to the moment where the first micro-hole was machined by Kurafuji and Suda in 1968 is summarized in Chapter 2.

Chapter 3 presents a novel methodology that allows identifying measurement errors (tool expansion, bending, wear) and measuring the machining zone entities including the machining gap based on the machining forces. The force signal is used to quantify measurement errors caused by the tool wear, bending and thermal expansion. Further, models are developed for estimating the mentioned entities. This has never been explored prior to this work. Without this data, information about the machining zone's properties would not have been possible to extract.

In Chapter 4, the force exerted on the tool is measured and characterized for various machining conditions. A dimensionless curve of the tool feed-rate versus the hole depth is constructed. This curve allows choosing the appropriate machining conditions based on the desired hole depth such that drilling can be done with minimal machining forces. This work is a significant contribution to the field of SACE knowing that the data available so far is specific to the machining conditions used. Further, this chapter shows that a tool-glass bond forms while machining where this bond is identified to be chemical.

Chapters 5 and 6 unveil information about the main unknowns in the machining zone in addition to the machining mechanism. Chapter 5 investigates the maximal machining gap formed between the tool and the hole bottom surface for different machining conditions. A thermal model that estimates the gap is also presented. The machining mechanism in addition to the nature of the machined surface layer and its properties, basically its texture, are presented in Chapter 6. The machining temperature is identified to vary depending on the machining geometry and configuration. For shallow structures, the electrolyte is in aqueous form where its temperature reaches the electrolyte vaporisation temperature. For deep holes where flushing is limited, tool-surface contact exists where the electrolyte is in a molten state and the machining temperature reaches that of the tool. Therefore, machining occurs when the electrolyte exists in aqueous or molten state which is determined by the local flushing. As for the texture, its formation is proved to be caused by the local electrolyte flow

inside the machining gap where the electrolyte flow is influenced by both the tool motion and the gas film dynamics. Based on these results, it is concluded that machining is caused by thermal assisted etching, where the high energy discharges generated locally heat the glass surface, and by physical bombardment of the surface by discharge channels (evidenced by crater formation on the surface).

The acquired knowledge about the machining mechanism and the machining zone's parameters is applied to develop feedback algorithms in Chapter 7 based on the force signal. The purpose is to test the potential of preliminary algorithms that balance both the local heating and flushing, on improving the machining performance. The efficiency of the algorithms is measured in terms of the ability to produce high-aspect-ratio holes during a short time while using tiny tools (seven times smaller than the state-of-the-art used ones) without causing tool or work-piece damage.

Chapter 8 summarizes the contributions of this work in advancing the knowledge about the SACE machining process and it presents preliminary ideas on how to address some remaining open questions.

Chapter 2

SACE micro-machining: state-of-the-art knowledge

The true definition of science is:
the study of the beauty of the world...
(-Simone Weil)

This chapter provides a review about the current understanding of the SACE machining mechanism in addition to the recent developments achieved in micro-hole drilling. What are the capabilities of the SACE drilling process? What is it required to achieve? Is the process controllable? Can it be monitored and how? What is the current knowledge about the local machining zone properties, including the surface layer? These are all questions that the present chapter will address in the context of work recently done on SACE micro-drilling.

2.1 SACE Machining process

Spark assisted chemical engraving is a process for machining non-conducting materials, mainly glass and ceramics, based on the electrochemical discharge phenomenon. Machining takes place in an electrochemical cell where two metallic electrodes (anode and cathode) and the work-piece to be machined are dipped in an electrolytic solution (Figure 2.1). The tool-electrode, normally being the cathode (-), is positioned above the work-piece and has a surface area much smaller than that of the counter-electrode. As a voltage is applied between the two electrodes, bubbles start to form where they coalesce into a gas film around the tool-electrode for a high enough voltage. Figure 2.2 depicts the current-voltage characteristic curve and the different stages of the gas film formation. For a voltage higher than the water decomposition potential U_d, bubbles start to form (point A) around the tool. For

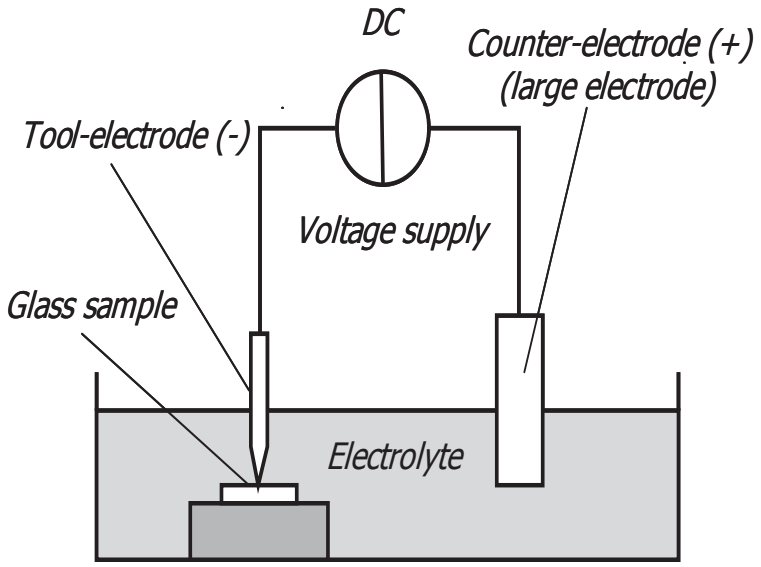

Figure 2.1: The SACE electrochemical cell schematic. Reprinted from (Didar et al., 2009) with permission from Elsevier.

increased voltage, the current increases linearly (region AB) where bubbles grow in size and become more dense (region BC). The curve reaches saturation where the maximal point C corresponds to the critical voltage U^{crit} and critical current I^{crit} above which a gas film can be formed. In fact, the drop in the current signal in region CD indicates that the bubbles are coalescing into a gas film. Starting from point D, the gas film is formed and high energy discharges (few eV) are generated.

Two configurations have been used so far for SACE micro-hole drilling: gravity-feed and constant-velocity-feed (Wüthrich, 2009):

Gravity-feed drilling

The gravity-feed drilling strategy is the most popular one for micro-hole drilling. During gravity-feed, the tool-electrode is always in contact with the glass surface and drilling proceeds only under the action of a constant force. However, the force acting on the tool-electrode must not be too high in order to avoid bending or breaking the tool-electrode or the work-piece. For this machining mode, for low depths (up to 100 μm/s) the electrolyte can enter into the hole (unlimited flushing) where machining rate can reach 70 μm/s (discharge regime). At high machining depths (typically higher than 200 μm) it becomes difficult for the electrolyte to enter the micro-hole and remove the machined material. Hence, drilling enters the hydrodynamic regime and at high voltages heat affected zones may form. This causes poor machined surface quality (Wüthrich et al., 2006c).

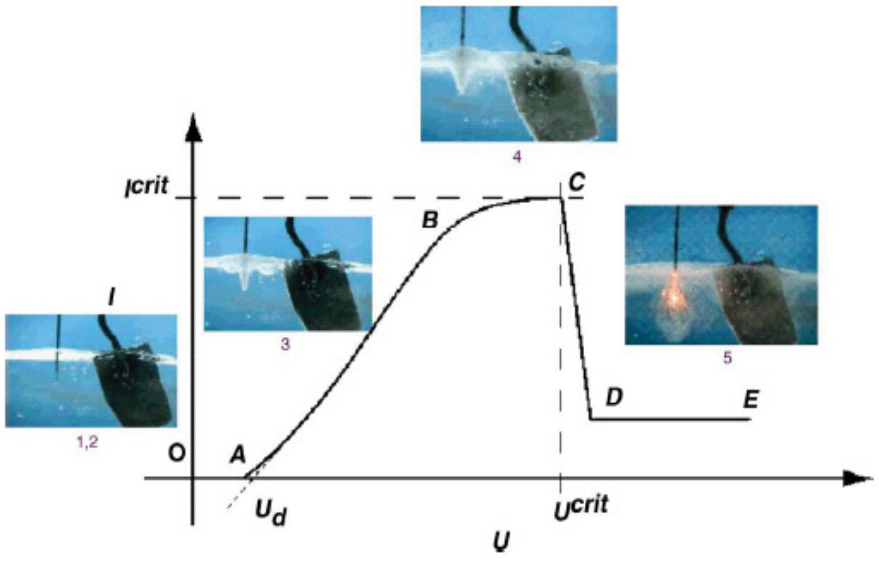

Figure 2.2: The SACE current-voltage characteristic curve. Reprinted from (Didar et al., 2009) with permission from Elsevier.

Constant-velocity-feed drilling

During constant-velocity-feed drilling, the tool is moved at a constant speed towards the glass surface starting from a certain position above it. In this case, the tool feed-rate has to be less than the material removal rate of the process to avoid breaking the tool-electrode or the glass work-piece. In fact, it was found experimentally that a tool feed-rate up to 20 μm/s (Lim et al., 2001; Shiuan and Yang, 2006; Han et al., 2007) can be used depending on several factors including the machining voltage and the electrolyte concentration. The problem with this strategy is that during machining the tool may be at a distance from the glass surface or may contact it. As the distance between the tool and the work-piece could not be measured so far during drilling, machining cannot be monitored with this strategy.

In both strategies, drilling rate is dramatically reduced for high depths starting from 200 μm and high-aspect-ratio-holes with good surface quality are difficult to achieve during a short drilling time.

2.2 SACE machining mechanism

As of today, there are still controversial opinions about the SACE material removal mechanism, even wrong concepts exist. This is due to the complexity of this process which can be seen from the various names given for it including *Electrochemical spark machining ECSM* (Panda and Yadava, 2009), *Electrochemical discharge machining ECDM* (Ghosh, 1997), *Elec-*

trochemical Arc Machining ECAM (Kubota, 1974) and *Spark Assisted Chemical Engraving SACE* (Wüthrich, 2009). Sometimes SACE is even confused with metal machining processes which are based on different principles. For some, SACE process is a combination of Electrochemical Machining (ECM) and Electrical Discharge Machining (EDM) (Jain and Adhikary, 2008; Panda and Yadava, 2009; Han et al., 2011; Panda and Yadava, 2012). While ECM occurs by dissolution of the work-piece, EDM is due to current flow from the tool to the work-piece resulting in work-piece erosion.

Currently, there exist several suggestions of the machining mechanism, the common ones being melting and etching, in addition to other non-popular theories like weathering and shock waves caused by fluid motion (Jain et al., 1991). The vast research conducted in this field agrees that during SACE the electrochemical discharges attack the glass in some way. Tokura et al. (1989) showed the significance of etching on the machining process through experimental investigations on ceramics. The idea was comparing through experimentation the mass of removed material when placing the work piece in electrolyte of different temperature. Results showed that when keeping the ceramic in 20 wt% NaOH solution for 30 h at 30 °C no change in mass could be measured whereas when increasing the electrolyte temperature to 150 °C during 30 min the mass decreases, the loss being similar as when applying a high voltage discharge. Fascio et al. (1999) hypothesized that the machining is thermal due to discharges and chemical due to attack by OH radicals. The authors showed, upon analysing the composition of glass machined surfaces, that H^+ replace Na^+ ions. Accordingly, it was hypothesized that etching causes dissolution of silicate. Controlling etching rate is shown to be difficult due to temperature fluctuations in the tool vicinity where only 10 °C increase in temperature can double the etching rate (McLellan and Shand, 1984). Yang et al. (2001) considered that the etching reaction is the basis in ECDM. Upon analysing surfaces machined using different voltages and electrolyte temperatures (analysis done by SEM and EDX), it was found that different material removal rate results. Jain and Adhikary (2008) did chemical analysis of the sodium hydroxide solution in which they machined quartz. They found traces of copper and silica ions indicating that quartz is dissolved in NaOH. Therefore, the authors concluded that quartz machining is due to chemical dissolution in addition to melting of the work-piece.

Although the machining mechanism is explored partially, other local phenomenon are not yet investigated. These include the local surface texture and its origin of formation.

Modelling the SACE process

As the SACE machining mechanism is still not very clear till today, it is modelled in various ways. Many attempts have been made to build models for simulating the SACE machining

process based on the heat supplied to the glass surface from the discharges. However, each model gave different predictions since basic understanding about the process is still missing and many assumptions had to be taken into account. For example, different models assume different glass machining temperature T_M. An overview of these models is presented in the following text.

Basak and Ghosh (1996) developed a model for the discharge generation that estimates the needed critical voltage and current to generate a discharge. The idealised electrochemical discharges mechanism was considered an accurate representation of the actual physical phenomenon occurring. In a further step, the authors considered the discharge generation as a process similar to the switching off phenomenon in electrical circuit where they developed a model that predicts the energy generated by a spark (considered to be a cylindrical heat source) and its frequency. Accordingly, they estimated the total amount of energy available for material removal and hence the material removal rate (Basak and Ghosh, 1997). Jain et al. (1999) attributed machining to glass melting, assuming that material removal rate occurs for temperatures higher than 1100 K. They computed material removal rate by developing a finite element model that predicts the thermal energy generated by sparks based on a heat transfer model. The model also calculates the isotherms assuming that the position where the spark is generated, at the location of the heat source, is random. Results showed that the computed material removal rate is higher than the actual one measured from experiments.

Fascio et al. (2004) developed a heat model to predict the machining depth. The model assumes that the glass is machined for a temperature higher than its softening temperature (around 1193 K). Bhondwe et al. (2006) considered that the machining process is due to melting and vaporisation of the glass caused by heat transfer from the discharges. The authors established a finite element method based on axisymmetric thermal model that uses heat transfer equations of conduction and convection to predict the temperature distribution among the nodes on the mesh. The heat source is assumed to follow a Gaussian distribution based on results from (Kulkarni et al., 2002) which showed that the machined surface has a dome shape. As machining is considered to occur at the glass melting temperature, the volume of removed material is calculated based on the isotherm corresponding to this temperature. The model predicts that the surface temperature starts from 14000 K in the middle of the spark and decreases to room temperature after 225 μm distance from the center. Panda and Yadava (2009) built a 3D finite element transient model that predicts the temperature distribution during travelling wire machining based on the assumption that the machining process is solely thermal and that no deposition of recast layer occurs on the surface. Like Bhondwe, the authors assumed that the heat source follows a Gaussian

distribution. The model predicts that material having a temperature higher than the glass melting temperature, around 1423 K, is removed. As the model assumes that a single spark is generated at a time, the material removal rate due to applying a certain number of pulses is calculated by summing up the volume of material removed for each spark divided by the duration of the sparks. The volume of material removed per spark is calculated based on the generated isotherms corresponding to the glass melting temperature. Results showed that material removal rates predicted by the model are higher than the actual ones. It was further found that the material removal rate increases with the energy transmitted to the surface and the duty cycle.

The presented models for predicting material removal rate are all based on the assumption that machining is solely thermal. However, no attempt was made to calculate the temperature needed to machine glass. In fact, this temperature was assumed when developing models to predict the material removal rate as 1193 K by (Fascio et al., 2004), 14000 K by (Bhondwe et al., 2006), 1423 K by (Panda and Yadava, 2009), and above 1093 K by (Jain et al., 1999). Despite the fact that the temperature required to machine glass is assumed differently in each of the models, these models predicted similar machining rate. This is due to the complexity of the models where they contain many parameters that allow tuning them in order to match with experimental findings.

Jalali et al. (2009) considered that machining occurs due to thermal melting in addition to etching where the OH radicals, supplied by the electrolyte, etch glass according to the following reaction:

$$2NaOH + SiO_2 \longrightarrow Na_2SiO_3 + H_2O \tag{2.1}$$

Based on this reaction, the OH radicals break the Si-O-Si bonds of the glass. This results in forming sodium silicate, which is a glass forming melt.

The etching rate p, which is the mass of material removed (in milligrams) during 1 hour per unit area, can be calculated from Equation 2.2 (Fascio, 2002) in function of the applied temperature T up to a maximum of 100 °C:

$$p = 3 \cdot 10^7 \exp(\frac{-6571.3}{T}) \tag{2.2}$$

For 100 °C the etching rate is around 4 μm/s. As the temperature is much higher than this during SACE (tool temperature reaches 600 °C), this rate must be dramatically increased. Therefore, the authors postulated that in the discharge regime, machining is not limited by the etching rate but rather by the heat propagation inside the glass. Based on this idea, machining rate in gravity-feed drilling is predicted by assuming that the local temperature is the same as that of the tool (around 600 °C). The authors further predicted the existence

of a layer of softened material that exhibits a drag force on the tool during machining when both are in contact. The authors estimated the machining rate during the hydrodynamic regime (occurs at depths higher than 200 μm) based on the assumption that viscous material accumulates locally for high depths which result in a drag force on the tool. The limiting machining was related to the drag force (based on stoke's equation) as:

$$v_{lim} = \frac{F}{6\pi\eta b} \tag{2.3}$$

where F is the drag force, η is the work-piece viscosity and b is the radius of the cylindrical heat source. Based on Equation 2.3 the viscosity could be approximated for a known force and limiting speed (based on experimental data). The authors reported that the resulting viscosity corresponds to a temperature around 600 °C which is less than the glass softening temperature. At this temperature glass is rigid (viscosity around 10^8 compared to $10^3\, Pa \cdot s$ at its melting temperature) and therefore machining cannot be only thermal. As a result, the authors attributed SACE machining to be a result of etching and thermal machining. In fact, the depth at which the hydrodynamic regime starts as predicted by (Jalali et al., 2009) (300 μm) is the depth limit up to which the finite element based model built by (Wei et al., 2011), which simulates the machining due to a single spark, is valid. Jiang et al. (2014) measured experimentally the spark energy and fit it to a stochastic model. The spark energy and the volume of the machined material were related using a finite element model that considers machining to be caused by thermal melting and etching. In this case, the glass is heated due to the heat transferred from the discharges.

Wüthrich (2009) estimated the material removal rate in the discharge regime during gravity-feed drilling knowing that the ability to heat the surface is the key in machining evolution. The discharges generated from the tool act as a heat source. For his purpose they developed a heat transfer model where the key assumption is that drilling takes place as soon as the machining temperature T_M is reached which is considered to be that of the tool in gravity-feed drilling. Based on the solution of the heat equation, the evolution of machining temperature T_M isotherm allows predicting the material removal rate (evolution of hole depth z in function of time). Therefore, material removal rate is written in terms of the normalized heat power κ (ratio between applied heat power and the minimal one needed to machine glass), the tool radius r and glass thermal diffusivity α as follows:

$$\frac{dz}{dt} = \frac{4a}{r}\frac{\kappa - 1}{2\kappa}\left[1 - \exp\left(\frac{\pi(\kappa-1)^2}{\kappa^2}\right)\right] \tag{2.4}$$

Equation (2.4) assumes that the heat power needed to machine glass is less than 1 W.

The experimental results of the machining rate in function of the applied voltage (expressed in terms of κ) match with the values predicted by Equation (2.4).

The present review shows that the current models in the field of SACE predict that the material removal rate increases with higher discharge energy implying higher local temperature. The models however are not a good representation of the machining mechanism as they are too complex while the basic understanding of the process is still missing. In fact, each of these models assumes very different temperatures at which glass is machined and no attempts to measure this temperature were done so far. Since the SACE machining process proves to be temperature dependent, it would be beneficial to first model it with simple heat transfer models to predict the local temperature distribution on the glass surface and the glass machining temperature.

2.3 SACE drilling capabilities

As mentioned in Section 2.1 both gravity-feed and constant-velocity-feed drilling face the problem of reduced machining rate for high depths especially for tools larger than 300 μm. In case of gravity-feed drilling the drilling rate reaches 100 μm/s for the first 100 μm (Wüthrich et al., 2006c) and decreases to less than 4 μm/s for depths higher than 200 μm which is explained to be a result of accumulation of machined material locally (Jalali et al., 2009). A stair-like evolution of machined depth in function of drilling time was realized in this case. For constant-velocity-feed drilling, the highest tool feed-rate that could be used for 400 μm diameter tool was up to 20 μm/s depending on machining conditions (voltage and the electrolyte concentration) (Lim et al., 2001; Shiuan and Yang, 2006; Han et al., 2007). This section provides a review about the capabilities of SACE drilling in terms of quality and drilling time. The variability in both factors is presented as well.

2.3.1 Predictability of the machining process

Studies have shown that the SACE machining process is variable where widely dispersed patterns are normally formed (10 to 20%). This was attributed to the instability of the gas film (Wüthrich and Hof, 2006). Hence, methods to enhance the gas film stability, based on reducing its thickness, were proposed with the purpose of reducing the process variability. These included influencing the density of the bubble nucleation sites, adding tool rotation (hydrodynamic fluxes) or influencing capillarity forces at the tool-gas-electrolyte interface. The last was investigated by reducing the tool wettability by adding surfactants to the electrolyte (Wüthrich et al., 2005c). Although drilling time increases in this case, results

showed that the reproducibility increases (dispersion of diameter is reduced from 20 to 5 μm) and the surface quality is enhanced where smoother surfaces result (reduced critical voltage). Wüthrich et al. (2006b) showed that during gravity-feed drilling, the hole depth evolution in function of time differs even when applying the same machining conditions. The authors further showed that the gas film improper formation limits the machining speed and that the initial electrolyte temperature greatly influences the variability of the process. In case of metal machining, (Kulkarni et al., 2003) showed a correlation between the fluctuation of the local temperature and that of the current flowing between the two electrodes. The role of local temperature on machining progress was shown as well by (Wüthrich et al., 2006c) where drilling was faster as more holes were machined (during gravity-feed drilling). The drilling evolution in function of time reaches a steady-state where it became more repeatable after machining 10 holes.

Morrison (2009) developed an approach to predict SACE variability in gravity-feed drilling based on stochastic models. This approach was based on using the steady state value of the coefficient of variation (predicted by the models), denoted in this text as SSV, to compare variability between data sets. Results showed that both preheating the electrolytic solution to its steady state temperature prior to machining or controlling the electrolyte level above the work-piece with an error of ± 0.05 reduces SSV by a factor of two. The combination of both elements results in reducing SSV by 30% of the standard value. Morrison also demonstrated that maximum reduction in variability (by a factor of 3) is established by applying a simple algorithm during drilling (changing the machining voltage depending on the hole depth evolution) (Morrison et al., 2008).

Moussa (2008) identified a strategy for reducing machining variability based on statistical tools. He found that preheating the tool and the work-piece (to 80 °C), applying pulsed voltage and reducing the electrolyte level above the work-piece, reduce the variability. Moussa further suggested using a tool of low thermal conductivity for high hole depth (hydrodynamic regime) so that the machining zone could remain hot (less heat dissipation through the tool).

Based on this information, it can be concluded that by monitoring the local temperature in the machining one, the variability in machining would be dramatically reduced.

2.3.2 Towards improving machining performance

The previous section shows that the local temperature fluctuation contributes greatly to the variability in the machining process. In this section the various conducted investigations on improving the machining quality and reducing the drilling time are presented.

Enhanced machining quality

Maillard et al. (2007) studied the effect of local temperature on the hole geometry. The authors particularly investigated the effect of both the hole depth and the machining voltage on the mean entrance diameter size of the hole during gravity-feed drilling. Three regions could be distinguished in the hole depth versus voltage plane. For low depths (less than 100 μm), where the machining speed is dependent on the applied voltage, defined circular diameters and smooth surfaces result. For high depths (more than 200 μm) machining speed is independent of the voltage (hydrodynamic regime) as it is limited by the ability to flush the hole. Heat affected zones result around the hole entrance in this case and the mean diameter increases linearly with the hole depth. For high depths and low voltage (less than 31 V) jagged contours result while at very high voltages (above 36 V) cracks are formed on surface and the entrance is deformed. Therefore, for high temperature, indicated by high applied voltages, the hole quality is dramatically reduced. The effect of local temperature on the hole quality was also demonstrated in the work of (Kim et al., 2006). It was shown that when applying rectangular pulsed voltage supply the thermal damage is reduced for increased pulses frequency and duty ratio due to the local heat reduction.

The tool geometry is also proved to influence the resulting machined surface quality. Zheng et al. (2007) showed that the machining quality is enhanced when using a flat side wall-flat front tool (due to enhanced local flushing and reduced discharges influence on the tool sides) together with pulsed voltage supply. The taper angle and the thermal damage are reduced in this case and drilling time is enhanced. Further, it was shown that tool rotation enhances machining. However, this is valid only for small rotational speeds (less than 1500 rpm). This was explained by the increased machining time for high tool rotational speeds causing a larger hole entrance diameter. It was further demonstrated that when using the modified tool along with pulsed voltage and tool rotation, the formation of surface thermal cracks is avoided. Cheng et al. (2010) also showed that for a flat side-wall tool the machining efficiency is enhanced compared to a cylindrical tool. This was attributed to the lower surface area in case of a flat side-wall tool making discharges more concentrated in addition to the enhanced flushing as electrolyte can better circulate inside the hole. Therefore, a higher material removal rate and a reduced hole entrance diameter result in this case. It was also shown that for this tool the critical voltage is reduced which was explained as a consequence of a more stable (thinner) gas film. Han et al. (2009) used a side insulated tool and pulsed voltage for drilling holes where they showed that for these machining conditions higher drilling depths, compared to those reached in conventional SACE drilling, could be achieved and the holes had reduced over-cut and taper angle.

Several studies have shown that modifying the electrolytic solution can also influence

the machined surface quality. The effect of adding thermally and electrically conductive particles to the electrolyte was investigated by (Han et al., 2007). The authors showed that upon addition of graphite powder, up to a certain concentration (1 wt%), the machined surface roughness is reduced. This is explained by the decrease in current amplitude (reduced local temperature) caused by reduced gas film breakdown strength hence diminished spark energy. Han et al. (2007) also showed that the increase in tool feed-rate results in smoother surfaces. However, an excessive increase in the tool feed-rate or the powder concentration becomes counter-productive where roughness increases in this case. Results from the work of (Han et al., 2009) proved that vibrating the electrolyte has a similar effect as adding motion to the tool were higher machining depths result due to enhanced flushing. Adding surfactant (Sodium Dodecyl Sulfate) to the electrolyte while machining quartz proved to enhance machining (Peng and Liao, 2004) similar to the results obtained by (Wüthrich et al., 2005c) upon adding soap to the electrolyte. This results in reduced taper angle due to the enhanced machining rate. Jui et al. (2013) showed that drilling quality can be deteriorated for increased electrolytic solution concentration, where higher hole entrance and exit diameters (higher over-cut and taper angle) are formed.

Although with the above-mentioned methods improved hole geometry and higher depths could be achieved, the highest aspect-ratio (hole entrance diameter over depth) obtained is 1:2. Recently, (Jui et al., 2013) could drill high-aspect-ratio through holes of surface roughness ranging from 250 to 350 nm using a 30 μm tool having 500 μm of its length immersed in the electrolytic solution (1M NaOH). The holes, 180 μm in diameter and 1.2 mm deep, were machined using a tool feed-rate of 1 μm/s and a voltage of 30 V while adding tool rotation. Hence, the drilling time was around 1200 s. Results showed that the tool rotation enhances the hole circularity. The hole exit had a much smaller size compared to the entrance diameter where it was around 40 μm compared to 65 μm. Therefore, high-aspect-ratio holes (1:9) could be achieved in this study but during several minutes.

Enhanced drilling time

Results from gravity-feed drilling showed that when electrolyte is locally available and the material can be evacuated from the tool vicinity (local flushing), high machining rate results (Jalali et al., 2009). It is further shown that in the hydrodynamic regime, where flushing is limited, the drag force from the softened layer may be responsible for limited machining rate. In fact, (Wüthrich et al., 2006c; Didar et al., 2009) showed that the initial drilling speed is determined by time required for the heat from discharges to diffuse in the glass substrate where this depends on the voltage and the work-piece conductivity. The discharge activity can be limited by gas film instability which affects drilling rate (Wüthrich et al., 2006b).

The tool geometry proved to influence the machining evolution. Based on the results of (Yang et al., 2011), drilling time is reduced when using a spherical tool compared to a cylindrical one since hole diameter is smaller in this case. This is attributed to the enhanced flushing that this tool allows, where reduced tool-glass surface contact results. It was further shown by (Wüthrich et al., 2006c) that drilling with a pointed tool allows applying lower voltages while keeping same drilling rate established using cylindrical tools while applying higher voltages. In this case the drilling rate is enhanced due to the more concentrated discharge generation at the tool tip. This result is similar to that obtained by (Bhattacharyya et al., 1999) while machining alumina, where for a tapered tool or for increased voltage the drilling rate was enhanced.

Cook et al. (1973) proved that the drilling rate is increased for higher voltage and higher electrolyte temperature. The effect of voltage on the machining rate was also confirmed by (Kim et al., 2006; Fascio et al., 1999). The drilling speed is also influenced by the type of electrolytic solution used where (Yang et al., 2001) showed that replacing sodium hydroxide (NaOH) by potassium hydroxide (KOH) enhances drilling. Paul and Hiremath (2013) used Taguchi method of optimization to study the effect of machining parameters on material removal rate. The authors found that the machining rate increases for higher voltage, duty cycle, and electrolyte concentration. Further, (Jain et al., 2002) demonstrated that the addition of abrasives to the electrolyte promotes etching. The effect of adding different types of tool motion on enhancing the drilling rate was also researched. Adding tool vibration (Wüthrich et al., 2006a), tool orbital motion (Gautam and Jain, 1998) and tool rotation (Zheng et al., 2007) showed to enhance drilling rate.

Based on this section, it can be concluded that machining quality and drilling time can be influenced by modifying the tool properties (geometry, motion) or the electrolyte properties (conductivity, temperature) in addition to influencing the machining conditions (voltage, tool feed-rate) and the tool wettability. Choosing the best combination of these strategies in order to enhance quality while maintaining a reasonable drilling speed and vice-versa relies so far on trial and error where a trade-off has to be made. No data is available that can give in terms of desired drilling parameters (hole depth and tool geometry) the weight of each of these strategies on improving machining quality and drilling rate. This limits the ability of SACE drilling from achieving the machining requirements as demanded by several applications, for example non-deformed machined surface for holes drilled during a short time, or drilling high-aspect-ratio holes of good surface quality (no surface cracks or heat affected zones) during a short time (few seconds).

2.4 About monitoring SACE drilling

SACE drilling is conducted in gravity-feed or in constant-velocity-feed configurations. No signal is commonly used yet to monitor the drilling progress online (unless for few recent attempts) and hence, the majority of the work conducted about SACE drilling does not use feedback algorithms, which induces some variability into the drilling process (as shown in Section 2.3.1). As a result, SACE machining field is still limited to academia where some lab prototype devices were fabricated (Esashi et al., 1990; Lee et al., 2004). SACE is not yet implemented for industrial purposes although efforts are expended towards reaching this stage (Wüthrich et al., 2005b).

As shown in previous section, gravity-feed or constant-velocity-feed drilling are limited in terms of the drilling speed or quality that can be achieved. For example, (Wüthrich et al., 2006c; Jalali et al., 2009) showed that machining is fast up to 200 μm depth during gravity-feed and is limited afterwards (few μm/s). Further, it was shown that the maximum feed-rate that can be used during constant-velocity-feed without breaking the tool or the work-piece depends on the machining conditions where it can reach 20 μm/s (Wüthrich et al., 1999). The tool diameter and the hole depth proved to affect the drilling progress. While the tool diameter affects the local temperature by influencing the heat concentration at the tip, the hole depth affects the ability to circulate electrolyte inside the hole (Wüthrich et al., 1999). However, no detailed study was carried out that allows knowing the depth limit up to which reasonable machining rate can be maintained, for any chosen set of machining conditions.

The last section showed some approaches applied to improve the machining performance (accelerated drilling, enhanced quality) based on influencing the local temperature and flushing. These approaches included modifying the machining conditions or the tool or electrolyte properties based on trial and error to achieve desirable machining rate and quality. However, strategies that work for a certain hole depth may not be the optimal ones for higher depths.

To address this problem, some signals were proposed to monitor the drilling progress online. Wüthrich et al. (1999) suggested using a force sensor to monitor the machining force to prevent tool bending/breaking during constant-velocity-feed drilling. Spaelter et al. (2005) and Wüthrich et al. (2006b) proposed using the force signal as monitoring signal during drilling as well as the current signal, to qualitatively know if machining takes place, but no further investigation was carried out. In fact, (Kulkarni et al., 2003) showed that the current is related to the local temperature of the work-piece where the more discharges are generated the higher the local temperature would be. The current was also suggested by (Wüthrich and Hof, 2006; Wüthrich et al., 2005a) as a potential signal to monitor the gas film formation. Cheng et al. (2010) also showed that there is relation between the

gas film quality and the current signal and the machined contours. Two types of current signals could be distinguished: one generated through bubbles (low current spikes) and one generated through the tool part exposed to electrolyte (high current amplitude) where for the first case less hole contours are formed. Further, it was shown that a higher voltage causes a more stable gas film (denser and thinner), similar to results obtained in (Allagui and Wüthrich, 2009), contrary to low voltage which result in forming big bubbles that may detach by buoyancy. A possibility to enhance machining for TW-ECDM is using optical sensors to detect wire-work piece contact as suggested by (Peng and Liao, 2004).

Simple algorithms based on the force signal were done to improve the drilling performance. In fact, (Morrison, 2009) showed that the variability in drilling can be reduced by a factor of 3 when stopping machining during a certain time whenever a high force is exerted on the tool. Cao et al. (2009) could drill 60 μm diameter holes of depth around 150 μm during 700 s when using a 31 μm tool. The electrolyte level above the glass was controlled to be 100 to 150 μm. Drilling in this case was done while placing a load cell placed beneath the work-piece to measure machining forces. The force resulting from tool-glass contact is measured, where if it is higher than a certain threshold the tool is controlled to move away from the glass surface by 5 μm. The machining conditions applied (tool feed-rate, voltage pulse duty cycle, electrolyte type and concentration, and tool rotational speed) are the ones found experimentally to result in a good machining quality (minimal heat affected zones and reduced entrance diameter) and minimal structures size. This knowledge was applied to machining 3-D structures of various shapes, where a wall thickness as small as 10 μm and a good surface quality (0.1 μm roughness) could be achieved.

Mochimaru et al. (2012) showed that tiny hole exits (12 μm) can be produced by drilling the hole to a deep depth using a large tool and then proceeding to drill it through using very small tool (20 μm diameter) while applying tool vibrations and pulsed voltage. In order to achieve these results, a feedback circuit was established where the work-piece is fixed above an insulated tank containing electrolyte and a detecting electrode. As soon as the tool completely penetrates the glass work-piece, the tank insulation is broken and a current flows between the tool and the detecting electrode. When this current change is detected, by means of a photo-coupler circuit, the voltage is switched off.

These algorithms are preliminary and specific to certain machining requirements. Further investigation is needed to study deeply the reasons behind limited machining rate or quality and to build accordingly algorithms for enhancing machining performance for any desired hole size (diameter, depth).

2.5 Machined surface layer

Based on knowledge of the tool temperature, (Jalali et al., 2009) predicted that the glass is softened where at high depths, a viscous surface layer is formed. Until today, no studies have been conducted to identify the properties of this layer. However, (Didar et al., 2009) found through nano-indentation measurements, done on the surface of machined channels, that the surface hardness decreases after machining. Further, it was found that the calculated density of the glass based on the machined volume and the measured mass of machined material (slide weighed before and after machining) changes compared to the original glass density. This was attributed to fast surface cooling right after machining. These results show that SACE machining locally changes the glass surface properties.

Han et al. (2011) found correlation between the applied voltage and the surface roughness during electrochemical discharge machining. It was shown that for an increased voltage, the discharge current peak increases resulting in more rough machined surface. Maillard et al. (2007) found that during gravity-feed drilling, the resulting machined surface is smooth and the hole entrance is defined for depths lower than 100 μm (discharge regime). It was further shown that cracks and heat affected zones around the hole entrance are formed for deep holes and high voltages (hydrodynamic regime). It is demonstrated by (Yang et al., 2011) that the machined surface evolution in function of machining duration is different for cylindrical and spherical tools. For cylindrical tool etching evolves in the radial direction where a ring is first etched and it grows to a completely machined hole. For a spherical tool, similar effect occurs but etching also evolves in the Z-direction where deeper concave cavities are formed beneath the tool. For both tools a bump is reformed in the middle of the surface during machining.

Although these results demonstrate that the glass is modified during machining, no investigation of the machined surface layer properties, including its texture, was carried out.

2.6 Conclusion

The present review about the state-of-the-art SACE drilling shows that the machining mechanism is not yet fully understood. This is apparent from the enormous number of complex models that try to predict the machining rate where each model assumes a different glass temperature. It is also shown that while several attempts have succeeded to reduce the process variability, this is still restricted to specific machining conditions. Efforts have been devoted so far to improve the hole quality (wall flatness, surface roughness, hole circularity) but this is investigated by tuning machining parameters so that the needed machined

surface properties are achieved. This approach is based on trial-and-error with limited understanding of the reasons behind hindered machining performance. With the lack of this understanding, the process is not yet able to meet any required demand and cannot be considered as fully controllable. Few signals are proposed to monitor the drilling process, where feedback drilling has been applied recently but their potential to fabricate high-aspect-ratio holes was not reported. Although it was recently shown that high-aspect-ratio holes could be achieved during constant-velocity-feed drilling (during long time), no control algorithm that produces high-aspect-ratio holes within few seconds has been reported so far. As for the machined surface layer, the present review shows that no previous attempt has been done to investigate its properties including its temperature and texture.

Chapter 3

Experimental methods and materials

It all starts with a dream... the
hardest part is being willing to do what
-ever it takes to make your dream a reality.
(-Dave Thomas)

Material removal mechanism and generally speaking the machining process in SACE remains, as discussed in Chapter 2, an open question. This is mainly due to the lack of a suitable signal that could give information about local parameters in the machining zone including the local temperature, the tool-work piece gap and the surface layer properties. In this work, it is proposed to use the force exerted on the tool-electrode during SACE machining as a monitoring signal in order to fill this knowledge gap. The aim of this chapter is to present and validate the developed methodology for accurately measuring the machining forces.

The chapter starts by describing the machining set-up. The force sensor design and characteristics are presented. For enhancing the measurement accuracy the tool wear, bending and thermal expansion, have to be taken into account. These factors are quantified in Section 3.3. A lumped thermal model is also built which predicts the tool expansion in function of the machining zone temperature. The measured tool thermal expansion is matched with that predicted by the thermal model.

3.1 Machining set-up

In this section, the technical details of the SACE machining set-up are described. The properties and specifications of the mechanical and the electrical systems, including the data acquisition boards, are presented.

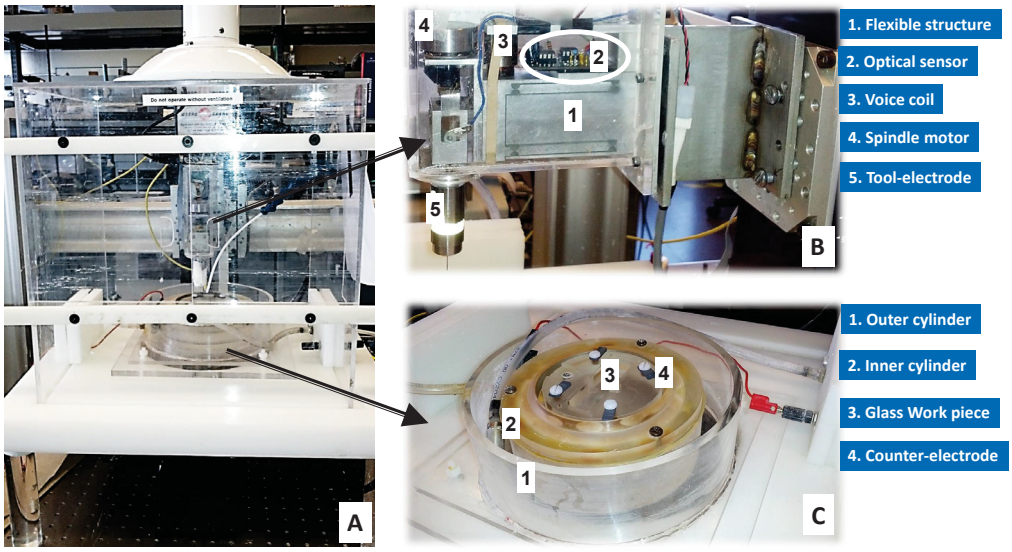

Figure 3.1: a) SACE table-top machining facility; b) The SACE machining head formed of a flexible structure, an optical sensor circuit, a voice coil actuator, a spindle motor and a tool-electrode; c) SACE processing cell. The counter-electrode and the work piece are fixed inside the inner cylinder that is filled with electrolyte. The electrolyte level above the work piece is controlled passively by an overflow system. The outer cylinder collects the electrolyte flowing from the inner cylinder.

3.1.1 Mechanical system

The set-up is composed of an XYZ platform (Cartesian robot) from Newport, a machining head assembly and a processing cell (Figure 3.1a). The SACE machining head assembly, holding the tool-electrode, is mounted on the Z-axis of the XYZ stage. The work piece is placed inside a processing cell mounted on the XY axes allowing its alignment with the tool-electrode. All the axes have a positioning precision slightly below 1 μm. Two types of electrolyte are used: sodium hydroxide and potassium hydroxide (prepared from deionized water). The work pieces are standard microscope glass slides purchased from VWR International and the tool-electrode is a stainless steel cylinder of diameter less than 500 μm.

Machining head

The machining head is mainly composed of a flexible structure, of very low damping, which has one degree of freedom z parallel to the Z-direction (Figure 3.1b). The structure, machined monolithically by wire electrical discharge machining (WEDM), holds the tool-electrode by a spindle-collet assembly. A motor is fixed to the spindle allowing its rotation at speeds ranging from 500 to 3000 rpm. The machining head also incorporates an optical sensor (SFH9201 from OSRAM Opto Semiconductors) and a voice coil actuator (LA-08-10-000 from BEI

Kimco Magnetics). It can be used in two configurations: as a profile-meter to measure the deflection in the z-direction, and as a force sensor to detect and compensate machining forces (using the voice coil actuator). In the force sensor configuration, the machining head can operate in two modes. In the first mode the force is measured based on the deflection of an elastic element. As will be described in detail in Section 3.2.2, the stiffness of the sensor is controlled actively via a PD controller. The last controls the input current to the voice coil (6 A maximum input, gain 1.1 N/A) generated by a servo drive (gain of 0.2 A/V). The measured force signal passes through a signal conditioning circuit (low pass 8th order Butterworth filter, 50 Hz cut-off frequency) which results in a 20 ms delay in reacting to these machining forces. In the second mode, the sensor is infinitely stiff and operates following the zero displacement force measurement principle.

Processing cell

The processing cell is composed of inner and outer cylinders (Figure 3.1c) of diameters around 100 and 190 mm respectively. The work piece is fixed to a base inside the inner cylinder by means of four cast acrylic holders. The anode, a stainless steel sheet, is fixed to the periphery of the inner cell's wall. It is connected to the power supply by a stainless steel wire passing through a hole on the side of the cell. The inner cylinder is initially filled with electrolyte. The electrolyte's level above the slide is maintained to be around 1 mm, depending on the electrolyte's viscosity, by means of an overflow system that uses a micro-pump (120SP1250-4EE purchased from Bio-Chem Fluidics). The pump injects fresh electrolyte to the cell (50 μL dispense volume and maximum flow rate of 6000 μL/min) without disturbing the local flow in the machining zone. The outer cylinder is used to collect the fluid flowing out of the inner cylinder. The excess fluid is evacuated from a drainage hole close to the outer cylinder's base via a peristaltic pump that is resistant to corrosive materials.

The SACE set-up is placed inside a chamber to isolate it from the surrounding. A ventilation system is connected to an opening on the top of the chamber to evacuate the generated electrolyte's vapour. Both the chamber and the processing cell are made out of cast acrylic which is a light weight, transparent, corrosion resistant and inexpensive material.

3.1.2 Electrical systems

The electrical system is composed of an optical sensor circuit, an XPS motion controller from Newport to control the motion of the XYZ stage, a dSPACE1104 real-time system for implementing the force sensor controller, a data interface box and a power supply (output reaches 125 W, 50 V).

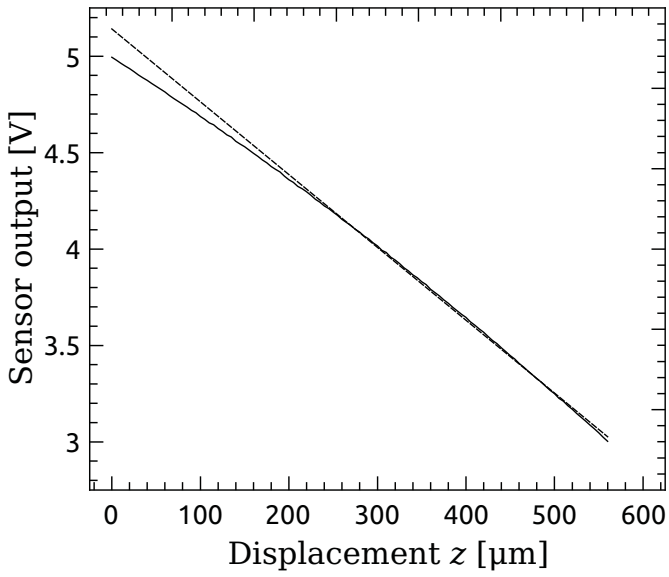

Figure 3.2: The optical sensor calibration curve. The sensor is used in the linear range, that is between 4.2 and 3 V output voltage corresponding to 270 μm z-motion. 5 V is the free position of the flexible structure.

Optical sensor circuit

The optical sensor circuit board, designed using KiCad, is fixed to the machining head base. When a force is exerted on the tool, the flexible structure moves with respect to its base causing a change in the sensor's output voltage. This voltage is amplified before being fed to an input channel of the data interface box.

The sensor is calibrated by recording its output voltage in function of the structure's z-motion as depicted in Figure 3.2. The sensor is used in the range where it shows a linear response, that is for an output voltage between 4.2 and 3 V (after amplification) corresponding to 270 μm z-motion. Note that 5 V corresponds to the position where the flexible structure initially stands (when released).

Data interface box

The data interface box allows data communication between the machining head, the XPS motion controller and the dSPACE real-time system. It contains a board for inputting/outputting analog signals to/from the GPIO2 board of the XPS system (four outputs and four inputs). This board communicates signals between the machining head, the dSPACE controller and the XPS controller. The main signals are the servo drive input voltage which controls the voice coil, the optical sensor's voltage and the power supply's input voltage. The box is also connected to twelve digital I/O channels of the GPIO4 board of the XPS and to sixteen

digital I/O channels of the dSPACE digital I/O board. The digital I/O channels are mainly used to trigger actions executed by the controllers, where the dSPACE can trigger actions done by the XPS controller and vice-versa. The box also contains a servo drive for controlling the voice coil current, a digital servo drive that controls the rotational speed of the motor connected to the spindle, and a micro-pump circuit board. The voice coil input current, the motor's rotational speed and the micro-pump flow rate are controlled by changing the voltage input to the servo drives and the micro-pump circuit via three XPS analog channels.

The motion of the X, Y and Z linear stages is controlled by programming TCL scripts that execute trajectory files uploaded to the Newport controller via a TCP/IP connection. The scripts also control analog signals among the two controllers and the machining head and execute actions by triggering digital I/Os.

The desired signals are recorded using channels on the XPS controller board or using ControlDesk which is the dSPACE computer interface. The dSPACE and XPS controllers can take input signals ranging from -10 V to +10 V (12 bits and 16 bits resolution) and they output signals in the same voltage range.

3.2 Measuring drilling forces

In this work, the force exerted on the tool during machining is proposed as a monitoring signal of the SACE process. The goal is to use it for extracting information about the machining zone's properties including the local temperature, the machining gap and the surface layer properties. For this purpose, the forces exerted on the tool-electrode while machining have to be measured precisely.

There exist several methods to measure the force applied to a body based on the following three common principles (Stefanescu, 2011, p. 17):

1. Measuring the acceleration of a body having a known mass.
2. Measuring the displacement resulting from applying the force to an elastic element.
3. Maintaining the body at a fixed position through compensating the applied force by a known force (zero displacement force measurement principle).

In the present work, it is chosen to design and build a force sensor that operates based on the second and third principles mentioned above.

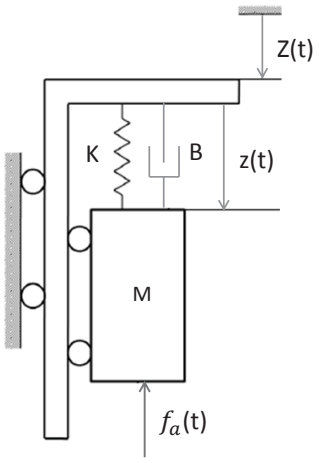

Figure 3.3: Mechanical model of the system: M is the machining head mass, K is the flexible structure's stiffness, B is the damping coefficient, $Z(t)$ is the motion of the Z-stage (moving at a constant speed $Z(t) = vt$), z is the motion of the tool-electrode fixation, and $f_a(t)$ is the force exerted on the machining head.

3.2.1 System model

The machining head is modelled as a second order system of mass M, stiffness K (flexible structure stiffness) and damping coefficient B (Figure 3.3). The machining head is mounted on the Z-stage that is moved at a constant speed v where $Z(t) = vt$, and Z is considered to be positive in the downward direction. For a downward motion Z of the Z-stage, the flexible structure will deflect when the tool contacts the work-piece surface. The displacement of the flexible structure z is measured by the optical sensor with respect to the flexible structure's stationary base. The equation of motion of the machining head can be written in terms of z (for the case where $Z(t) = vt$), v is constant) as:

$$M\ddot{z} = -Kz - B\dot{z} \tag{3.1}$$

When adding an external force $f_a(t)$ (opposite to the direction of motion), the equation of motion becomes:

$$M\ddot{z} = -Kz - B\dot{z} - f_a(t) \tag{3.2}$$

In order to properly design the force sensor such that the vibrations resulting from the Z-stage motion are filtered, the machining head eigenfrequency has to be determined. Hence, it is necessary to first identify the mechanical properties of the machining head including its stiffness. A schematic of the flexible structure is represented in Figure 3.4. The structure is composed of two horizontal beams (length a_1 each), a frontal vertical beam (length a_2), and

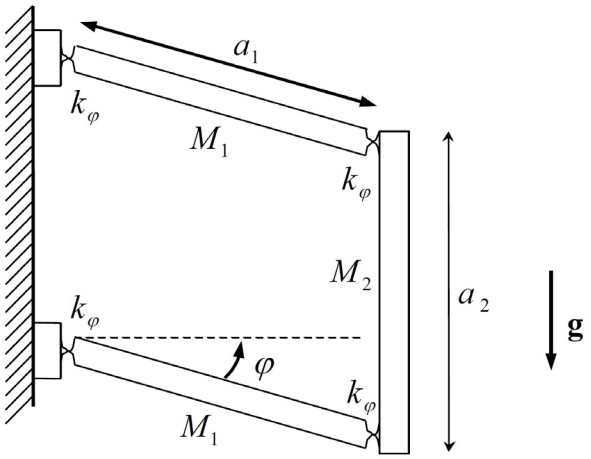

Figure 3.4: Schematic of the flexible structure. M_1 and M_2 are the masses of the structure's beams, a_1 and a_2 are the dimensions of the beams, k_φ is the hinge's angular stiffness and φ represents the angular motion.

four hinges each of angular stiffness k_φ. The angular stiffness k_φ of a hinge can be expressed in terms of the material's modulus of elasticity E, the width b, thickness e and the hinge radius r as follows (Henein, 2000):

$$k_\varphi = \frac{2Ebe^{2.5}}{9\pi\sqrt{r}} \tag{3.3}$$

The equation of motion of the flexible structure can be expressed in terms of the masses, M_1 and M_2, the moment of inertia I_A of one horizontal beam and the stiffness k_φ, the length of the horizontal plate a_1 and the gravitational acceleration g as (Figure 3.4):

$$\left(\frac{2I_A + M_2 a_1^2}{a_1}\right)\ddot{\varphi} + 4k_\varphi\varphi + (2M_1 + M_2)\, g a_1 = 0 \tag{3.4}$$

The eigenfrequency is extracted from Equation (3.4) as:

$$\omega_o = \sqrt{\frac{4k_\varphi}{2I_A + M_2 a_1^2}} \tag{3.5}$$

Accordingly, it is calculated to be about 8 Hz. Comparing Equations (3.2) and (3.4), the total stiffness K of the flexible structure can be determined based on its geometry by taking into account the angular stiffness of the four hinges k_φ and the length a of the horizontal beam as:

$$K = \frac{4k_{\varphi}}{a_1^2} \tag{3.6}$$

While the equivalent mass M of the second order system is expressed in terms of M_2, I_A and a as:

$$M = \frac{2I_A + M_2 a_1^2}{a_1^2} \tag{3.7}$$

The experimentally identified equivalent mass M (77 g) and stiffness K (3000 N/m), based on the system's step response, match with the calculated values where the mass is around 50 g and the stiffness[1] is around 2500 N/m. These results confirm that the system is correctly identified.

3.2.2 Force sensor design

In this section the force sensor design is presented. The design is based on the idea of measuring the displacement resulting from applying a force to an elastic element of well-defined stiffness. A PD controller is added to the system in order to tune the force sensor stiffness, where two conditions are considered. On one side, the sensor stiffness has to be minimized to obtain a maximal displacement for small forces. On the other side, the mechanical structure should be as stiff as possible to be robust against vibrations caused by the motion of the Z-stage holding the machining head. This trade-off between high and low sensor stiffness is taken into account when designing the PD controller such that the force sensor measures small forces while rejecting the machine's vibrations.

The proportional and the derivative terms, P and D, of the controller can be computed by requiring that the closed-loop system behaves as a second order system with a desired stiffness K_{cl} and damping B_{cl}. Upon adding the PD controller to the system, the motion is represented in terms of the desired closed loop stiffness K_{cl} and the damping B_{cl} as[2]:

$$M\ddot{z} = -K_{cl} z - B_{cl}\dot{z} \tag{3.8}$$

Combining Equation (3.2) and Equation (3.8), the force control signal exerted on the system is written as:

$$f_a(t) = (K_{cl} - K)\, z + (B_{cl} - B)\, \dot{z} \tag{3.9}$$

[1] Note that the value of K (Equations 3.3 and 3.6) is highly sensitive to the hinge width e which is difficult to control during manufacturing by EDM

[2] For simplicity, the weight of the flexible structure is removed from the calculation. The PD controller compensates this weight with constant feed-forward control.

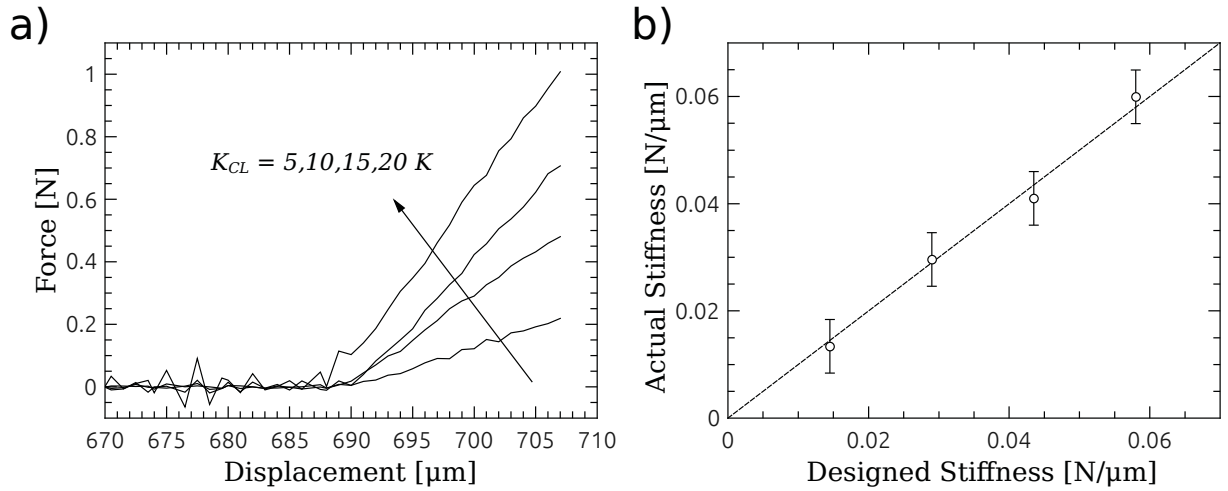

Figure 3.5: a) Force-displacement curve for a range of designed force sensor stiffness where K_{cl} is the closed-loop system stiffness and K is the flexible structure stiffness; b) Validity of the design method shown though the agreement between the actual (measured) and designed stiffness.

where the controller's proportional P and derivative D terms are calculated as follows:

$$P = K_{cl} - K \tag{3.10}$$

and

$$D = B_{cl} - B \tag{3.11}$$

The force F measured by the force sensor can be calculated either from the displacement z or the force $f_a(t)$ exerted by the voice-coil actuator:

$$F = K_{cl}z = f_a(t) + Kz = \frac{K_{cl}}{K_{cl} - K} f_a(t) \tag{3.12}$$

The PD controller is implemented digitally on the dSPACE real-time system. The Euler scheme is used to descretize the controller. Due to the relatively high cycle frequency (1 KHz), no analysis in the z-transform had to be carried out for the purposes of the present work.

3.2.3 Force sensor characteristics

In this part, the force sensor characteristics, including its stiffness, response time, resolution and vibration rejection, are discussed. The force sensor is operated while moving the Z-stage at a constant speed v, where $Z(t) = vt$.

Sensor stiffness

The stiffness K_{cl} of the closed-loop system is tuned according to Equation (3.10). Figure 3.5a shows an example of the recorded force signal in function of the Z-stage motion. In this case, the tool is positioned at a Z absolute position of 670 μm. The tool is moved towards a stiff work-piece at a speed of 10 μm/s in order that it contacts the surface, resulting in a growth of the force signal. For this example, the sensor designed stiffness is varied from 5 to 20K. The slope of the force-displacement curve allows calculating the actual force sensor stiffness. Figure 3.5b depicts the actual measured stiffness versus the designed stiffness where it shows that the actual stiffness is similar to the designed one. This ensures that the stiffness is accurately tuned over this range.

Response time

In the present work, the measured forces are contact forces (i.e. they result from tool-work piece mechanical contact). Thus, the displacement $z(t)$ of the flexible structure is imposed and in principle the sensor response time is only limited by the response time of the optical sensor (very fast, below 120 μs). However, as discussed in Section 3.1.1, the low pass filter (8th order Butterworth, 50 Hz cut-off frequency) added to the signal conditioning circuit of the force sensor causes a time delay in the force sensor response. This delay is problematic when doing dynamical force measurements as the system should react to the machining forces immediately once they occur. Therefore, quantifying this delay precisely is crucial since it has to be considered when designing the force sensor. Figure 3.6 shows an example of the unfiltered and filtered force signal in function of time and the corresponding Z-stage motion. Figure 3.6a shows that when the force signal is not filtered, the force stops growing when the pre-set threshold (0.55 N) is reached. However, when the filter is added a delay is induced, where the force grows during 20 ms above the pre-set threshold as shown in Figure 3.6b. The fact that the Z-stage motion is stopped as soon as the force threshold is exceeded (Figure 3.6c) confirms that the source of the 20 ms delay is indeed the force signal filter.

For drilling with tools smaller than 400μm in diameter, machining with minimal forces is desired to prevent tool bending or breaking. The force signal conditioning filter induces a delay of 20 ms in the fore sensor response, causing the force to grow beyond the pre-set threshold. Hence, the actual force threshold at which the motion is actually stopped has to be known relative to the pre-set force threshold. For this purpose, a calibration curve that depicts the actual threshold at which the force stops growing in function of the desired pre-set threshold is constructed for different threshold levels (Figure 3.7). For this example, the tool

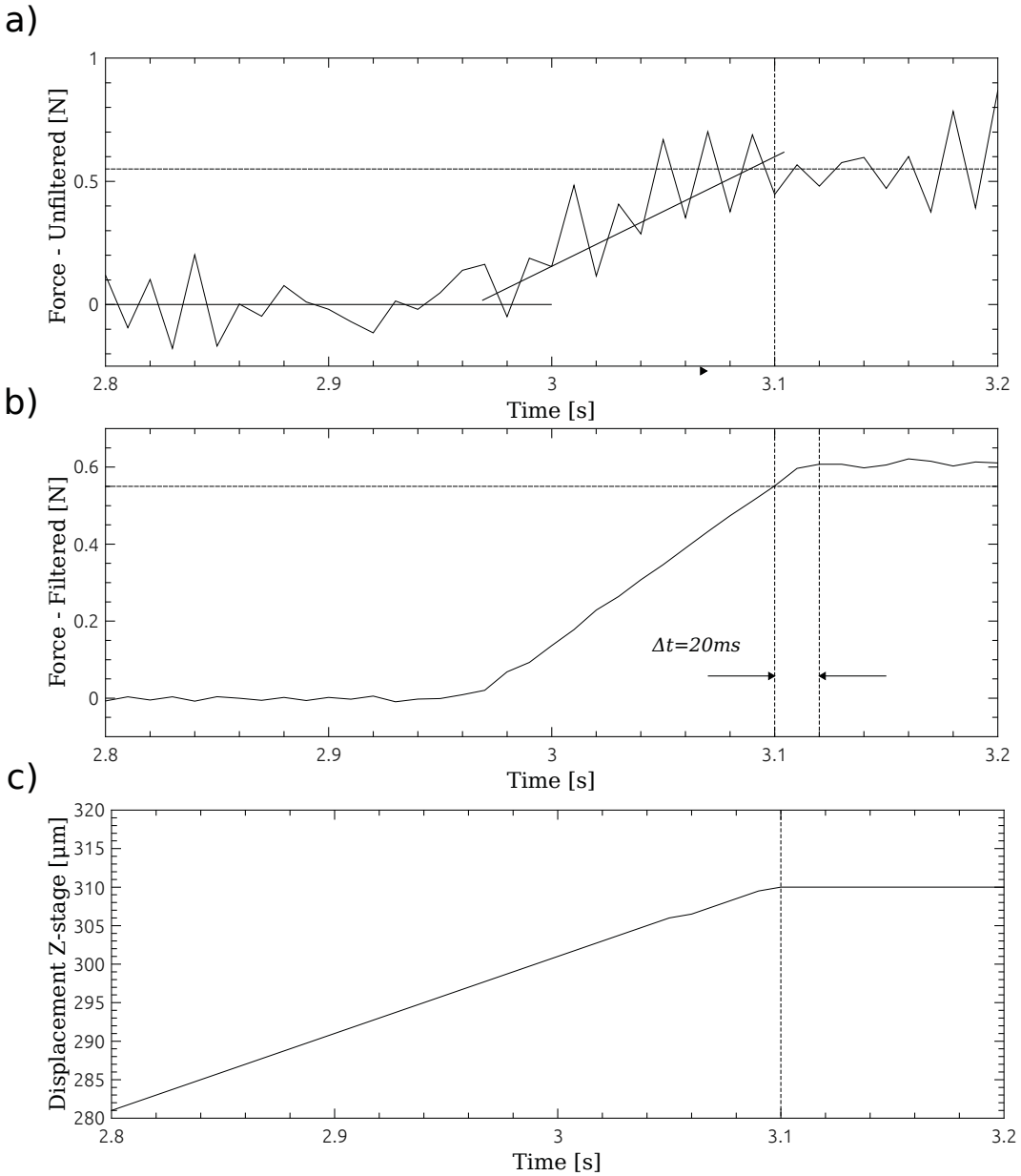

Figure 3.6: a) The recorded force signal (unfiltered), b) the filtered force signal showing the 20 ms delay that the low pass filter induces, and c) the corresponding Z-stage motion as a function of time. The Z-stage motion is stopped at the instant the force threshold (0.5 N) is crossed.

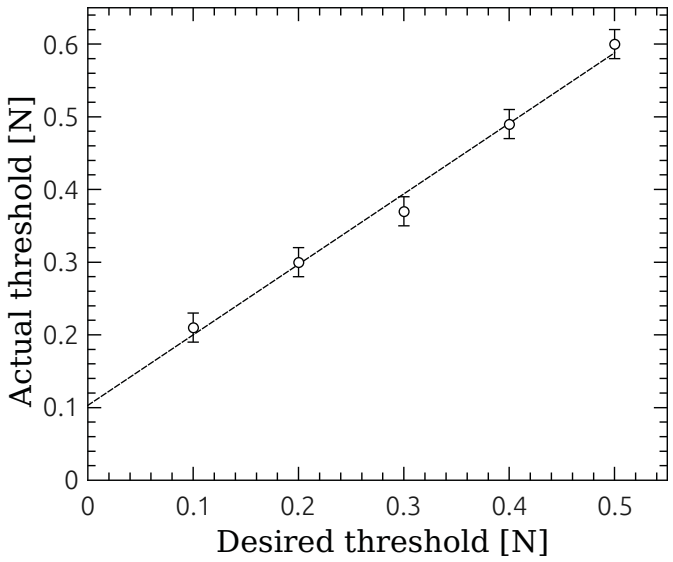

Figure 3.7: The actual force level at which the Z-motion stops in function of the pre-set force threshold. The 0.1 N offset is due to the 20 ms delay in the force response.

feed-rate is 100 μm/s and the sensor's stiffness is designed to be 16 K where K is 3000 N/m. Due to the 20 ms delay in the sensor response, a 0.1 N offset in the measured force signal results (product of the feed-rate, sensor's stiffness and the 20 ms delay). Therefore, for a desired threshold of 0 N, the resulting actual threshold will be 0.1 N. This is indeed the case as depicted in Figure 3.7.

Resolution

Filtering the force signal improves the force sensor resolution. Figure 3.8a shows an example of the recorded force signal in function of time and the normal distribution of the measured sensor noise after filtering (Figure 3.8b). The resolution of the force sensor is better than 5 mN (Figure 3.8b where it is 20 times better than that of the unfiltered signal, Figure 3.6). Detecting such small forces allows taking actions during machining to prevent tool bending or breaking, especially when using small tools.

Vibration rejection

As the force sensor will be operated while moving the Z-stage of the machining set-up, vibration rejection is an important issue to be addressed. Spectra of vibrations created due to the Z-stage motion are determined experimentally. In this case, the machining head is operated in open-loop where it is used as an accelerometer.

Figure 3.9a shows the power density spectra of the tool vibrations (z displacement mea-

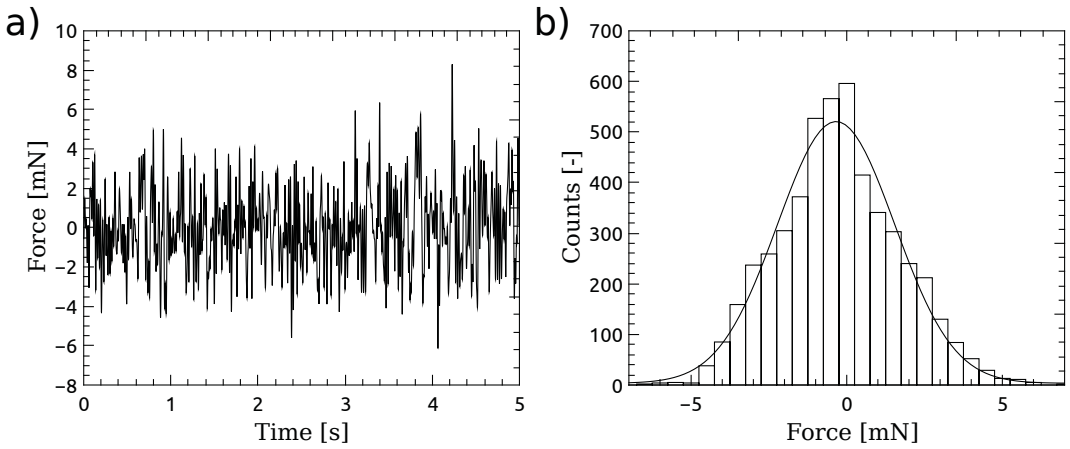

Figure 3.8: a) The recorded force signal (after filtering) in function of time and b) the normal distribution of the measured sensor noise. The sensor resolution is better than 5 mN.

sured by the optical sensor inside the flexible structure) when continuously moving the Z-axis (excluding the transients caused by starting up and ending of the motion) for various speeds from 100 μm/s to 10 mm/s while the PD controller is off. For speeds higher than 1 mm/s two major frequencies are transmitted. Peak A (8 Hz) is the eigenfrequency of the flexible structure in the machining head (Section 3.2.1) while Peak B is the frequency of the vibrations due to the lead-screw of the Z-stage. As the speed is decreased, starting from 10 mm/s, the high frequency Peak B is shifted gradually to the left and it merges with Peak A for speeds lower than 1 mm/s. Note that the amplitude of Peak B decreases as it shifts towards the eigenfrequency of the flexible structure, the last being a second order system which acts as a high-pass filter in terms of vibration transmission.

In the applications of the present work, the force-sensor will not be operated for Z-stage speeds higher than 100 μm/s. Consequently, the controller should be able to reject essentially only the eigenfrequency of the flexible-structure (8 Hz). Design of the PD controller is based on the normalized frequency response of a second order system (Figure 3.10a). In this work, we consider that attenuating the Eigen-frequency of the flexible-structure by 20 dB is sufficient. Taking this into account, it becomes possible to design the PD controller for a given damping ratio. As shown in Figure 3.10b, when taking a damping ratio ζ of 0.5 magnitude[3], 20 dB attenuation is achieved for a normalized frequency of 0.25. Hence, this implies that K_{cl} must be 16 times larger than K.

Figure 3.9b shows the power density spectra for the Z-stage continuous motion when implementing a PD controller designed for $K_{cl} = 16K$ and a damping ratio $\zeta = 0.5$. Peak A in Figure 3.9, which corresponds to the system's eigenfrequency, is eliminated when the PD

[3]Due to practical reasons (cycle time of the real-time system) it was not possible to implement higher damping ratios as the derivative term of the PD controller became too unstable.

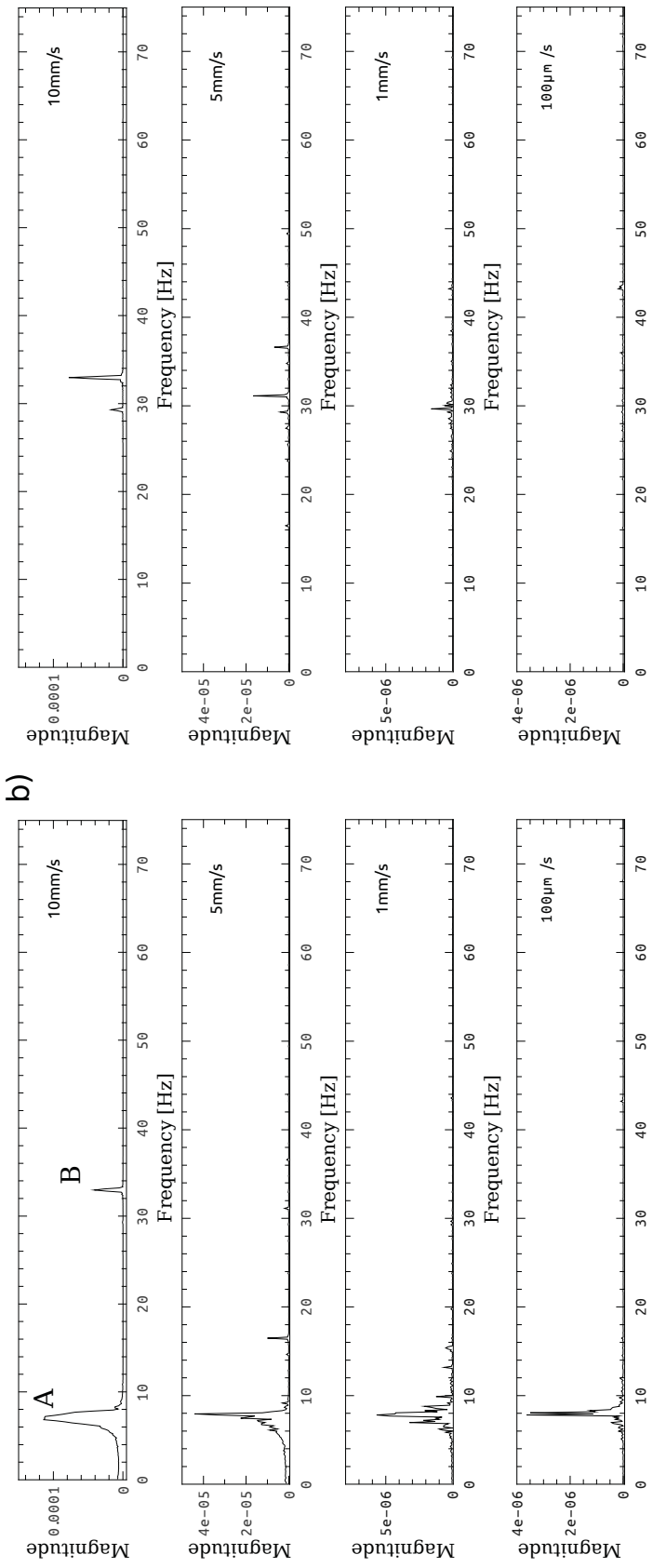

Figure 3.9: a) The power density spectra of the tool vibrations for a Z-stage continuous motion in the absence of PD controller for speeds of 100 μm/s, 1 mm/s, 5 mm/s and 10 mm/s. The plots show the machine head eigenfrequency (Peak A) and vibrations induced due to the motion of the Z-stage lead-screw (Peak B); b) The power density spectra for the Z-stage continuous motion when adding the PD controller. The machine head eigenfrequency is attenuated for all speeds while vibrations are rejected for Z-stage speeds lower than 100 μm/s.

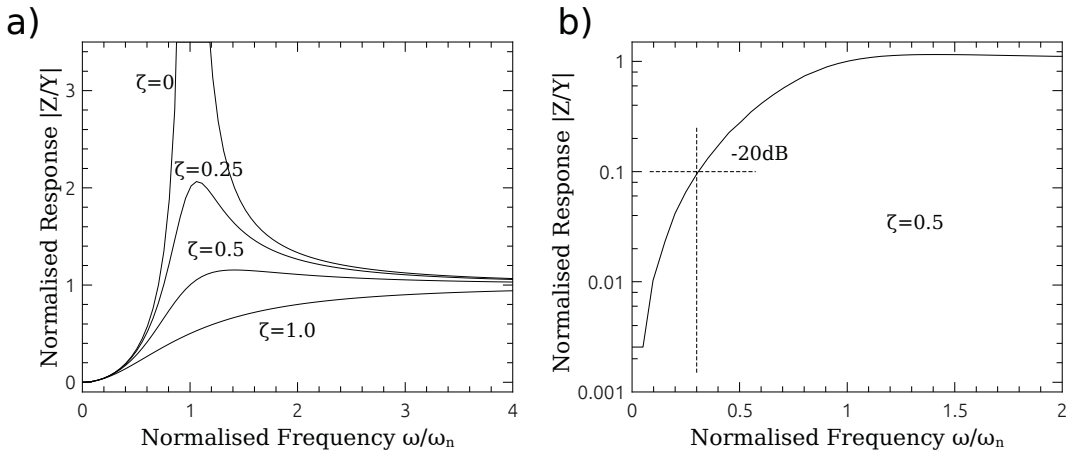

Figure 3.10: a) The normalized frequency response of a second order system for different damping ratios ζ; b) The damping ratio is chosen to be 0.5 since for higher ζ the PD controller is unstable. For this damping ratio, the chosen attenuation level (20 dB) is achieved for a normalized frequency of 0.25 implying that $K_{cl} = 16K$.

Parameter	Value
Range of tool feed-rate f (μm/s)	up to 100
Resolution (mN)	better than 5
Time delay (ms)	20
Noise attenuation level (dB)	20
Eigen frequency (Hz)	8
Stiffness range (N/m)	5 to $16K$ ($K = 3000$ N/m)
Damping ratio	0.5

Table 3.1: Properties of the designed force sensor.

controller is added. This shows that the controller acts as a high-pass filter. The vibrations coming from the Z-stage lead screw, Peak B in Figure 3.9a, are only transmitted for Z-stage travel speeds higher than 100 μm/s.

It has to be noted that the vibrations happening when starting the Z-motion are also attenuated when using this controller, as shown in Figure 3.11. As the normalized frequency is 0.25, the closed-loop frequency has to be four times higher than that in open loop ($\omega_{cl} = 4\omega_o = 32\,Hz$). As shown in Figure 3.11, the eigenfrequency is shifted to the right to 32 Hz after adding the controller, and the vibrations amplitude is reduced (due to the introduced damping). Hence, the present controller is sufficient for the work done in this thesis up to tool travel-speeds of around 100 μm/s, where no vibrations are transmitted. The force sensor properties are listed in Table 3.1.

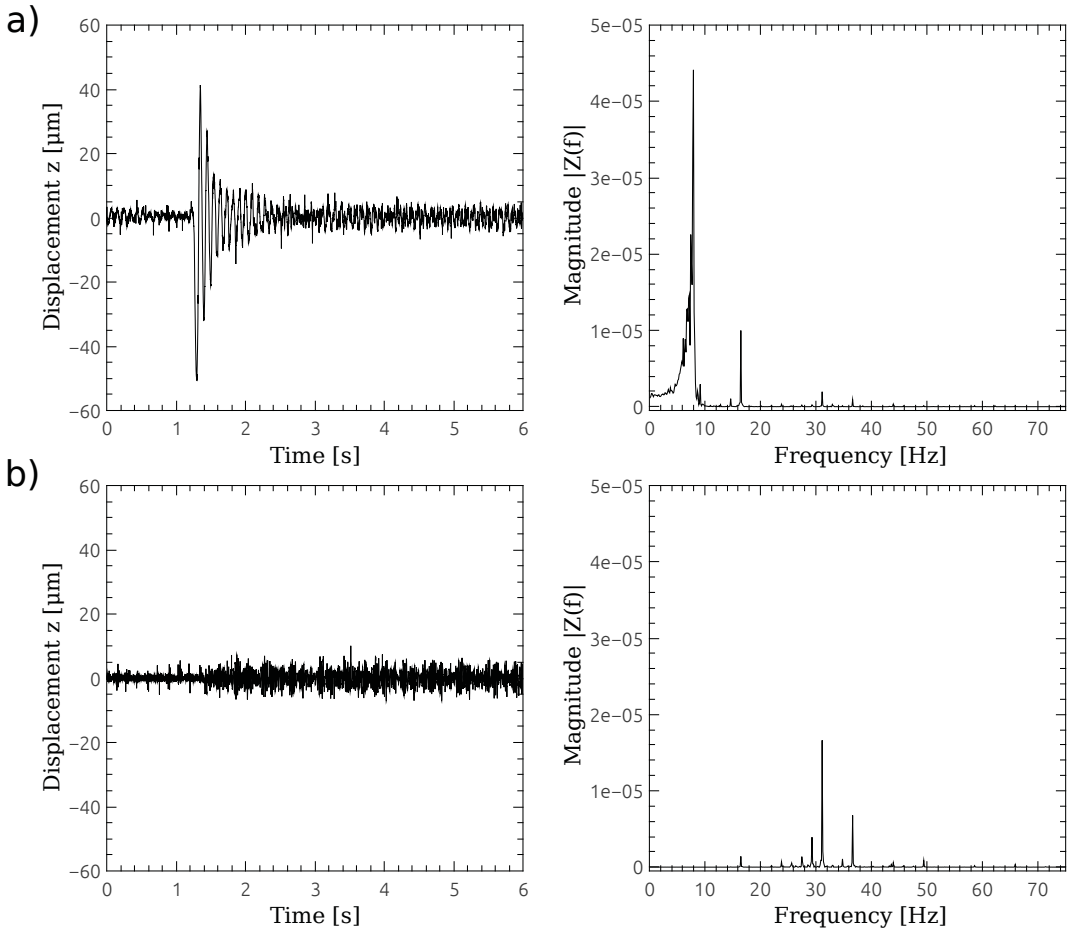

Figure 3.11: a) The vibration of the flexible structure when starting the motion and the corresponding power density spectra; b) The power density spectra after adding the PD controller.

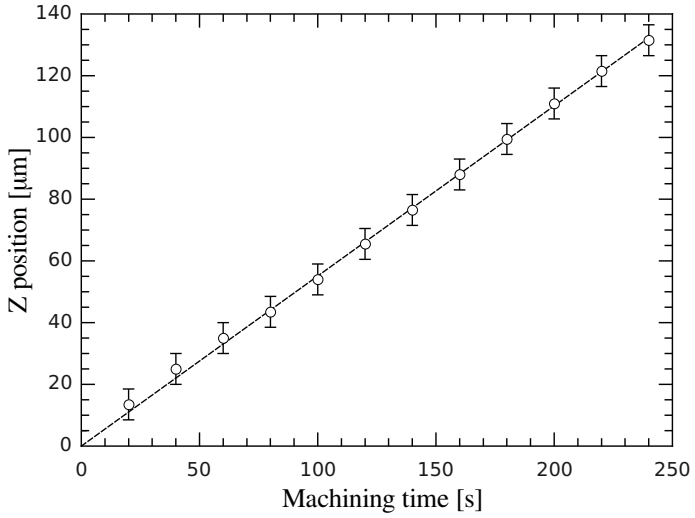

Figure 3.12: Tool wear measurements for a 400 μm diameter tungsten tool done in 30 wt% NaOH while applying 32 V. The Z-position of the Al_2O_3 work-piece is detected 12 times and between each two measurements the voltage is switched on during 20 s. The slope of this curve is the tool wear rate. Reprinted from (AbouZiki and Wüthrich, 2012) with kind permission of Springer Science and Business Media.

3.3 Measurement errors

The force sensor is designed to measure machining forces with the goal of identifying the local machining zone parameters. To properly quantify these parameters, measurement errors resulting from the tool wear, bending and thermal expansion have to be considered. As the electrolytic solution is corrosive, tool wear results. Tool bending may also occur for tool-work piece contact, depending on the tool stiffness. Further, during machining the tool expands due to the high local temperature that reaches 500 °C, as stated in Chapter 2. In this section, a methodology is developed to quantify these measurement errors. Further, a thermal model that identifies the heat distribution in the machining zone is built. The measured tool thermal expansion matches that predicted by the model.

3.3.1 Tool wear and bending

A methodology to measure the tool wear and bending is developed and presented. These measurements have to be considered while quantifying the tool thermal expansion.

Tool wear

In order to measure the tool wear, the work-piece is required to be chemically resistant to the electrolytic solution. Alumina (Al_2O_3), which is known to resist etching by electrochemical

Voltage range	Tool wear average value (μm/s)		
	Tungsten	Steel	Stainless Steel
28-33 V	0.54	0.06	0.02

Table 3.2: Tool wear (μm/s) for the three 400 μm diameter tool-electrodes: tungsten, steel and stainless steel. Stainless steel exhibits the minimal wear. Reprinted from (AbouZiki and Wüthrich, 2012) with kind permission of Springer Science and Business Media.

discharges for voltages below 40 V according to (Bhattacharyya et al., 1999; Wüthrich, 2009; Tsutsumi et al., 1993; Chak and Venkateswara Rao, 2007), is used as the work piece. To confirm that alumina resists etching, a voltage of 33 V is applied during 5 min. Visual observation of the work piece with an optical microscope showed no traces of etching on the alumina surface.

For the present experiments, the machining head is used in the profile-meter mode. The error in the tool's vertical motion (Z-motion) is below 1 μm (Section 3.1.1). To measure the tool wear, the Z-position of alumina work-piece, denoted by *initial Z*, is identified (using the profile-meter mode of the machining head). The tool is moved away from the surface and the voltage is switched on during a certain time. The Z-position of the alumina work-piece is detected afterwards. The difference between the initial Z and the position at which the surface is detected the second time, gives the length by which the tool is shortened during a certain time, implying the tool wear. This measurement is repeated 20 times for each tool (400 μm diameter tungsten, steel and stainless steel) and machining voltage (28 to 33 V; 1 V increments). The Z-position of the Al_2O_3 work-piece recorded in function of machining time for a tungsten tool while applying 32 V is shown in Figure 3.12 for 12 consecutive measurements.

Table 3.2 depicts the average tool wear for the three electrode materials for a range of machining voltages. The highest tool wear is for tungsten where it is in average around 0.5 μm/s. The stainless steel tool exhibits minimal wear which is around 0.02 μm/s. This shows that stainless steel is the most compatible tool-electrode material for SACE drilling due to its high chemical resistance. Consequently, stainless steel tools are used throughout this work.

Tool bending

The tool bending is quantified for a 0.5 mm diameter stainless steel tool since this tool material is used throughout the present thesis work (exhibits minimal wear). To measure tool bending, the tool is moved downwards starting from an arbitrary origin of the coordinate system (corresponding Z-position is denoted by Z_o). The tool is brought in contact with the glass surface causing the flexible structure to deflect, hence changing the output voltage

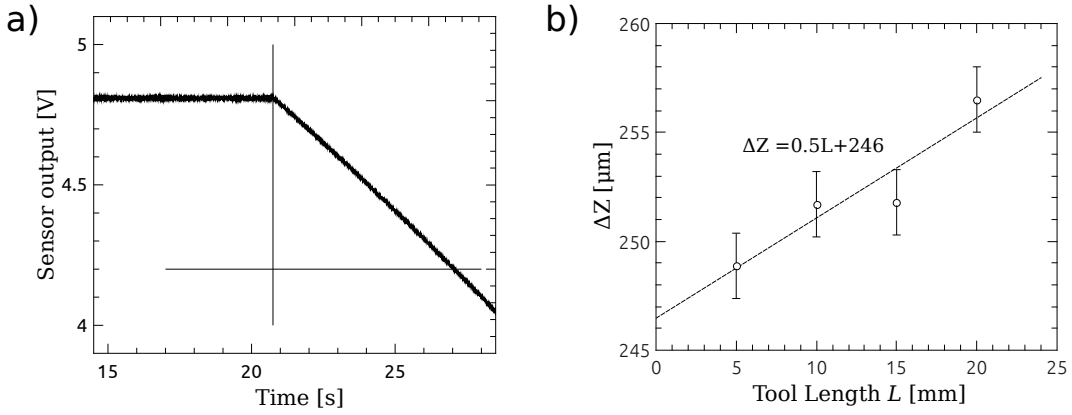

Figure 3.13: a) An example of the recorded optical sensor signal for tool bending quantification. The tool is initially away from the glass (optical sensor 4.8 V output). To measure bending, the tool is moved by Δz to touch the glass surface at 4.2 V (measurement repeated 20 times). b) Tool bending for a 0.5 mm diameter stainless steel tool in function of the tool length.

of the optical sensor circuit. The position at which the tool contacts the glass surface, corresponding to a threshold of 4.2 V in this case (Figure 3.13a), is denoted by Z_i. The tool is moved back to Z_o following each measurement. The same procedure is repeated 20 times for a specific tool length where for each measurement the force and the optical sensor signals are recorded. An example of the recorded optical sensor signal in function of the Z-position is depicted in Figure 3.13a. ΔZ, which is the distance from Z_i to Z_o, is extracted for each measurement where it represents the average tool bending. The tool bending measurement is done for different tool lengths L ranging from 5 to 20 mm. Figure 3.13b depicts ΔZ in function of the tool length where the resulting ΔZ is $0.5\,L$ (L in mm and ΔZ in μm). For the used tool, the stiffness K_{tool} (N/μm) is equal to $1.38L^{-1}$. Therefore, for 10 mm long tool, the tool stiffness is around 0.14 N/μm which is 3 times higher than the stiffness of the PD controller (around 0.048 N/μm). When extrapolating ΔZ to zero tool length the resulting ΔZ is around 246.5 μm. This value is the absolute position (with respect to Z_o) at which the glass surface is detected, before bending occurs.

3.3.2 Tool thermal expansion

In the context of SACE, the thermal expansion of the tool was never studied so far. In this section, a thermal model that predicts the tool temperature is built. Further, a methodology to measure the tool thermal expansion is developed. Expansion measurements are corrected for errors resulting from tool wear and bending. The validity of the present methodology is confirmed by matching the measured expansion with that predicted by the thermal model.

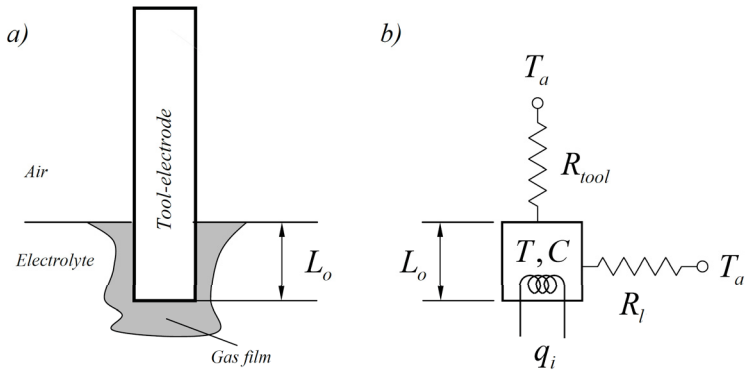

Figure 3.14: a) Schematic of the tool-electrode during machining (L_o is the tool length dipped in the electrolyte); b) The thermal model that predicts the tool temperature. q_i is the average discharge power, T_a is the ambient temperature, T is the tool tip temperature, C is the tool heat capacitance, R_l and R_{tool} are the thermal resistances of the electrolyte and tool respectively. Reprinted from (AbouZiki and Wüthrich, 2012) with kind permission of Springer Science and Business Media.

Thermal model

In order to determine the tool temperature, a thermal model that estimates the tool temperature is developed (Figure 3.14). During SACE machining, discharges are generated at the electrode's sharp edges through the gas film. This causes the tool to heat up. The length of the tool heated up by the discharges is assumed to be the part dipped in the electrolyte and is considered to have a heat capacitance C. Part of the generated heat is dissipated through the upper part of the tool as well as the electrolyte in the tool's vicinity. Both the thermal resistances of the electrolyte, R_l, and the upper part of the tool, R_{tool}, are lumped in the model as an equivalent resistance R. The heated tip, of temperature T, is connected to the ambient temperature, T_a, through these resistances. Based on these considerations, the change in the tool's temperature can be written as:

$$\frac{dT}{dt} = \frac{1}{C}\left[q_i\left(t\right) - \frac{1}{R}\left(T - T_a\right)\right] \tag{3.13}$$

The heat capacitance of the tool's tip is expressed in terms of the tool-electrode's density ρ_{tool}, diameter d, specific heat σ_{tool}, and the length L_o heated up (around 1 mm) as:

$$C = \rho_{tool}\pi\left[\frac{d}{2}\right]^2 L_o\sigma_{tool} \tag{3.14}$$

The tool resistance is written in terms of its length L, thermal conductivity λ_{tool}, and diameter d while the electrolyte's thermal resistance is a function of its thermal conductivity λ_l

and the tool's diameter d (considering a half sphere volume). The tool's and electrolyte's resistances are considered to be in parallel and are estimated individually by the following equations respectively:

$$R_{tool} = \frac{4L}{\lambda_{tool}\pi d^2} \tag{3.15}$$

$$R_l = \frac{1}{\lambda_l \pi d} \tag{3.16}$$

The thermal resistance of the tool-electrode is large (more than $3500\,\mathrm{KW}^{-1}$ for 2 cm long steel and stainless steel tools based on Table 3.3) compared to that of the electrolyte ($900\,\mathrm{KW}^{-1}$ for 30 wt% NaOH), most of the heat is dissipated through the electrolytic solution. Hence, the equivalent resistance is considered to be solely that of the electrolyte ($\mathrm{R} \approx R_l$).

The solution of the first order model, Equation (3.13), grows exponentially with the following time constant:

$$\tau = RC \cong \frac{\rho_{tool}\sigma_{tool}}{\lambda_l}\frac{d \cdot L_o}{4} \tag{3.17}$$

For long enough time, the change in tool temperature reaches a stationary value ΔT considering that the heat supply is constant:

$$\Delta T = T\left(t \to \infty\right) - T_a = Rq_i \cong \frac{q_i}{\lambda_l \pi d} \tag{3.18}$$

The average discharges' power q_i is written, based on shot-noise theory (Wüthrich, 2003, 2009), in terms of the machining voltage U, the mean number of discharges per time n_d, the mean discharge duration τ_d and the mean discharge amplitude I_d as:

$$q_i = U \cdot \bar{I} = n_d \tau_d I_d U \tag{3.19}$$

For 30 V machining voltage, $\bar{I}$ is found experimentally (based on electric current signal recordings) to be around 0.01 A.

Tool expansion measurement

For measuring the tool thermal expansion, the profile-meter mode of the machining head is used to find the glass surface. The tool is moved away from the work piece by 50 μm and two steps are executed (one at a time):

1. The tool is moved 100 μm downwards toward the work piece at 5 μm/s while the voltage is off (dry experiment).

2. The voltage is switched on during 3 s and the tool is moved 100 μm downwards toward

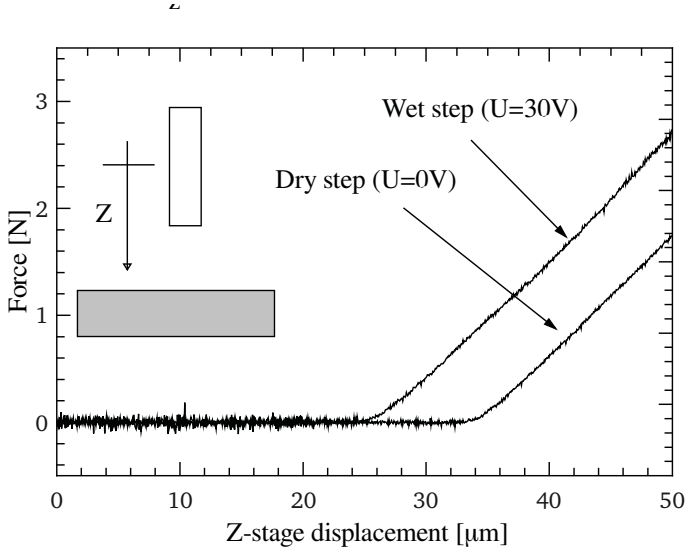

Figure 3.15: Thermal expansion measurement for a 500 μm diameter stainless steel tool while applying 30 V. The tool is moved downwards to detect the glass surface while: a) the voltage is switched on (wet step) and b) while the voltage is off (dry step). The difference between the two measurements (9 μm) is the tool thermal expansion. Reprinted from (AbouZiki and Wüthrich, 2012) with kind permission of Springer Science and Business Media.

the work piece at 5 μm/s while the voltage is still on (wet experiment).

The initial voltage is applied during 3 s to ensure that the tool reaches the stationary thermal expansion which is estimated to happen during 0.7 s based on Equation (3.17) for a machining voltage of 30 V. During both the dry and wet experiments, the force signal is recorded using the force sensor mode (5 mN resolution) of the machining head (Section 3.2.3). The experiments are repeated 20 times to ensure measurement repeatability.

Figure 3.15 depicts an example of the recorded force signals for both the dry and wet experiments. For the dry experiment the surface is detected after moving downwards by 34 μm. For the wet experiment, the surface is detected after a downward motion of 25 μm. The difference between the Z-position at which a force is detected in case of dry and wet experiments is 9 μm. This value is the thermal expansion of a 500 μm stainless steel tool for 30 V machining voltage. For these experiments, it is not required to correct for tool bending as in both dry and wet steps the same bending occurs.

Validation

The tool thermal expansion for the three electrodes (stainless steel, steel and tungsten) is measured. Twenty experiments are done for each condition. To have similar initial conditions for all the tool-expansion measurements, the tool is cooled down to room temperature between consecutive measurements. Therefore, expansion measurements are separated by 20 s

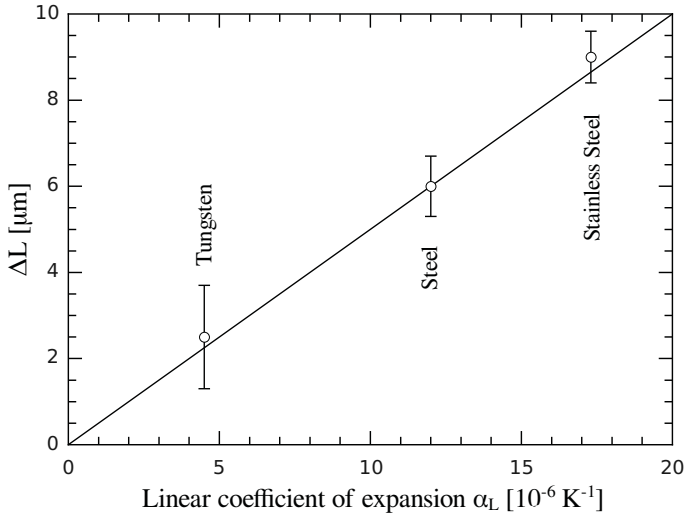

Figure 3.16: The average value of the thermal expansion in function of the linear coefficient of expansion for three electrodes: tungsten, steel and stainless steel. Twenty measurements are done for each material. Reprinted from (AbouZiki and Wüthrich, 2012) with kind permission of Springer Science and Business Media.

	Linear expansion coefficent α_L [K^{-1}]	Density ρ [kg·m^{-3}]	Thermal conductivity λ [W·m^{-1}·K^{-1}]	Specific heat σ [kg·K]
Stainless steel	$4.5 \cdot 10^{-6}$	8030	26	510
Steel	$12.0 \cdot 10^{-6}$	7850	46	420
Tungsten	$17.3 \cdot 10^{-6}$	19600	167	134

Table 3.3: Properties of the three tool-electrode materials: stainless steel, steel and tungsten. Reprinted from (AbouZiki and Wüthrich, 2012) with kind permission of Springer Science and Business Media.

during which fresh electrolyte is added to the cell to rapidly cool down the tool. The average value of the thermal expansion for each tool is plotted in Figure 3.16 in function of each material's thermal expansion coefficient (Table 3.3). The relation between these two entities is linear. This result matches with the Equation (3.20) where the change in length ΔL is proportional to the initial length of the tool L_o, the coefficient of thermal expansion α_L and the change in temperature ΔT:

$$\Delta L = \alpha_L L_o \Delta T \tag{3.20}$$

From Figure 3.16, the tool-tip temperature is estimated to be around 500 °C for a 1 mm tool length dipped in the electrolyte. This temperature matches with the one calculated from Equation (3.18) by substituting 0.3 W for q_i, calculated based on Equation (3.19) by taking the average current to be 10 mA (as measured for 30 V machining voltage).

Further, the estimated local temperature agrees well with the temperature measured with thermocouples (Kellogg, 1950), by spectroscopic measurements (Reghuram, 1994) and through local glass viscosity estimation (Jalali et al., 2009). For quantifying the tool expansion, the work-piece expansion is not considered. The agreement between the temperature estimated based on the measured expansion (Figure 3.16) and that predicted by the thermal model (Equation (3.19)) shows that the work piece expansion, which is not considered when measuring the tool expansion, is negligible. Hence, no further attempt is done to quantify the glass work piece expansion.

To ensure that the tool expansion is measured properly, such that after the tool reaches its expansion limit, the following measurement is done. The voltage, 30 V, is switched on during 15 s and the voltage signal is recorded in function of time (Figure 3.17). A stainless steel tool is used as it exhibits negligible wear compared to the other two tools (Table 3.2). Figure 3.17 shows that about 0.5 s is needed for the tool to reach its expansion limit. During this short time, the tool expands exponentially as predicted by the first order thermal model, Equation (3.13). The measured data is fitted by least square regression to the first order thermal model as shown in the inset of Figure 3.17. This results in a time constant of around 0.3 s which is in the same order of magnitude as the one calculated from Equation (3.17) (0.7 s for the present machining conditions). The agreement between the measured tool expansion and that predicted by the thermal model ensures the validity of the expansion measurement method.

Application

The method developed to measure the tool thermal expansion can be used to control the tool temperature, hence the machining zone temperature during machining. When varying the machining voltage amplitude or duty cycle, the tool temperature is influenced. By knowing the change in the tool length (measured based on the developed methodology), the tool temperature can be estimated with Equation (3.20). The change in a stainless steel tool length (0.5 mm diameter) for different machining voltage and duty cycles (20 ms pulse-on-time) while using 30 wt% NaOH is plotted in Figure 3.18. The behaviour of ΔL in function of the voltage amplitude (Figure 3.18a) or the duty-cycle (Figure 3.18b), which are directly related to the tool temperature, is linear which is consistent with Equation (3.20). The present results allow varying the machining zone temperature which is a crucial factor in SACE machining process.

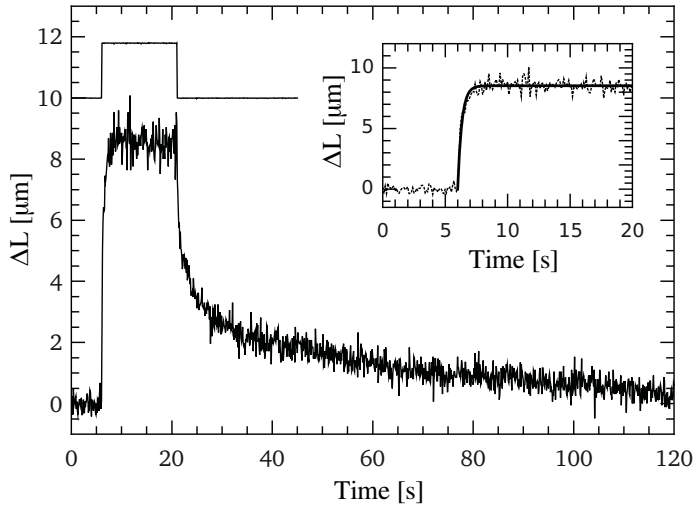

Figure 3.17: Change in tool length ΔL in function of time for 500 μm stainless steel tool while applying 30 V during 15 s. The tool reaches its expansion limit in 0.5 s. The inset shows the fit of the first order thermal model to the measured data, where a time constant τ of 0.3 s results. Reprinted from (AbouZiki and Wüthrich, 2012) with kind permission of Springer Science and Business Media.

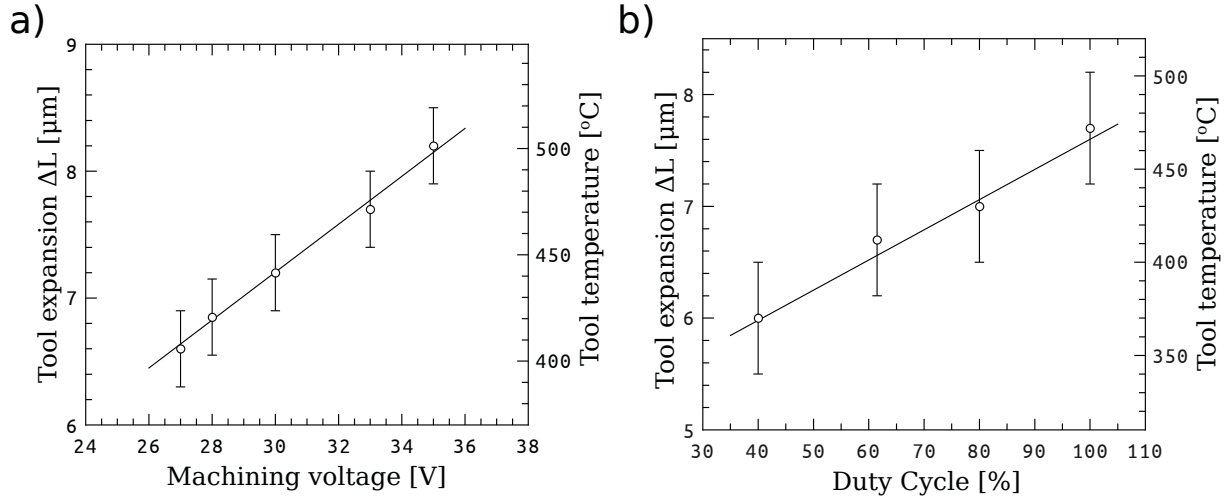

Figure 3.18: Change in length ΔL of a 0.5 mm diameter stainless steel tool in function of the a) voltage amplitude and b) voltage duty cycle. Different tool temperature results when varying the voltage amplitude or duty cycle. Reprinted from (AbouZiki and Wüthrich, 2012) with kind permission of Springer Science and Business Media.

Chapter 4

Drilling forces characterization

Destiny is not a matter of chance,
it is a matter of choice; it is not a thing
to be waited for, it is a thing to be achieved.
(-Kitty Kolding)

Following the force measurement methodology developed in Chapter 3, machining forces occurring under different machining conditions during constant-velocity-feed drilling are measured and characterized. Accordingly, it is found that the lack of both local heating and flushing limits the material removal rate during SACE machining. Plots depicting the force regions in the tool feed-rate versus hole-depth plane are constructed for various machining conditions. These plots are superposed on one dimensionless plot when considering the effect of both flushing and heating. The dimensionless curve allows choosing the machining parameters in function of the required machining depth so that the drilling operation can be performed with almost zero forces. The present novel finding permits drilling without forming deteriorated surfaces (deformed surfaces, cracks and heat affected zones). It is further demonstrated, for the first time in the field of SACE drilling, that the tool can bond to the glass surface while machining. This bond is detected based on the recorded force signal.

4.1 Local heating and flushing

In constant-velocity-feed drilling, forces will be exerted on the tool whenever tool-glass surface mechanical contact occurs. This contact is a result of insufficient material removal rate compared to the tool feed-rate. To understand the origin of the forces, called *drilling forces* in this text, it is necessary to better understand the factors leading to poor material removal rates in SACE drilling.

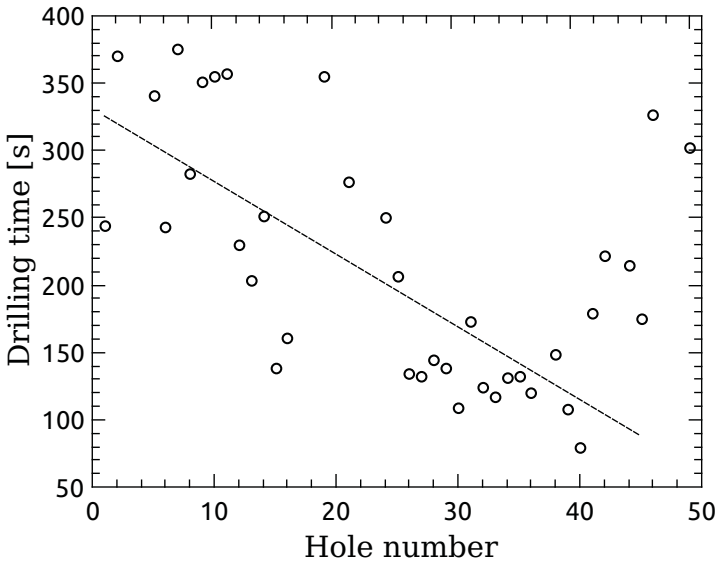

Figure 4.1: The recorded drilling time for fifty 400 μm deep holes machined in 50 wt% KOH solution while applying 30 V and using 250 μm diameter tool moved at 50 μm/s. Drilling time decreases as more holes are drilled.

It is known from gravity-feed drilling that for depths reaching 100-200 μm, drilling evolves at high rate (discharge regime) and becomes negligible for depths higher than 300 μm due to limited flushing (hydrodynamic regime) (Jalali et al., 2009). During the discharge regime when drilling with a 400 μm tool-electrode, machining rate reaches about 80 μm/s when applying 33 V and it decreases to 50 μm/s for lower voltage (30 V) (Wüthrich, 2009). The variable machining rate is due to the variation in the tool-electrode temperature for different machining voltages which influences the local machining zone temperature. Studies from gravity-feed machining also showed that it takes significantly longer time to machine the first few holes in a row of sequentially drilled holes (Morrison, 2009). This is probably due to the increased local temperature of the glass and electrolyte as drilling progresses which causes accelerated machining.

The importance of local heating can be observed as well in the case of constant-velocity-feed drilling configuration, that is used throughout this thesis work. During this drilling configuration, the tool is moved towards the glass at a constant feed-rate (no forced contact with the glass surface). For a reduced material removal rate, as the tool feed-rate becomes faster than the etching progress, forces are exerted on the tool due to mechanical contact between the tool and the glass surface. Figure 4.1 shows the recorded drilling time during constant-velocity-feed drilling for an array of 50 holes, 400 μm deep, drilled in 50 wt% KOH using 250 μm diameter tool. Prior to drilling, the tool is positioned 50 μm above the glass surface (detected using the profile-meter function of the machining head). The tool is moved

at 50 μm/s while applying 30 V. To ensure that the holes are drilled starting from the same initial conditions, an overflow system is used, as described in Section 3.1.1, to keep the electrolyte level constant. Results show that, similar to the case of gravity-feed machining, the drilling time decreases as more holes are machined which is due to the increased local temperature causing faster drilling.

Heating is crucial for machining but local flushing has to be equally important. In fact, this can be seen in the studies conducted by (Han et al., 2011) regarding the relation dependence of the surface roughness on the tool feed-rate. The results showed that during constant velocity feed-drilling the surface roughness and the tool feed-rate follow an inverse volcano relationship. This implies that very low or high tool feed-rates result in similar machined surface roughness. The similarity in the surface roughness for very low or high tool feed-rates can be explained as follows. For low feed-rates, the slow tool motion causes the local hot electrolyte to circulate in the machining zone during a longer time which causes formation of heat affected zones and widening of the hole entrance diameter. For high tool feed-rates, the tool continuously contacts the surface. This causes, on one side, enhanced heat transfer to the surface and, on the other side, disturbed gas film formation at the tool tip and reduced local flushing. The last limits the machining progress resulting in non-uniform machined surface. This shows that balancing both heating and flushing during SACE has to be the key to enhanced machining rate and surface quality.

Based on these observations, it is claimed that for machining to progress efficiently two elements are needed: continuous electrolyte supply in order to etch (flushing) and high temperature to accelerate etching. While flushing is expected to enhance the machining efficiency, excessive flushing must result in local heat dissipation. A direct consequence of this claim is that machining rate has to be slower when drilling with an eccentric tool while applying tool rotation. This is indeed the case where when using tools of different eccentricities, the depth at which forces start to appear differs. For these experiments, prior to machining, the glass is detected using the profile-meter function of the machining head. The tool is positioned 50 μm above the glass surface and it is moved downwards at a constant speed of 10 μm/s while adding 2000 rpm tool rotation and applying 30 V. Holes are drilled in 50 wt% KOH solution. Results show that for a tool eccentricity of around 100 μm, the machining forces appear starting from 120 μm depth compared to 160 μm when reducing the tool eccentricity to around 50 μm. Further, when fixing the machining conditions for increased tool rotational speeds above 1000 rpm forces appear, in average, at a lower depth. This effect is more apparent for increased tool eccentricity. These findings prove the validity of the theory that efficient machining implies achieving a good balance between local heating and sufficient flushing to enable etching.

A characteristic number which falls into the category of local heating issue is the time t_o needed to initially heat the glass surface to the required temperature for machining to proceed. This time can be estimated based on the solution of a simple thermal model that predicts the heat propagation to the glass surface. The model considers the heat from the discharges as a cylindrical heat source.

The time t_o needed to heat the glass surface is given by (Jalali et al., 2009; Wüthrich, 2009) in function of the normalized heat power κ:

$$t_o = \frac{\kappa^2 r^2}{4\pi\alpha\left(\kappa - 1\right)^2} \tag{4.1}$$

where α is the work-piece thermal diffusivity and r the tool radius. κ is the ratio between the heat P_o transferred to the surface and the minimum one P_{min} required to machine. P_o is expressed in terms of the machining voltage U, not including the voltage U_d needed to decompose the water to hydrogen and oxygen, and in terms of the current I flowing between the electrodes as:

$$P_o = \left(U - U_d\right) I \tag{4.2}$$

The current is approximated to be around 0.01 A for a 400 μm tool based on (AbouZiki and Wüthrich, 2012).

P_{min} is expressed, based on (Jalali et al., 2009; Wüthrich, 2009), in function of the work-piece thermal conductivity λ, the temperature difference ΔT between the ambient temperature and that needed to machine glass T_M, and the tool's radius r as:

$$P_{min} = \lambda \Delta T \pi r \tag{4.3}$$

Equation (4.1) shows that the time needed to heat the surface depends on the tool radius. For reduced tool radius the discharges are more concentrated at the tool tip. This results in a smaller initial heating time (increased etching rate) which prevents tool-surface contact as soon as glass machining starts. Likewise, it is expected that the depth at which forces occur must be higher for smaller tools.

Based on these considerations, it is expected that forces appear for certain depths while constant velocity-feed drilling depending on the machining conditions. For low tool feed-rates, faster material removal must result for the first few hundred microns since sufficient time will be available to heat the glass surface and to flush the hole. This effect has to be enhanced upon using smaller tools (more concentrated discharges) or when applying higher machining voltage which result in higher local temperature. Flushing must become limited at certain drilling depths causing reduced material removal rate and repeated tool-glass

Parameter	Tool diameter	
	500 μm	250 μm
Voltage (V)	30, 33	30
Tool Feed-Rate (μm/s)	1 to 5 and 1 to 30	1 to 70

Table 4.1: Machining conditions applied while characterizing the drilling forces.

surface contact. The depth at which flushing is considered to be limited has to be dependent on the machining conditions, mainly the voltage, tool feed-rate and the tool radius which directly affect the local temperature. Consequently, during drilling forces must occur at different depths which vary depending on the machining conditions. The depths at which forces occur are denoted as *force regions* in this text.

4.2 Characterization of drilling forces

To validate the presented theory regarding the influence of heating and flushing on machining, holes are drilled using different machining conditions as presented in Table 4.1 while recording drilling forces. It is expected that when increasing the voltage and reducing the tool feed-rates less drilling forces must result due to the enhanced local heating and flushing.

Fifty holes are drilled for each set of machining conditions. The machining head is used in its force sensor mode to measure forces, as described in Section 3.2. Prior to drilling, the tool is positioned 50 μm above the work piece (surface detected using the profile meter mode of the machining head), and it is moved towards the surface at a constant feed-rate while the voltage is switched on.

4.2.1 Drilling forces in function of drilling depth and tool feed-rate

Figure 4.2 shows the waterfall plots of the recorded forces for 250 μm deep holes drilled using a 500 μm tool while machining at 30 V. Each waterfall plot corresponds to a certain tool feed-rate, where feed-rates are chosen starting from the lowest possible feed-rate allowed by the experimental set-up (based on the Newport stages' specifications) up to a feed-rate at which high forces occur which result in a continuous tool-glass surface contact while machining (forces cannot be removed). Results show that for low feed rates (less than 1 μm/s in case of 30 V) forces appear after 200 μm depth. For tool feed-rates between 2 and 3 μm/s forces start appearing after moving the tool downwards by 40 μm although the tool is initially positioned 50 μm above the glass surface. This early detection of the surface is due to the tool thermal expansion that reaches 10 μm as shown in Section 3.3.2. For tool feed-rates

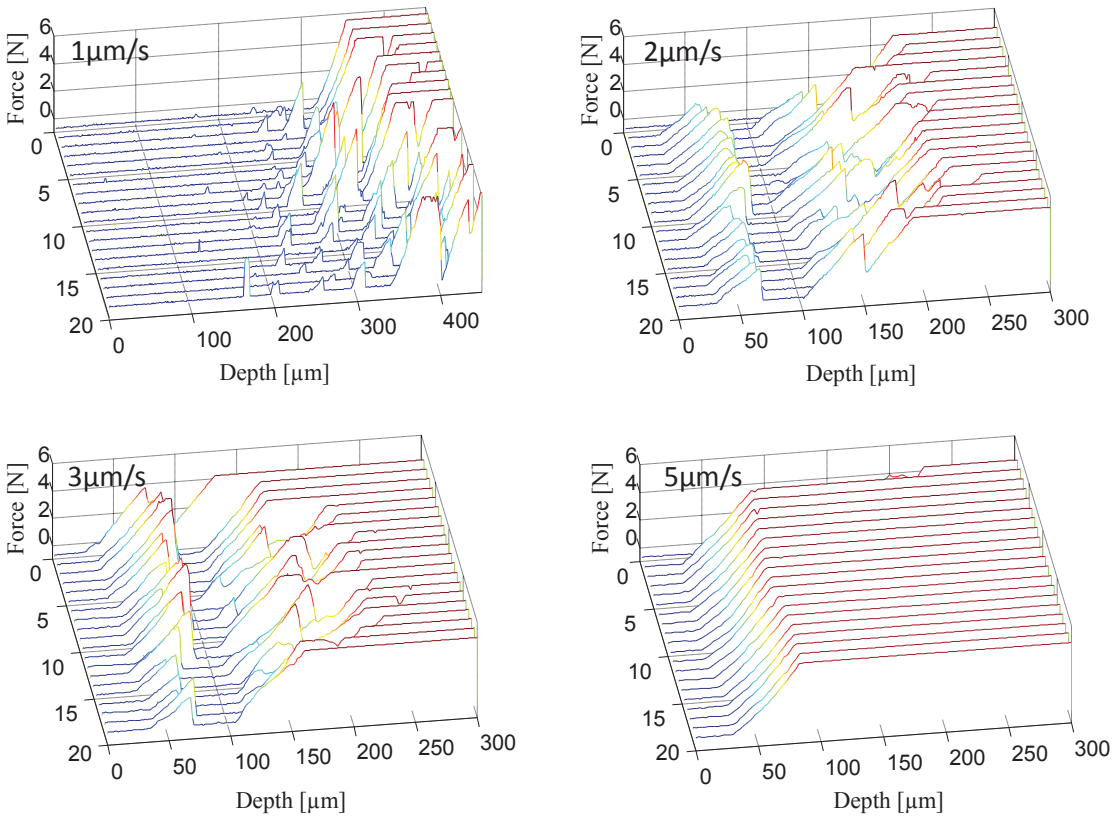

Figure 4.2: Waterfall plots showing the occurrence of forces in function of drilling depth for various tool feed-rates when using a 500 μm diameter tool-electrode and applying 30 V. The tool is positioned 50 μm above the glass surface prior to drilling and is moved at a constant feed-rate. Each waterfall plot is constructed from 20 measurements and corresponds to a certain tool feed-rate. The material removal rate is negligible for feed-rates higher than 5 μm/s (force does not recover). The force sensor saturates at a force of 6 N. Reprinted from (AbouZiki and Wüthrich, 2013) with permission from Elsevier.

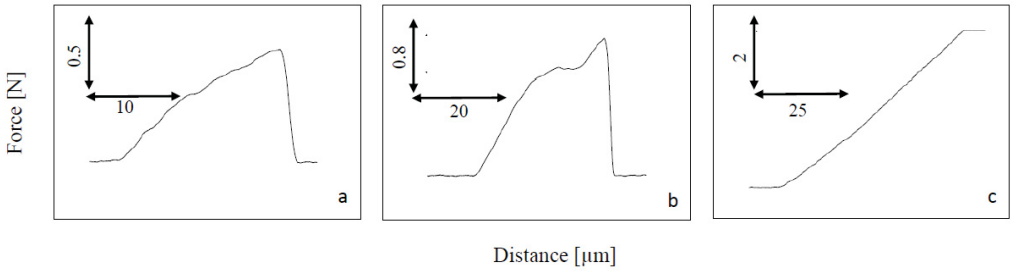

Figure 4.3: The three forms that the measured forces can take. The difference between the three shapes is the slope of the force signal which is determined by the etching progress. Reprinted from (AbouZiki and Wüthrich, 2013) with permission from Elsevier.

above 5 μm/s, forces appear as soon as the tool reaches the glass surface and they never recover for the currently used set-up. The forces detected as soon as the tool reaches the initial glass surface position, are denoted in the present text as *surface forces*.

As the surface forces recover, drilling proceeds with almost zero forces down to a certain depth (around 60 μm) where forces appear again and do not recover afterwards. These forces are called in this text *high depth forces*. It can be noticed that as the feed-rate is increased, the region between the first and second force occurrence, denoted as *middle region*, shrinks in width until the high depth forces occur at the glass surface (in this case for 5 μm/s). The high depth forces are a result of negligible material removal rate. It can be noted that the measured forces appear in one of the three forms shown on Figure 4.3. The difference between the three shapes is mainly the slope of the force signal, which is determined by the etching progress. Progressive etching at a constant rate results in (a) while a constant etching rate followed by a region where etching is accelerated (force does not grow during a certain time) and then by a region of reduced material removal rate (higher force) occur in (b). When the etching rate is negligible, the third type results (c). In this case, the slope depicts the stiffness of the overall set-up including the tool.

Based on these observations, forces can be categorized into three zones in function of the drilling depth. In the first zone, surface forces occur which recover in few seconds. The appearance of surface forces must be due to insufficient local heating causing a reduced etching rate. This zone does not exist for machining conditions enabling high enough heat transfer to the glass surface (low feed-rate, small tool, high voltage). In the second zone, almost no forces are measured. In the third zone, forces grow to high values where they cannot recover afterwards. These forces occur at high depths and have to be the result of inappropriate flushing where the lack of OH radicals prevents etching.

This analysis supports the claim that machining forces appear due to insufficient heating

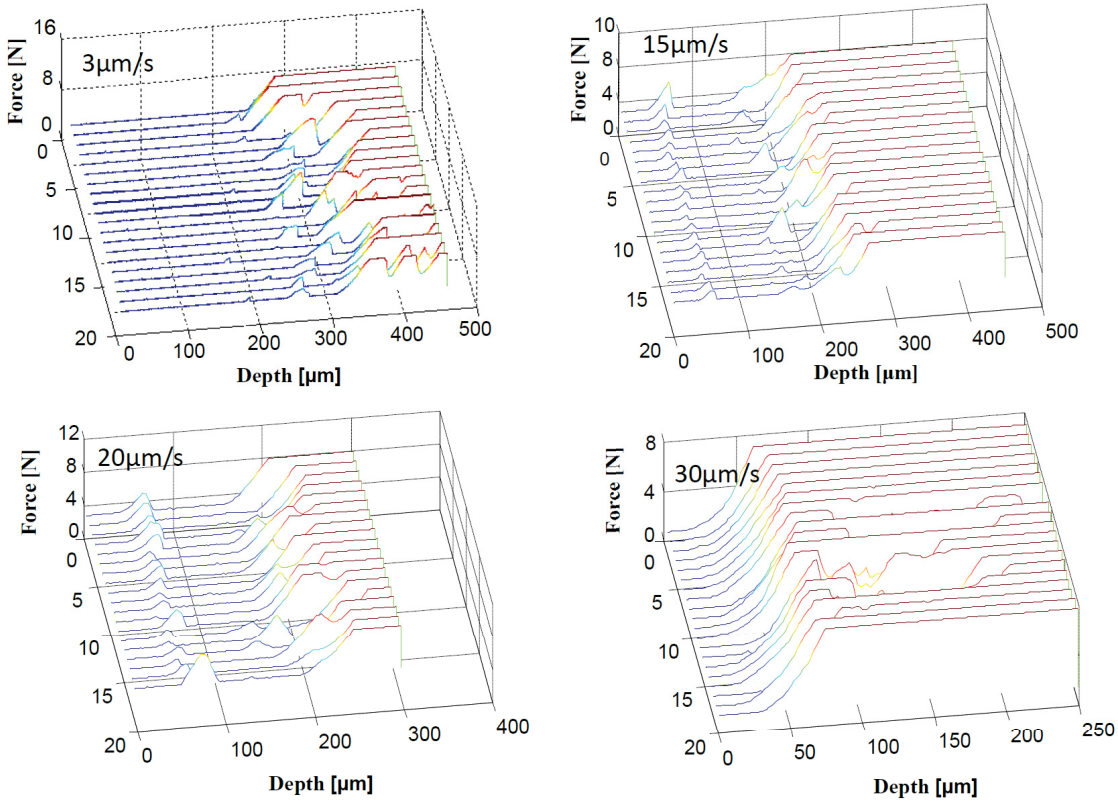

Figure 4.4: Waterfall plots showing the occurrence of forces in function of drilling depth for various tool feed-rates when using a 500 μm diameter tool-electrode and applying 33 V. The tool is positioned 50 μm above the glass surface prior to drilling and is moved at a constant feed-rate. Each waterfall plot corresponds to a certain tool feed-rate and is constructed based on 20 drilled holes. The material removal rate is negligible for feed-rates higher than 30 μm/s (force does not recover).

or flushing. Therefore, less forces must be detected when enhancing these two entities. This can be achieved by applying higher machining voltage or reducing the tool size.

4.2.2 Effect of increased machining voltage on the occurrence of drilling forces

Figure 4.4 shows plots of the forces recorded when drilling 250 μm deep holes while applying a higher voltage, 33 V, and various tool feed-rates using a 500 μm tool. For both voltages (Figures 4.4 and 4.5), when using low feed-rates (less than 1 μm/s and 5 μm/s for 30 and 33 V respectively), forces start to appear at depths above 190 μm. The forces disappear (recover) and then occur at high depths above 250 μm where they become unrecoverable. The high depth forces correspond to the third type of forces as depicted on Figure 4.3 while recoverable

forces correspond to the first two configurations (Figure 4.3) as etching progresses in this case. Intermediate tool feed-rates start from 5 to 30 μm/s for 33 V compared to 2 to 5 μm/s for low voltage. For intermediate feed-rates surface forces appear and recover rapidly where a region of zero forces follows. Forces reappear at around 120 μm for 33 V compared to 60 μm for 30 V. Hence, for intermediate tool feed-rates, the width of the middle region is wider for higher voltage indicating more efficient material removal. Similar to the case of low voltage, for increased tool feed-rates the width of the middle region shrinks until high unrecoverable forces occur at the surface. In case of 33 V, this corresponds to a feed-rate of 30 μm/s which is 10 times higher than that at lower voltage (around 5 μm/s).

These findings are in agreement with the theory that the occurrence of forces depends on how well the heat is transferred to the work-piece. Higher local temperature resulting from higher machining voltage or lower tool feed-rate enhances material removal (less tool-glass surface contact).

4.2.3 Effect of reduced tool size on the occurrence of drilling forces

To further enhance local heating and flushing, holes are drilled using a smaller tool (reduced diameter). In this case, less forces must occur for a certain machining depth. This is what figure 4.5 shows where for a 250 μm diameter tool, higher feed-rates could be used before forces become unrecoverable (correspond to negligible machining rate) compared to drilling with a larger tool. Upon machining with 30 V, no surface forces are detected for tool feed-rates below 50 μm/s. Forces in this case appear for depths between 70 and 190 μm, depending on the tool feed-rate. Intermediate feed-rates correspond to the ones between 50 and 70 μm/s where surface forces occur and forces reappear 50 μm later. As in the case of the large tool, the width of the middle region decreases for higher tool feed-rates. For the 250 μm diameter tool, unrecoverable forces occur on the surface for feed-rates above 70 μm/s compared to 5 μm/s for 500 μm diameter tool for the same applied voltage.

It can be noticed that the behaviour of the forces is similar to that resulting from using a larger tool-electrode, with the difference that for smaller tools higher tool feed-rates can be used before the forces become unrecoverable. This further confirms the theory regarding the influence of combined local temperature and flushing on the machining progress.

4.2.4 Force regions in the normalized tool feed-rate versus hole depth plane

Based on the recorded force signal, a plot depicting the force occurrence in function of the hole-depth Z and the tool feed-rate f for each voltage and tool size, is constructed as shown

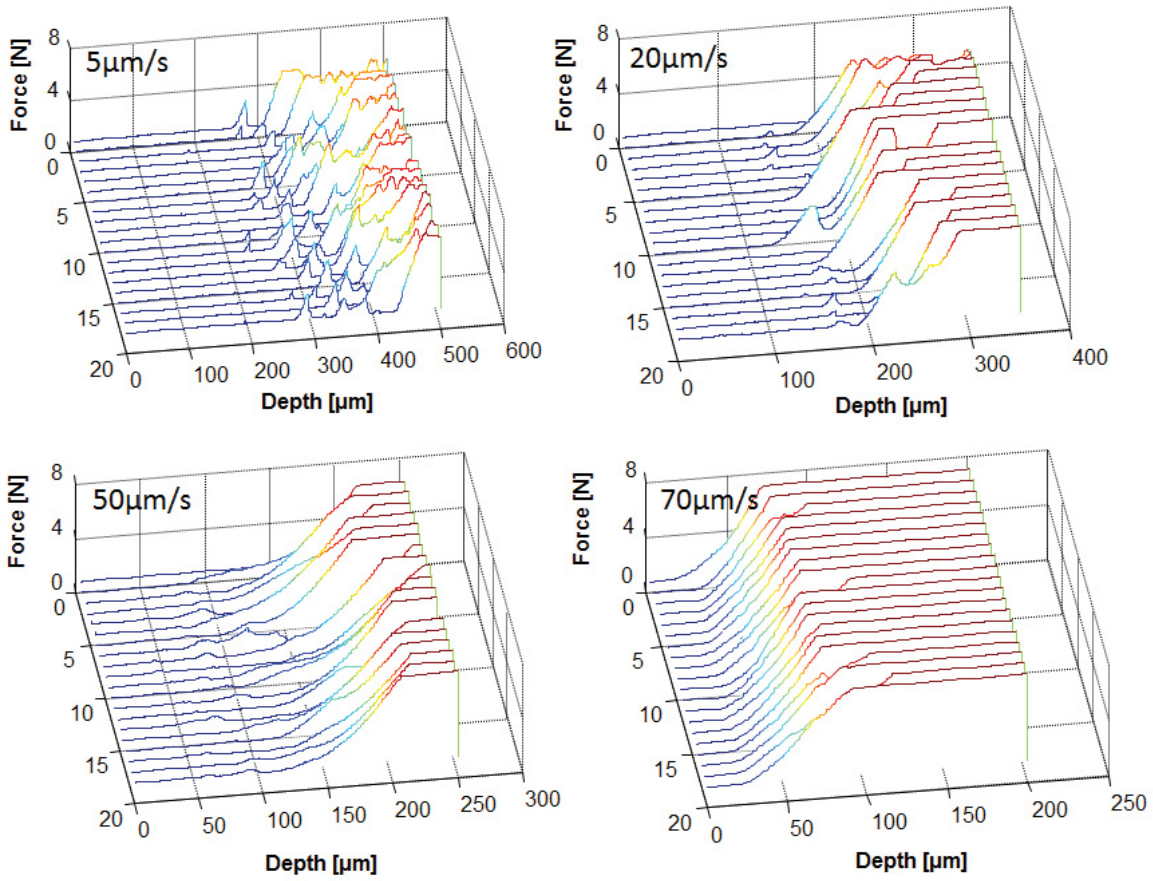

Figure 4.5: Waterfall plots showing the occurrence of forces in function of drilling depth for various tool feed-rates when using a 250 μm diameter tool and applying 30 V. The tool is positioned 50 μm above the glass surface prior to drilling and is moved at a constant feed-rate. Each waterfall plot represents recorded data based on 20 machined holes and corresponds to a certain tool feed-rate. The material removal rate is negligible for feed-rates higher than 70 μm/s (force does not recover).

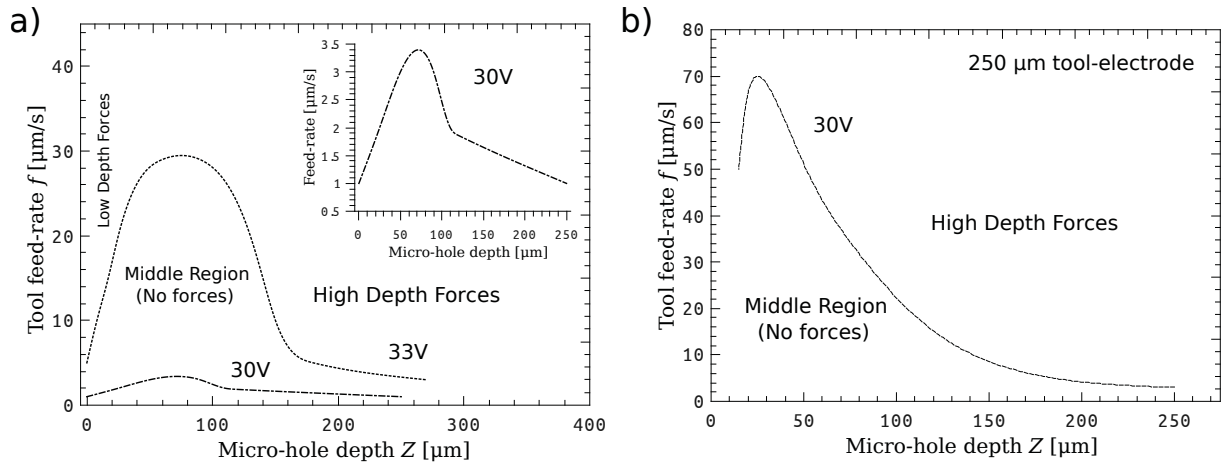

Figure 4.6: Phase plots depicting force regions in the tool feed-rate f vs. hole depth Z plane for different tool size and machining voltages. Reprinted from (AbouZiki and Wüthrich, 2013) with permission from Elsevier.

in Figure 4.6.

The schematic shows that for the large tool, the depth at which the middle region starts (during which zero forces occur) grows linearly with increased tool feed-rate. This depth z_i must be related to the time t_o needed to heat the glass surface and the tool feed-rate f used according to the following equation:

$$z_i = f t_o \tag{4.4}$$

Moreover, the width of the middle region decreases for higher tool feed-rate where high depth forces occur at a reduced depth. The schematic also shows that the maximum tool feed-rate that can be used before the surface forces become unrecoverable is shifted to a higher value when either increasing the voltage or reducing the tool size.

To further justify the theories presented in section 4.1, Equations (4.1) and (4.4) are used to present the plots in Figure 4.6 in a dimensionless form. Both the maximum allowable tool feed-rate and the machining depth that can be achieved before entering into the high force region (hydrodynamic regime) have to be influenced by the heat transferred to the machining zone. The last is determined by the time needed to heat up the glass surface. Therefore, the dimensionless plot is obtained by normalizing the tool feed-rate and the hole depth. The tool feed-rate f is normalized, based on Equation (4.4), by the ratio of the tool radius r to the time t_o needed to heat the surface. The depth Z is normalized based on the tool radius r that influences the depth at which flushing is limited (hydrodynamic regime). As shown in Figure 4.7, all the three curves are superposed on one dimensionless curve.

This dimensionless plot must be also applicable to gravity-feed drilling. During gravity-

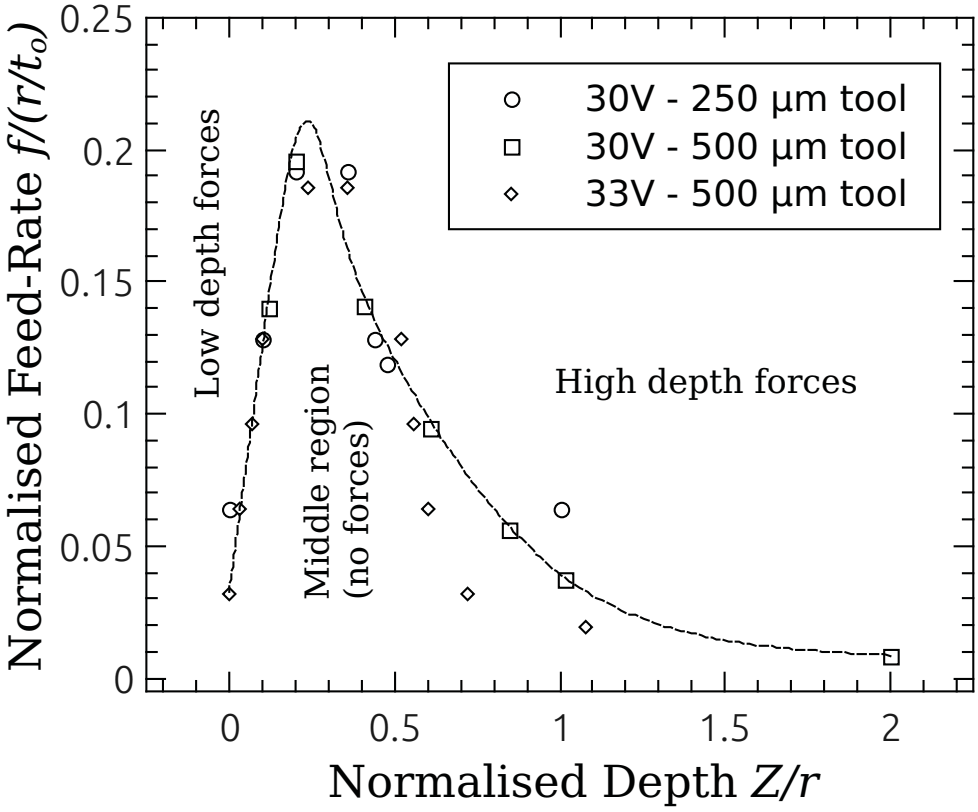

Figure 4.7: Dimensionless plot for the tool feed-rate f vs. hole depth Z depicting the force regions during SACE drilling. Normalization is done according to the time needed to heat the surface t_o and the tool radius r. Reprinted from (AbouZiki and Wüthrich, 2013) with permission from Elsevier.

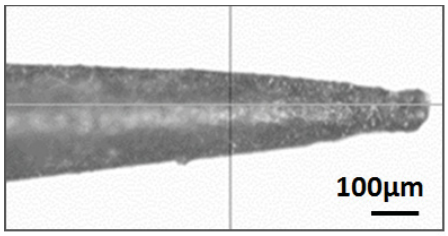

Figure 4.8: Needle-shaped tool used for 2 D machining. This tool is chosen for the purpose of enhancing local flushing. Reprinted from (AbouZiki et al., 2012) with permission from Elsevier.

feed drilling, material removal rate is high up to a depth of 70 μm, when using a 400 μm tool, after which drilling progresses slowly (Jalali et al., 2009). Converting these values to dimensionless form, the normalized depth is calculated to be 0.35 (70 μm divided by the tool radius). On Figure 4.7, the maximum normalized depth at which drilling enters into the high force region is around 0.28 which is slightly different than that calculated for gravity-feed. This is probably due to the fact that for gravity-feed the tool is always in contact with the glass surface resulting in different surface heating. Therefore, Figure 4.7 is an efficient representation of the SACE machining behaviour for all drilling modes.

4.3 A closer look into the effect of local heating during 2D machining

For 2D machining, local flushing is less problematic compared to the case of micro-hole drilling as the local flow inside a channel is less constrained. Therefore, the influence of local heating on the machining performance is investigated during 2D machining.

To ensure that local flushing is not limited, channels are machined using a pointed tool (needle-shaped as shown in Figure 4.8). During machining the tool is moved parallel to the glass surface and at a fixed distance Δz away from it. Since in the micron-range the glass slide can never be flat, the Z-position of the glass surface is detected using the profile-meter mode of the machining head at several points on the XY trajectory path to be followed by the tool. This allows obtaining the XYZ trajectory path of the tool.

Based on the theory that increased local temperature accelerates machining, higher tool travel-speed, larger Δz between the tool and the glass surface (prior to starting machining) and lower machining voltage must reduce the channel depth since for these conditions less heat is transferred to the surface.

Figure 4.9 shows two channels machined in 10 wt% NaOH using two tool travel-speeds, 10 and 20 μm/s respectively, (for 5 μm Δz and 30 V). As expected, for low tool travel-speed the

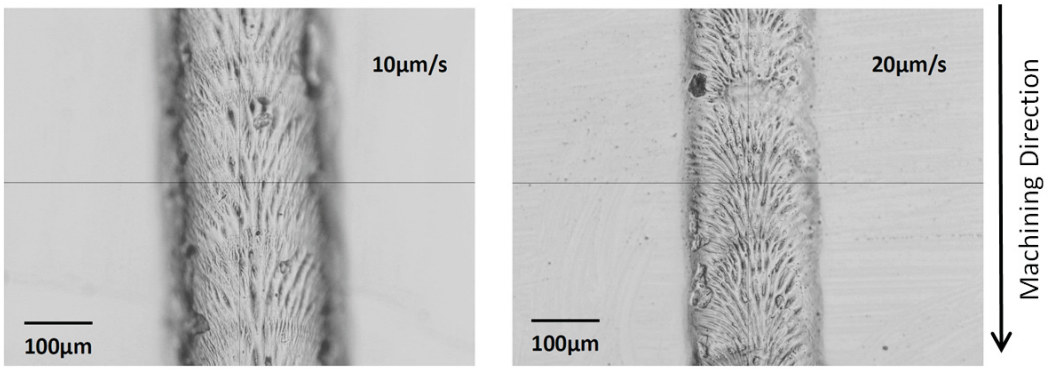

Figure 4.9: Two channels machined in 10 wt% NaOH while applying 30 V for 10 and 20 μm/s tool travel-speeds and for a 5 μm Δz. Reprinted from (AbouZiki et al., 2012) with permission from Elsevier.

channel is deeper (24 μm which is about twice the depth of the first channel). Figure 4.10 shows that the channel mean depth increases for higher electrolyte concentration. For example, for 5 μm Δz a channel depth of 13, 18, 30 and 40 μm results for 10, 20, 30 and 40 wt%. This can be attributed to the higher heat transferred to the machining zone knowing that a higher electrolyte concentration implies increased thermal conductivity (around 0.627 W/(m·K) for 10 wt% NaOH and reaches around 0.651 W/(m·K) for 40 wt% NaOH) (OxyChem, 2009). Further, for each electrolyte concentration, a higher Δz causes a decrease in the channel's depth by almost the same Δz value. These results are as expected and agree well with the theory regarding the influence of local temperature on the machining progress.

For all tool-surface gaps Δz used, tori-like structures appear on the surface. The edge of a torus is measured to be few microns higher than its center and its inner radius is equal to the tool tip diameter. Therefore, these tori-like patterns are explained to be the result of etching beneath the tool tip. For high tool travel-speed and low voltage, the temperature is high enough beneath the tool tip to allow etching while it is low on the tool's surrounding. This causes etching to be faster beneath the tool tip where a hole is created beneath it. The tool tip is trapped in this hole and it bends while its upper part continues moving in the XY plane. After a certain time, the tool jumps into another position on the surface. This process is repeated along the channel's surface resulting in the observed tori. This *stick and jump* effect is represented in Figure 4.11. The distance Δx between two tori centers can be approximated based on the schematic in terms of the height of the torus edge Δy and the tool length L as:

$$\Delta x = \sqrt{2L\Delta y} \tag{4.5}$$

where Δx is independent on the tool feed-rate which indicates that the tori-like structures

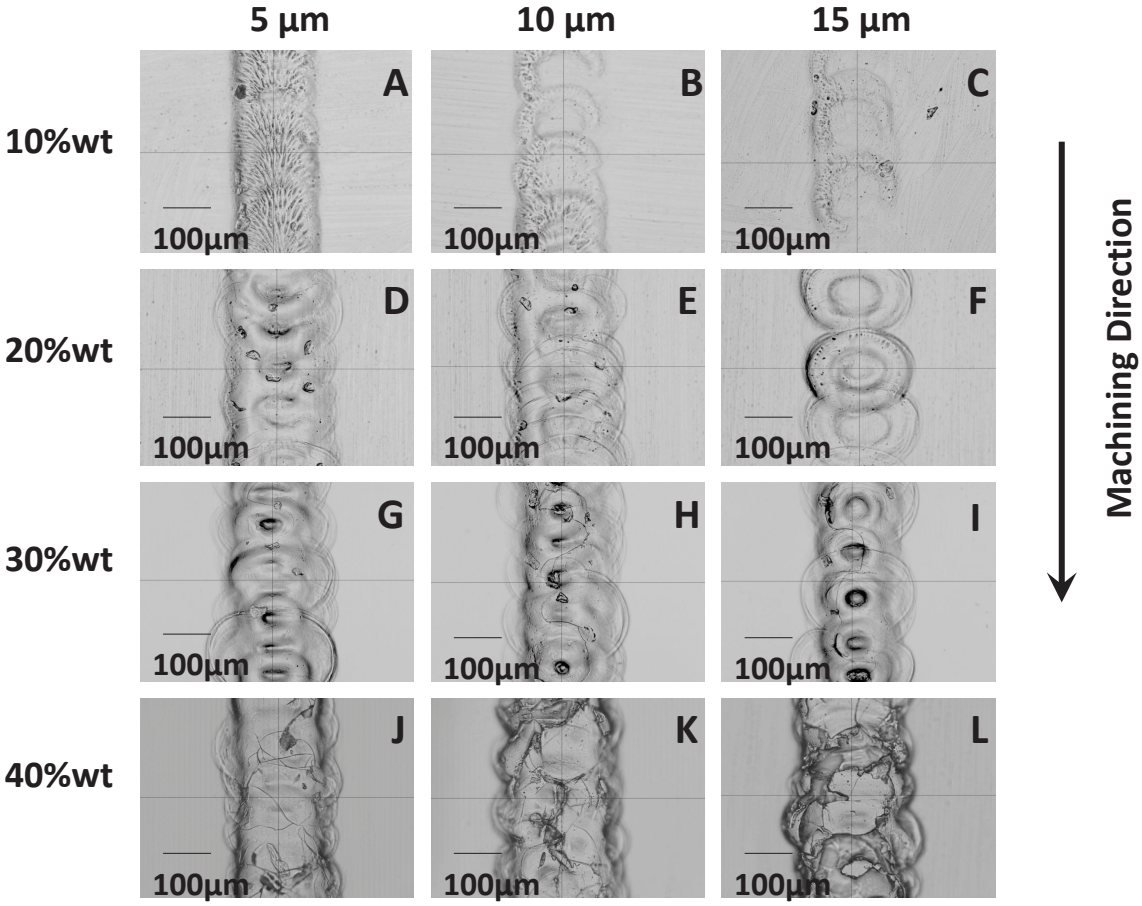

Figure 4.10: Channels machined using different electrolyte concentration (10, 20, 30 and 40 wt% NaOH) while varying Δz (5, 10 and 15 μm) for a machining voltage of 30 V and 10 and 20 μm/s tool-travel speeds. Reprinted from (AbouZiki et al., 2012) with permission from Elsevier.

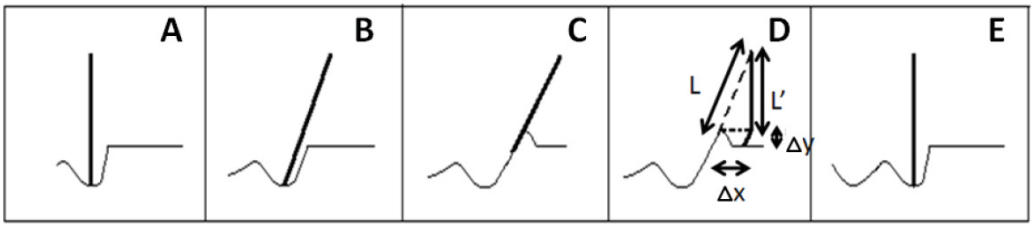

Figure 4.11: Schematic of the *stick and jump* effect in 2 D machining. Δx is the distance between the centers of two consecutive tori, Δy is the height of the torus edge, L is the tool length, and L' is the length of the tool bent tip. Reprinted from (AbouZiki et al., 2012) with permission from Elsevier.

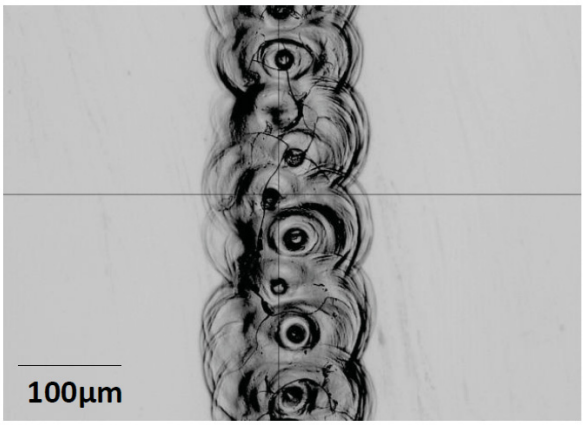

Figure 4.12: Misalignment of the tori-like structures formed on the channel surface due to the *stick and jump* effect. Reprinted from (AbouZiki et al., 2012) with permission from Elsevier.

are formed by tool mechanical contact with the glass surface (tool trapping). Further, if this is indeed the case then the tori-like structures have to be misaligned. This is indeed the case as shown in Figure 4.12 where the tori structures are separated by the same distance Δz but they are located at different X-positions on the channel surface. In this case Δx is around 150 μm which matches with Equation (4.5) for L of around 1 cm and Δy of few micrometers which agrees with the profile-meter measurements.

Figure 4.13 shows channels machined using two different voltages (30 and 32 V) for 10 μm/s tool travel-speed, Δz of 5 μm and a range of electrolyte concentrations (10 to 40 wt% NaOH). If the local heating is crucial to the machining process, as claimed in the previous sections, then deeper channels should be obtained for increased machining voltage. Profile-meter measurements support this theory where for all electrolyte concentrations, the channels are deeper by around 5 μm for the higher voltage.

The present results emphasize the importance of local heating on accelerating the machining process as discussed in the previous sections. Nevertheless, high local temperature may result in deteriorated surfaces. This is shown in Figure 4.14 where heat affected zones and cracks are formed on the surface when using 40 wt% NaOH, 28 V and 5 μm/s tool travel-speed.

It is also found that the surface roughness is affected by the electrolyte concentration. Using a stylus profile-meter (XP-200 profilometer), the channel surface roughness is found to decrease when the electrolyte is more concentrated. The average roughness is estimated to be 2.3 μm, 1.5 μm, 0.8 μm, and 0.5 μm for 10, 20, 30, and 40 wt% NaOH respectively based on the ten-point mean roughness method.

With respect to the surface texture, the reasons behind its variation from feathery-like

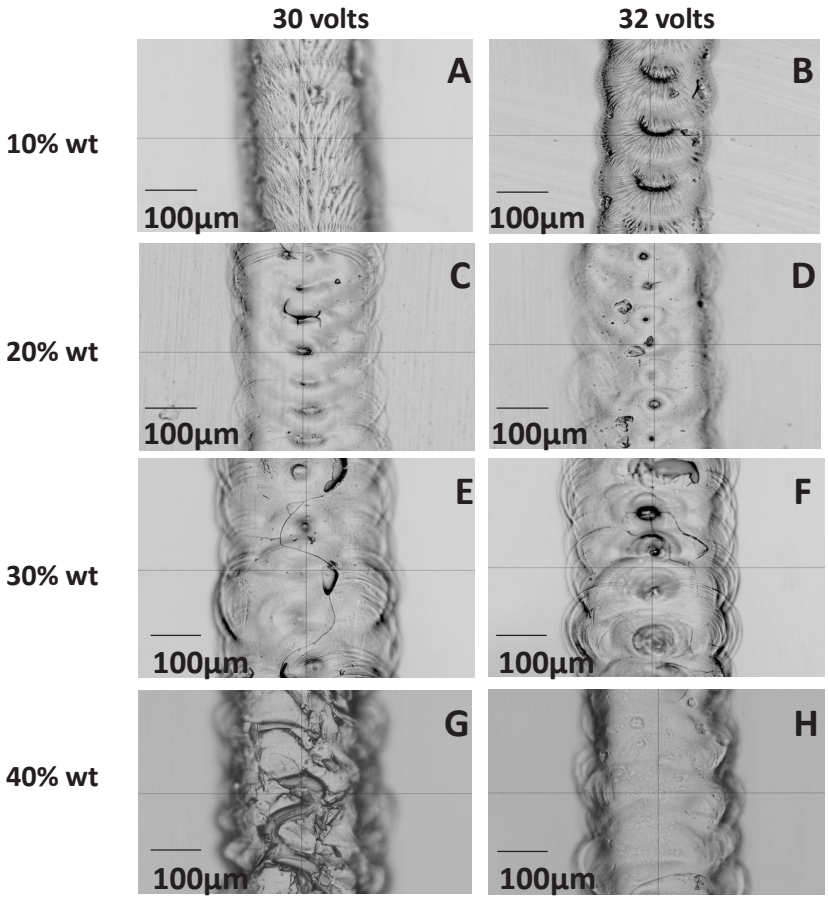

Figure 4.13: Channels machined in different electrolyte solutions (10, 20, 30 and 40 wt% NaOH) while applying 30 and 32 V for 10 μm/s tool travel-speed and for a Δz of 5 μm. Reprinted from (AbouZiki et al., 2012) with permission from Elsevier.

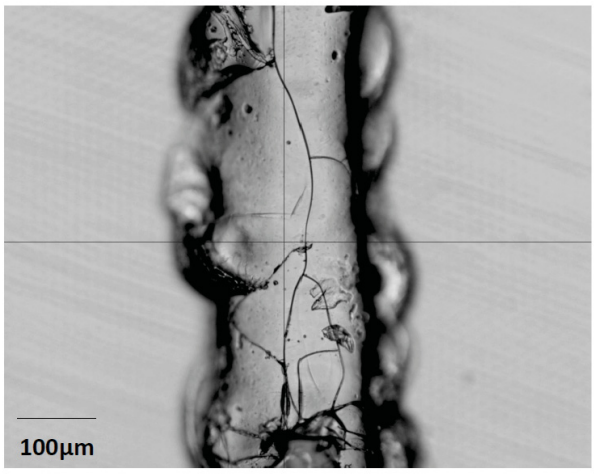

Figure 4.14: Cracks formed on the surface of a channel machined in 40 wt% NaOH solution while applying 28 V and for 5 μm/s tool travel-speed. Reprinted from (AbouZiki et al., 2012) with permission from Elsevier.

to smooth, depending on the machining conditions, are explored in Chapter 6.

4.4 Enhancing local heat transfer by forced tool-surface contact

The previous results showed that for reduced local temperature, tori-like structures are formed on the channel surface while a more homogeneous surface results for a higher local temperature. The effect of enhanced heat transfer to the machining zone on the resulting machined hole bottom surface is investigated. Holes, 100 μm deep, are drilled in 30 wt% NaOH solution by constant-velocity-feed drilling, where the tool is moved at a constant feed-rate of 10 μm/s and 33 V is applied. Whenever the pre-set force threshold (0.1 N) is exceeded, the tool motion is stopped until the force disappears and then the motion is restored. To ensure that the heat is efficiently transferred to the glass surface just before drilling is terminated, the tool is pressed against the glass surface at a constant force, called *Pressing-Force* in this text, while the voltage (33 V) is on during a certain time, denoted as *Trapping Time*. The voltage is switched off while the tool is kept at the same position during 10 s to allow cooling it down. The cooling time of 10 s is chosen such that enough time is allowed for the tool to retract to its original length, estimated in the same way as in Figure 3.17. Note that the designed force sensor allows measuring forces in both upward and downward directions. While a positive force indicates that the tool is pushed upwards, a negative force implies that the tool is being pulled in the downward direction towards the glass surface.

For any of the Trapping Times applied, it is realised upon analysis of the force signal that as soon as the voltage is switched off, the force decays. This is due to the retraction of the tool where it becomes shorter and hence moves away from the glass surface. This motion causes a reduction in the force amplitude. The force is removed when it reaches the zero-level. Unexpectedly, the force continues decaying beyond zero where it stays negative during a short time after which it quickly jumps back to zero. This is depicted in the inset of Figure 4.15 which shows that the decay in the force signal, denoted as *Delta-Force* in this text, is exponential and hence corresponds to the tool thermal retraction as both follow the same behaviour. Knowing the force sensor stiffness (0.047 N/μm) and Delta-Force, the change in the tool length can be calculated knowing the temperature at which the tool starts retracting, that is calculated in the same way as in Figure 3.18. Therefore, a fixed Delta-Force corresponds to a certain tool cooling temperature. The jumping of the force from a negative value and back to a zero level is explained by the fact that the tool got attached

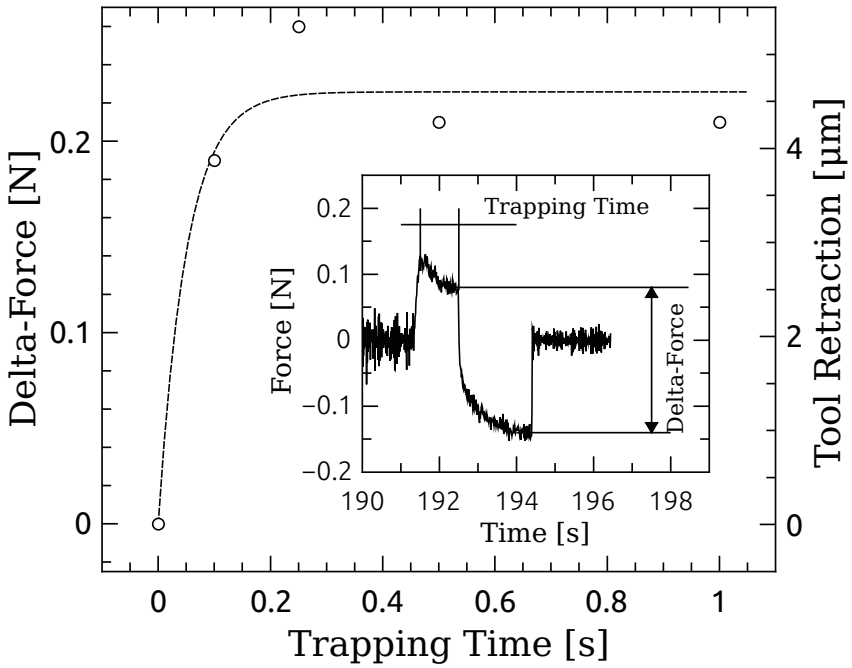

Figure 4.15: The change in Delta-Force in function of the force threshold (Pressing-Force). The figure inset is a representative example of the recorded force signal in function of time (for 100 μm hole depth, using 30 wt% NaOH solution, 10 μm/s tool feed-rate and 33 V) and it depicts the Trapping Time and the Delta-Force. Delta-Force represents the decrease in the force signal after switching off the voltage before the tool is released.

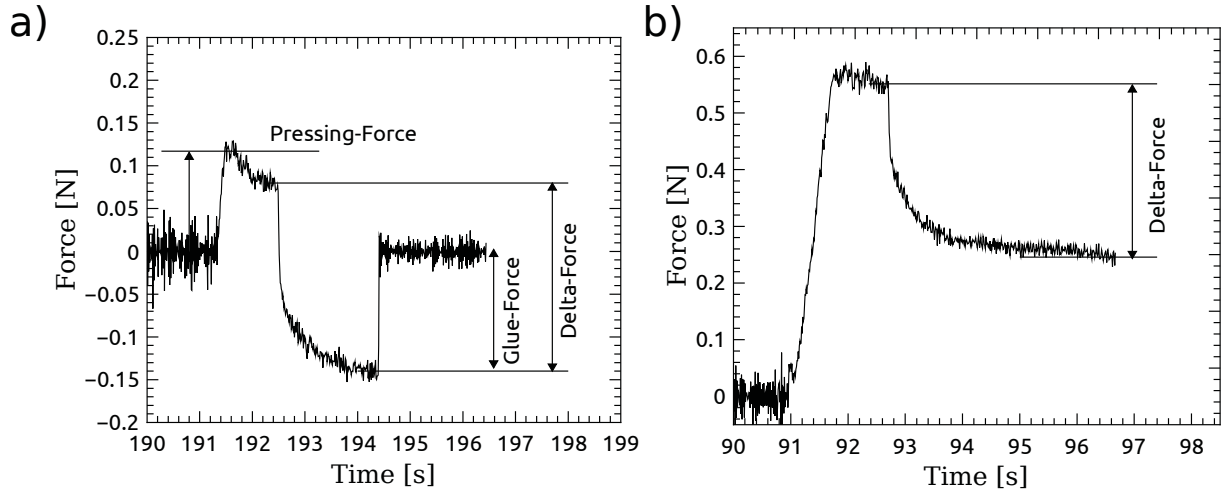

Figure 4.16: Plots of the recorded force signal vs. machining time depicting the two forms that the force signal can take when the tool is bonded to the glass surface.

to the glass surface during a short time, while the force is negative. The force goes back to the zero level when the tool is detached from the glass surface where this change in the force amplitude is denoted as the *Glue-Force* in this work. Figure 4.15 shows that Delta-Force is constant for all applied Trapping Times implying that the tool retracts by the same amount. Due to the limitations of the current set-up the minimal Trapping Time that could be applied is 0.1 s. This indicates that a small Trapping Time is sufficient to allow tool-glass bonding where the surface is heated quickly as soon as the tool is pressed against it.

The drop in the force signal once the tool retracts can take one of the two forms depicted in Figure 4.16. In the first case, the Pressing-Force is smaller than Delta-Force where the tool retraction causes a drop in the force to a negative value after which the tool detaches from the glass surface. In the second case, the Pressing-Force is larger than Delta-Force where the force drops into a positive value upon tool retraction that reaches a maximal value. Hence, the tool never detaches from the surface in this case.

The effect of the Pressing-Force on the Glue-Force amplitude is investigated. Figure 4.17a shows that the Glue-Force stays constant independently of the Pressing-Force. If the tool is glued to the glass at a specific temperature by solidification of material between the two surfaces, for example electrolyte molten salt, then the tool must be released at a fixed temperature decay (at which the solidified material is dissolved) regardless of the Pressing-Force magnitude. Therefore, Delta-Force must drop to a value corresponding to the same temperature. Figure 4.17b shows that Delta-Force increases for a higher Pressing-Force where different tool retraction is calculated, indicating that the tool is released at different temperatures. The constant Delta-Force value reached after a Pressing-Force of around 0.25 N corresponds to a maximal tool thermal retraction that is attainable for the applied machining

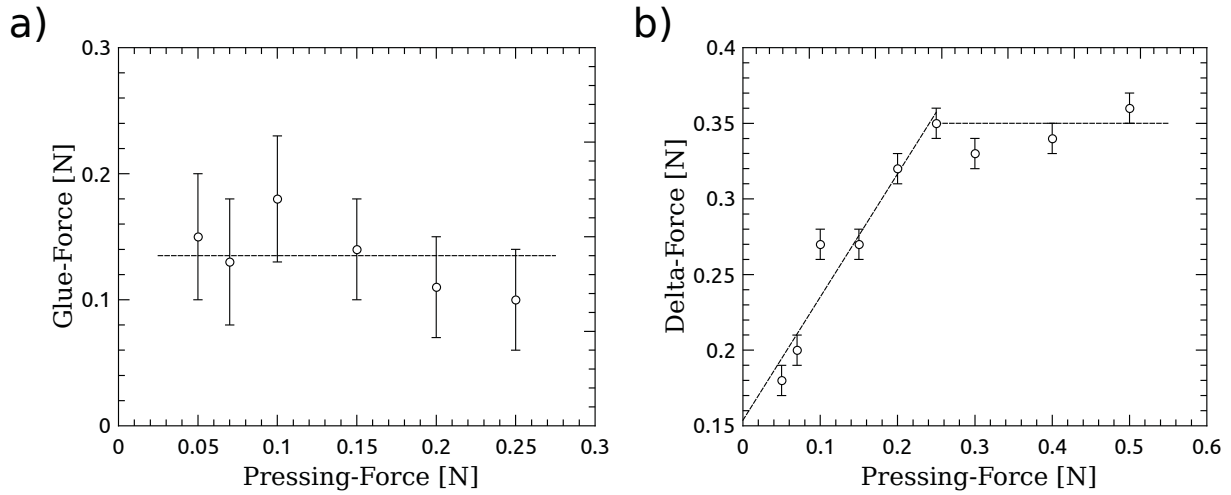

Figure 4.17: a) The Glue-Force and b) the Delta-Force in function of the Pressing-Force (presses tool against glass surface).

conditions beyond which the Glue-Force is not measurable. Note that for the maximal Delta-Force (0.35 N), the tool expansion is about 7.5 μm knowing that the force sensor stiffness is 0.047 N/μm. This value matches with the tool expansion measured in Section 3.3.2 for an applied voltage of 33 V (see Figure 3.18a). This shows that the maximal tool expansion is indeed reached at 0.35 N Delta-Force, ensuring the correctness of the interpreted data. These results show that the tool-glass bond is not broken due to temperature decay, for example due to flushing away the solidified NaOH beneath the tool. Rather, as the Glue-Force is constant, the bond is broken when the force pulling the tool away from the glass exceeds the bond strength. When extrapolating the curve to zero Pressing-Force the resulting Glue-Force is around 0.15 N which is the same as that obtained in Figure 4.17 for the different Pressing-Force. This suggests that the bond is chemical probably similar to field-assisted bonding. The last occurs between metal and glass during a short time and at temperatures lower than the glass softening point which is around 700 ^{o}C Wallis and Pomerantz (1969). During SACE machining, the ions from the glass bulk might migrate to its surface due to the high electrical field in the tool vicinity. This may result in a bond between the tool (metal) and the glass.

The hole bottom surfaces are shown in Figure 4.18 for different Pressing-Force levels. For small Pressing-Force, the decay in the force must have the form depicted in Figure 4.16a. In this case the machined surface is deformed due to tool detachment before the glass cools down (right after the machining is stopped). For increased Pressing-Force, the tool must stay in contact with the glass surface even after the tool retracts as in Figure 4.16b. In this case the tool is pressed to the glass surface during 10 s after switching off the voltage allowing the glass to cool down slowly before the tool is detached. Therefore, a smooth hole

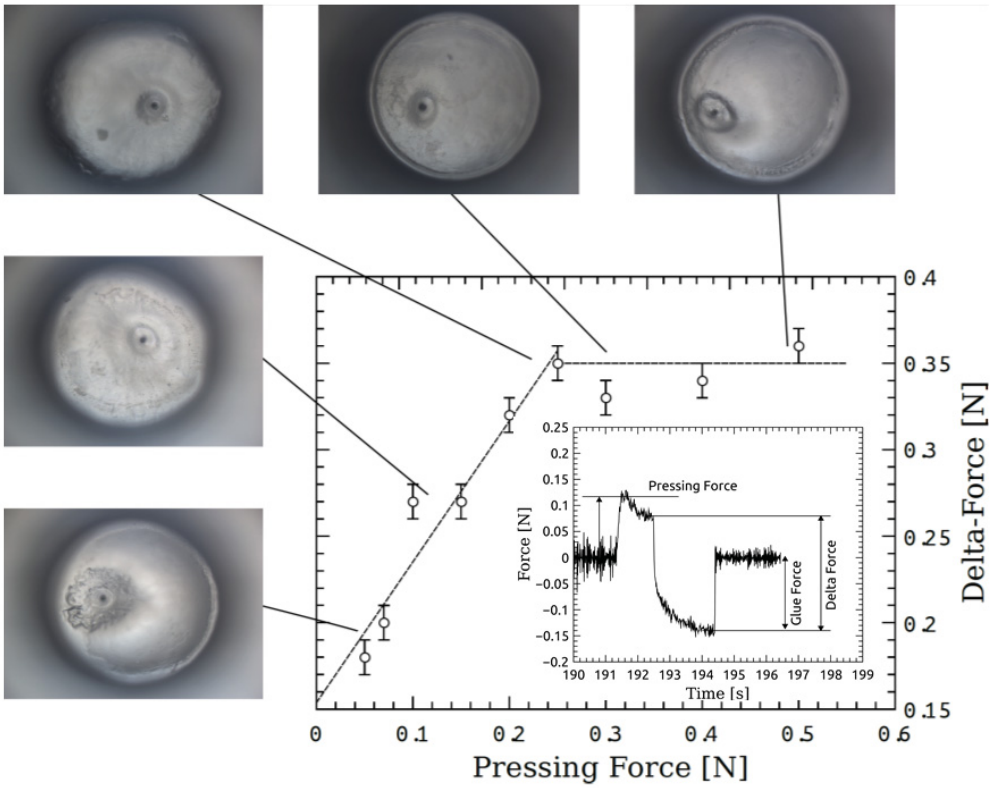

Figure 4.18: A plot of Delta-Force in function of the Pressing-Force. The figure inset is a representative example of the recorded force signal in function of time and it depicts the Pressing-Force, the Glue-Force and the Delta-Force. The Delta-Force represents the decrease in the force signal after switching off the voltage before the tool is released. Pressing-Force is the force threshold and Glue-Force is the negative force implying tool-glass surface bonding. The figure also shows the typical hole bottom surfaces for each selected Pressing-Force. For high Pressing-Force (above 0.25 N) an imprint of the tool bottom surface could be seen on the machined glass surface.

bottom surface results where the tool bottom surface is imprinted on the glass. This explains the non-homogeneities appearing on the surface for low Pressing-Force and the smooth and circular surface for forces higher than 0.25 N as shown in Figure 4.18.

4.5 Addressing the issue of local heating and flushing

Knowing that local heating for low machining depth and flushing for high depth are limited, an algorithm is added during constant-velocity-feed drilling to investigate if this issue can be addressed. The algorithm is to take an action whenever a pre-set force threshold is exceeded such that drilling will proceed with almost zero forces. The action is either waiting for a certain duration or moving away from the surface by a small distance or doing both while the voltage is switched on. Adding a waiting time to heat the machining zone at low depths, whenever the force threshold is exceeded, must enhance machining. In this case, the force have to be reduced to around zero where machining will proceed at higher rate. Moving away from the surface when the force threshold is exceeded at high depths, is expected to enhance flushing.

The first algorithm done is to favour flushing, where the tool is moved away from the surface by 10 μm whenever a force higher than the pre-set threshold is exceeded. For these experiments two thresholds, 230 and 850 mN, are chosen. 400 μm deep holes are drilled using a cylindrical 500 μm tool while applying 33 V, for tool feed-rates ranging from 3 to 30 μm/s. For high tool feed-rates, on one side the tool is close to the machined surface which will increase the local temperature. On the other side, the chance of tool-work-piece contact becomes higher with increased feed-rate. This results in taking more actions to flush the hole which has to eventually cause heat loss. Hence, one expects that when increasing the tool feed-rate, drilling becomes faster until reaching a limit dictated by the trade-off between heating and flushing of the machining zone. This is indeed the case as Figure 4.19a shows where for tool feed-rates above 10 μm/s drilling proceeds in a similar manner, in case of the high force threshold (850 mN).

More heat loss must result for a smaller force threshold since the tool upward motion is done more frequently. Hence, the drilling time for low force threshold must be higher than that resulting from using a higher force threshold for the various applied tool feed-rates. Figure 4.19b shows this effect where drilling time is longer for the low force threshold (240 mN). For example, when considering 3 μm/s feed-rate, drilling time is reduced from 450 s (Figure 4.19b) to 240 s (Figure 4.19a) when increasing the force threshold. Hence, for the rest of the experiments 850 mN force threshold is used.

To ensure that the tool upward motion, whenever the force threshold is exceeded, is

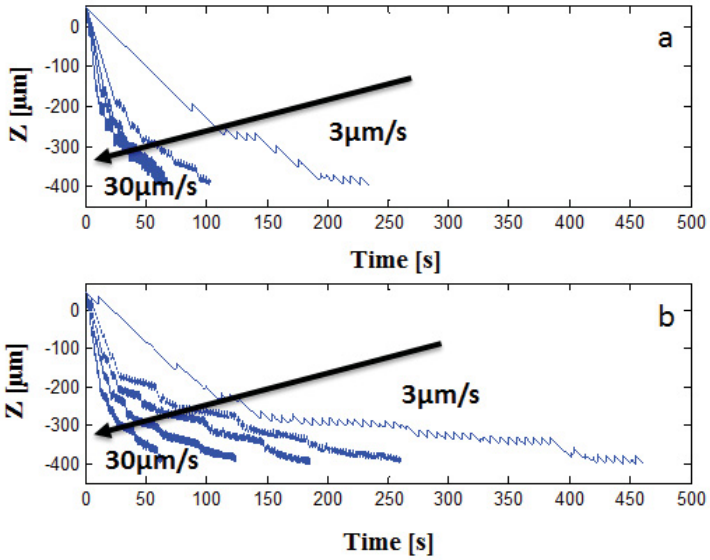

Figure 4.19: Motion of the Z-stage in function of time for holes machined using a 500 μm tool, 30 wt% NaOH and different tool feed-rates (3, 5, 10, 20 and 30 μm/s). The tool is moved away from the surface by 10 μm whenever the pre-set force threshold: a) 850 and b) 240 mN, is exceeded. Machining proceeds afterwards where the tool is moved again at a constant feed-rate towards the glass. Note that a different time-scale is used in (a) and (b). Reprinted from (AbouZiki and Wüthrich, 2013) with permission from Elsevier.

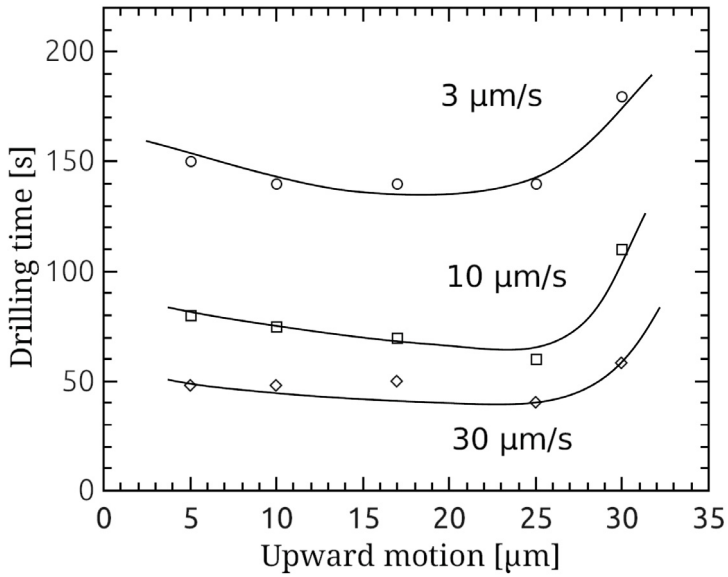

Figure 4.20: Drilling time in function of the tool upward motion for 3, 10 and 30 μm/s tool feed-rates. The minimum drilling time corresponds to 25 μm upward motion. Reprinted from (AbouZiki and Wüthrich, 2013) with permission from Elsevier.

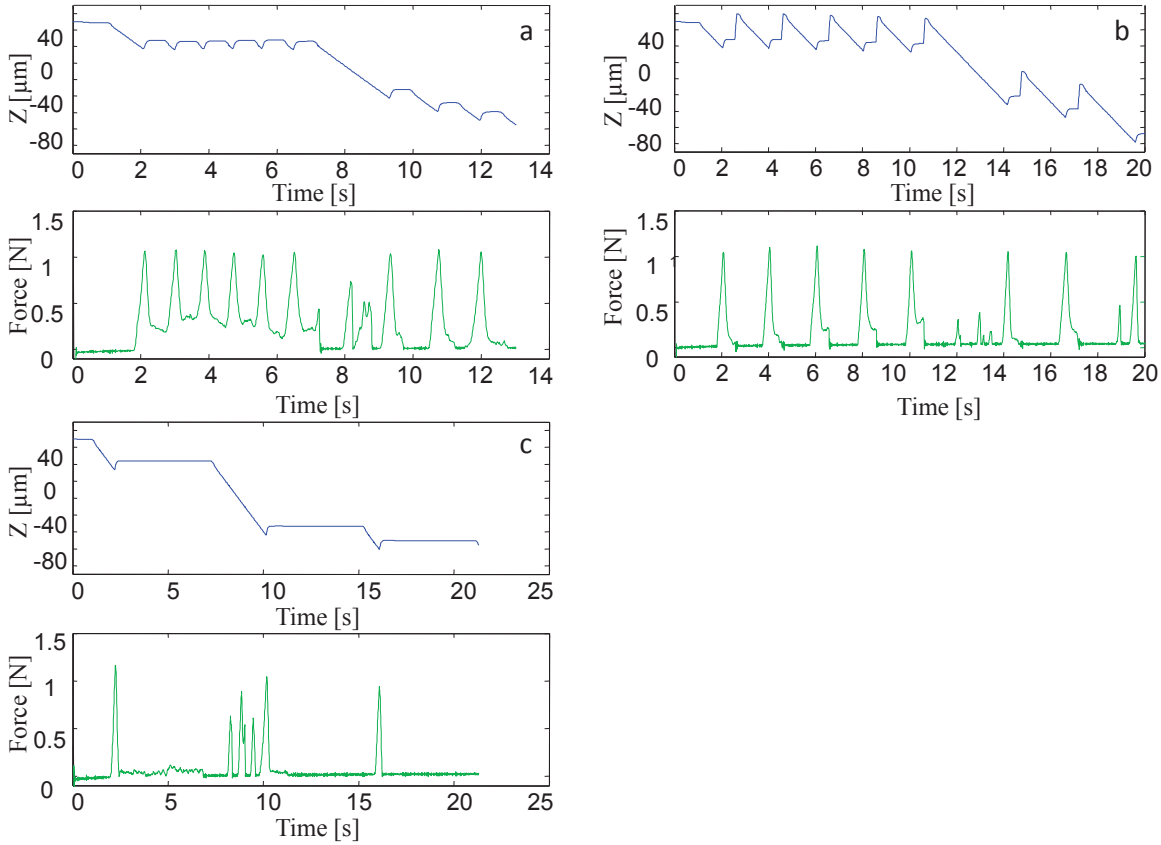

Figure 4.21: Effect of adding a waiting time and an upward motion, whenever the force threshold is exceeded, on heating and flushing. A waiting time of 0.5 s is added a) while keeping the tool at the same position (without upward motion) and b) after moving upwards by 25 μm. The waiting time is increased to 5 s in (c). Reprinted from (AbouZiki and Wüthrich, 2013) with permission from Elsevier.

sufficient to allow good flushing while maintaining the machining zone temperature, the drilling time for a range of tool upward movement is recorded. Increasing the upward motion up to a certain value must help enhance machining after which it must become counter-productive. As shown on Figure 4.20, for different tool feed-rates (3, 10 and 30 μm/s), the shortest drilling time resulted from an upward motion of 25 μm.

Based on this result, 100 μm deep holes are drilled while applying 33 V and moving the tool at the fastest possible feed-rate, which is 30 μm/s in this case as shown in Section 4.2. Whenever a force of 850 mN is exceeded, one of the following three actions is taken:

- a waiting time of 0.5 s is added (Figure 4.21a),
- a waiting time of 0.5 s is added after moving upwards by 25 μm (Figure 4.21b) and

- a waiting time of 5 s is added (Figure 4.21c).

Figure 4.21 shows that the lowest drilling time is attained for the first algorithm and is increased for the last two cases. This validates the claim that for low depth insufficient heating of the work-piece limits machining. In this case, creating a tool-glass gap whenever the force is exceeded is counter-productive. On the other side, adding a sufficient waiting time to heat the glass surface enhances machining.

For depths higher than 300 μm, adding a waiting time to heat up the surface does not reduce the drilling time. However, drilling is accelerated when an upward motion is added to the tool whenever the force threshold (850 mN) is exceeded. This shows that for high depth limited local flushing hinders the machining evolution.

4.6 Conclusion

In this chapter, drilling forces are characterized for various machining conditions. These forces are the result of mechanical contact between the tool and the work-piece due to the insufficient material removal rate. It is shown that when increasing the machining voltage or reducing the tool size drilling forces appear at higher depth due to the enhanced flushing. Further, for these cases when applying low tool feed-rates the surface forces are not present due to the reduced time needed to heat up the glass surface. Based on this knowledge, the forces are plotted in the normalized tool feed-rate versus hole depth plane. This dimensionless plot shows the depth regions at which forces occur. In fact, it allows choosing the machining parameters such that for a desired hole depth minimal contact forces are exerted on the tool during drilling.

The significance of surface heating on the machining is demonstrated in 2D machining where flushing is not limited in this case. It is shown that for reduced tool travel-speed and tool-surface gap and for higher voltage deeper channels result. For fast tool travel-speeds the stick and jump effect occurs where the tool jumps from one position to another on the surface due to insufficient local heating. Further, it is demonstrated that the machined channel depth is higher for increased electrolyte concentration (higher thermal conductivity) which further emphasizes the effect of enhanced local temperature on machining.

This chapter also shows that during machining a tool-glass bonding, noticed from the recorded force signal, can form. This effect influences the machined surface texture where a tool imprint on the machined surface could be obtained for high pressing forces. Investigation about the nature of the bond showed that it is not created by solidification of local material beneath the tool, like molten electrolyte salt, upon cooling down the machining zone. It was

found that this bond is most likely chemical as it forms at almost zero tool-surface pressing force.

The potential of improving the local heating and flushing is investigated by implementing simple algorithms that stop the tool motion or move it away from the surface when a certain force threshold is exceeded while drilling. The present findings show that the local heating and flushing are important factors during SACE machining process. Balancing these two factors is needed for better machining performance (faster machining and enhanced surface quality).

Chapter 5

The machining gap

Hope sees the invisible, feels the
intangible, and achieves the impossible.
(-Woody Allen)

In the previous chapter insufficient local heating and flushing, particularly for depths starting at the end of the middle region in Figure 4.7, were identified to be the main reasons for the existence of contact forces during machining. In this chapter, it is demonstrated for the first time in the field of SACE that the machining progress is directly linked to the formation of a gap beneath the tool while machining at these depths. For a constant tool feed-rate, tool-work piece mechanical contact and consequently machining forces are caused by a reduced gap size. The size of the gap is random since it is dependent on how good the flushing is and how well the etching progresses. In this work, the average gap formed during machining for depths at which contact forces occur is quantified for different machining conditions. It is demonstrated that the reduced gap size is caused by a reduction in local temperature and by limited flushing. The dependence between the maximal established gap and the local temperature is described by a thermal heat transfer model. The model is based on the idea that during machining the gap grows until the local glass temperature drops to the electrolyte salt melting point. The agreement between the measured and the calculated gap shows the validity of the proposed idea. All this evidence clearly shows the importance of local heating and flushing on the SACE machining progress.

5.1 Machining gap model

Chapter 4 revealed that the appearance of forces during drilling is due to mechanical contact between the tool and the glass surface. Depending on the machining conditions, different

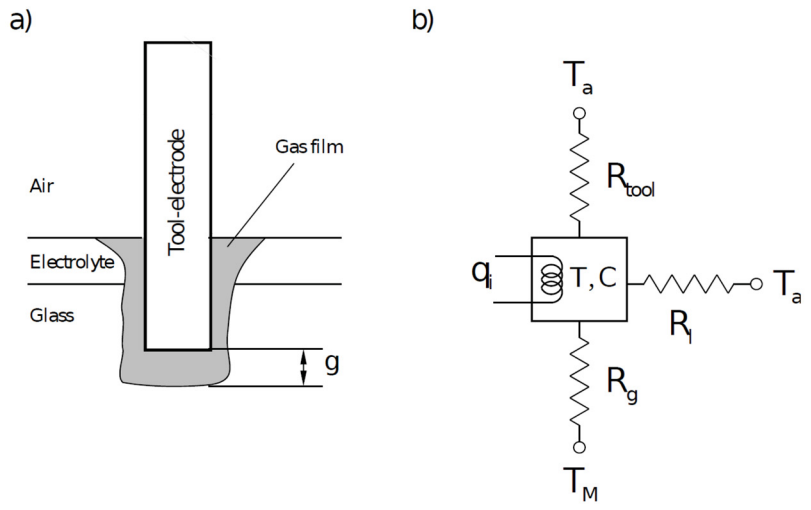

Figure 5.1: a) Schematic of the tool-work piece gap g, and b) Schematic of the thermal model that takes into account the heat dissipation inside the gap where R_l and R_{tool} are the electrolyte and tool thermal resistances, R_g is thermal resistance inside the gap, T_a is the ambient temperature, T is the tool temperature, T_M is the machining temperature, C is the tool heat capacitance, q_i is the heat source due to discharges.

depth regions where forces are exerted on the tool are identified. For certain depths, zero machining forces result. Accordingly, it is claimed that a gap is formed between the tool and the local machined glass surface during machining and it diminishes under certain circumstances causing tool-work piece mechanical contact (machining forces). This gap, illustrated in Figure 5.1a, will be referred to in this text as the *machining gap*.

Chapter 4 showed that for efficient local heating and flushing, tool-glass surface contact is minimal. Hence, it becomes reasonable to claim that the size of the machining gap is linked to how well local flushing and heating are achieved. Accordingly, the following mechanism is proposed. For high local temperature, the machining rate increases resulting in a larger machining gap. The gap growth causes increased heat transfer resistance between the tool and the work-piece which results in a drop in the local temperature in the gap. When the temperature drops below a certain critical temperature at which the material removal rate is negligible, the gap does not grow anymore. This critical temperature is still highly debated in the literature where for example (Fascio et al., 2004) predicted that it is higher than the glass softening temperature while (Jalali et al., 2009) estimated that this temperature is around 600 °C. Recall that the tool temperature is around 500 °C (Section 3.3.2). At this temperature no aqueous electrolyte is available but rather a molten salt (e.g. molten NaOH or KOH) exists. In this work, it is proposed that when the local temperature drops below the electrolyte salt melting point T_{ME} (318 °C for NaOH and 406 °C for KOH), the electrolyte solidifies and glass can no longer be etched. In this case, a maximal gap is reached. Based

on this theory, a model that describes the local heating process is constructed.

From Chapter 3, the thermal model for tool expansion considers the discharges as a heat source $q_i(t)$ attached to the tool. When a gap is present beneath the tool, the heat generated by the discharges will be dissipated through the tool itself, the electrolyte surrounding the tip and through the gap. Hence, the tool with heat capacitance C and temperature T, is connected to the electrolyte (considered to be at ambient temperature T_a), the upper part of the tool and the machining gap by three resistances R_l, R_{tool} and R_g respectively as represented in the schematic of Figure 5.1b.

By defining R to be the equivalent resistance of the two resistances R_l and R_{tool} connecting the heat source to T_a, the heat transfer equation at steady state can be written as (T_M is assumed to be equal to T_{ME}):

$$q_i = \frac{1}{R}\left(T - T_a\right) + \frac{1}{R_g}\left(T - T_{ME}\right) \tag{5.1}$$

The resistance across the machining gap depends on the thermal conductivity λ_g of the material inside it (including the molten electrolyte, gas bubbles and the machined material), on the gap size g and on the tool diameter d based on the following:

$$R_g = \frac{4g}{\lambda_g \pi d^2} \tag{5.2}$$

Previous studies showed that etching stops when the distance between the tool and the glass surface is more than $25\,\mu$m (Fascio et al., 1999; Wüthrich, 2003). Therefore, the gap is assumed to be in the same order of magnitude. For a gap less than $100\,\mu$m, R is much larger than R_g (Equation (5.2)). This allows rewriting Equation (5.1) as:

$$q_i = \frac{1}{R_g}\left(T - T_{ME}\right) \tag{5.3}$$

Further q_i can be written based on Section 3.3.2 (Equation (3.18)) as:

$$q_i = \left(T - T_a\right)\pi d \lambda_l \tag{5.4}$$

with λ_l the electrolyte thermal conductivity. By substituting Equations (5.2) and (5.4) in Equation (5.3) the machining gap g can be represented as:

$$g = \frac{\lambda_g}{\lambda_l} \cdot \frac{d}{4}\left(1 - \frac{T_{ME} - T_a}{T - T_a}\right) \tag{5.5}$$

Equation (5.5) can be represented in dimensionless form by eliminating the gap depen-

dence on the tool diameter as follows:

$$\frac{g}{d} = \frac{1}{4} \cdot \frac{\lambda_g}{\lambda_l} \left(1 - \frac{T_{ME} - T_a}{T - T_a}\right) \tag{5.6}$$

Hence, in dimensionless form the normalized gap is dependent on the thermal conductivity of the electrolyte λ_l and that of the material inside it λ_g, the electrolyte salt melting point T_{ME}, the tool temperature T and the ambient temperature T_a.

5.2 Measurement methodology

As during drilling a gap is continuously created between the tool and the glass machined surface, the size of this gap is random and dependent on how well the etching progresses. To identify the mean value and standard deviation of the machining gap, a methodology that allows gap measurement based on the force signal is developed. The measured gap is corrected for tool thermal expansion measured in Section 3.3.

The gap measurement is done in two steps:

1. The hole is drilled at a constant feed-rate up to the desired depth. Prior to machining, the tool is positioned 50 μm above the glass work-piece (detected using the profilemeter function of the machine head). The machining head is used in its force sensor mode where for machining forces higher than 0.3 N the motion is stopped during a certain time to remove the force (to avoid tool and surface deformation).

2. A waiting time of 10 s, denoted by *cooling time* in this text, is added after drilling the hole (while the voltage is off) to cool down the tool and the glass surface before measuring the gap. The gap is measured for the cases where drilling ends while no contact forces are measured ensuring that a gap is indeed formed.

The first investigated gap measurement method requires moving the tool downwards, after drilling the hole, towards the machined surface by a distance g ranging from 10 to 35 μm (tool feed-rate set to 25 μm/s). For each drilled hole the tool is moved downwards by a specific g where the frequency of tool-glass surface contact, witnessed by force detection, is recorded (50 measurements done for each g). The frequency of tool-glass surface contact for five chosen g values is plotted and fitted to the cumulative distribution function of the normal distribution. The g for which 50% of the measurements resulted in tool-glass surface contact is the average gap. For each set of machining conditions, 300 holes are required (50 holes for each g). Figure 5.2a shows the distribution of the frequency of measurements indicating tool-glass surface contact versus g for 100 μm deep holes drilled

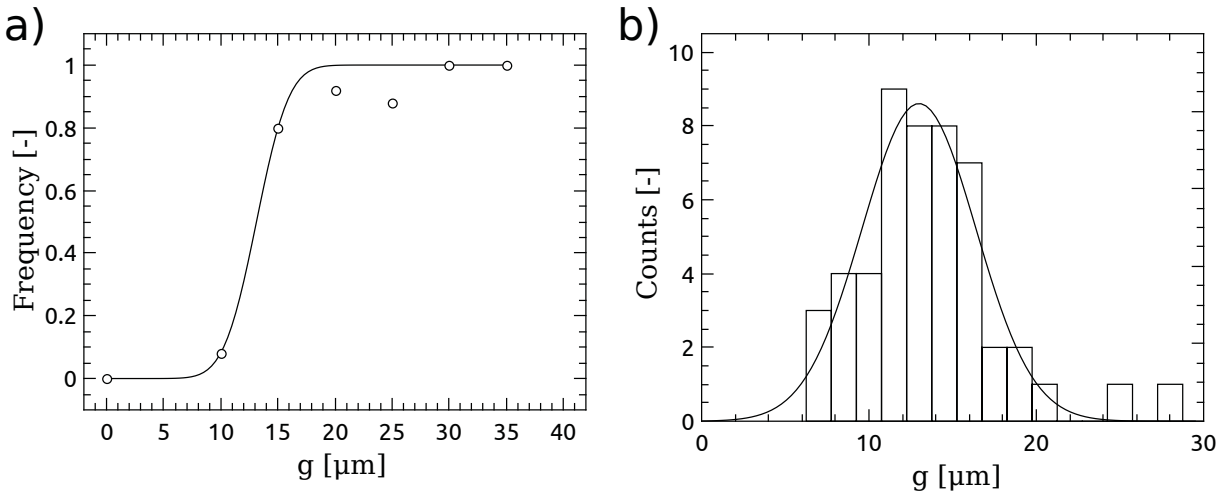

Figure 5.2: The average gap value obtained using two measurement methods. a) In the first method, the gap measurements follow the cumulative distribution function of the normal distribution. g for which the frequency of tool-surface contact is 50% corresponds to a gap of 13.1 ($\pm$0.2) μm. b) For the second method, the measured gap is fitted using the Gaussian distribution where an average gap of 12.9 ($\pm$0.3) μm resulted as well.

in 30 wt% NaOH solution using a 250 μm tool-electrode while applying 33 V. For this set of machining conditions the gap is around 13.1 ($\pm$0.2) μm, before being corrected for tool thermal expansion.

The second investigated gap measurement method is based on moving the tool downwards, after drilling the hole, a large enough distance (higher than 20 μm) to ensure that it contacts the surface. The distance that the tool moves downwards until a force is detected is the gap. For these measurements, a waiting time is added after drilling to cool down the glass and tool surfaces before measuring the gap. This time is denoted as *cooling time* in this text. Figure 5.3 shows an example of the measured gap based on two signals depicting the Z-motion and the machining force in function of time. A cooling time of 10 s (Figure 5.3a) is added after drilling the hole (before measuring the gap). Figure 5.3b, shows that a force is detected after 27.4 s which corresponds to a tool downward motion of 11 μm (Figure 5.3a). Therefore, the gap is 11 μm in this case. Fifty measurements (based on 50 holes) are done for each set of machining conditions. The collected data is plotted on a histogram and is fitted using the Gaussian distribution to obtain the average value of the gap. Figure 5.2b shows the resulting gap measurements for the same machining conditions as those applied for the first measurement method. The gap is in average, before being corrected for tool thermal expansion, around 12.9 ($\pm$0.3) μm (error calculated based on 95% confidence interval of the least square regression) which is similar to the value obtained using the first method. Since the second gap measurement method requires less data for a certain set of machining

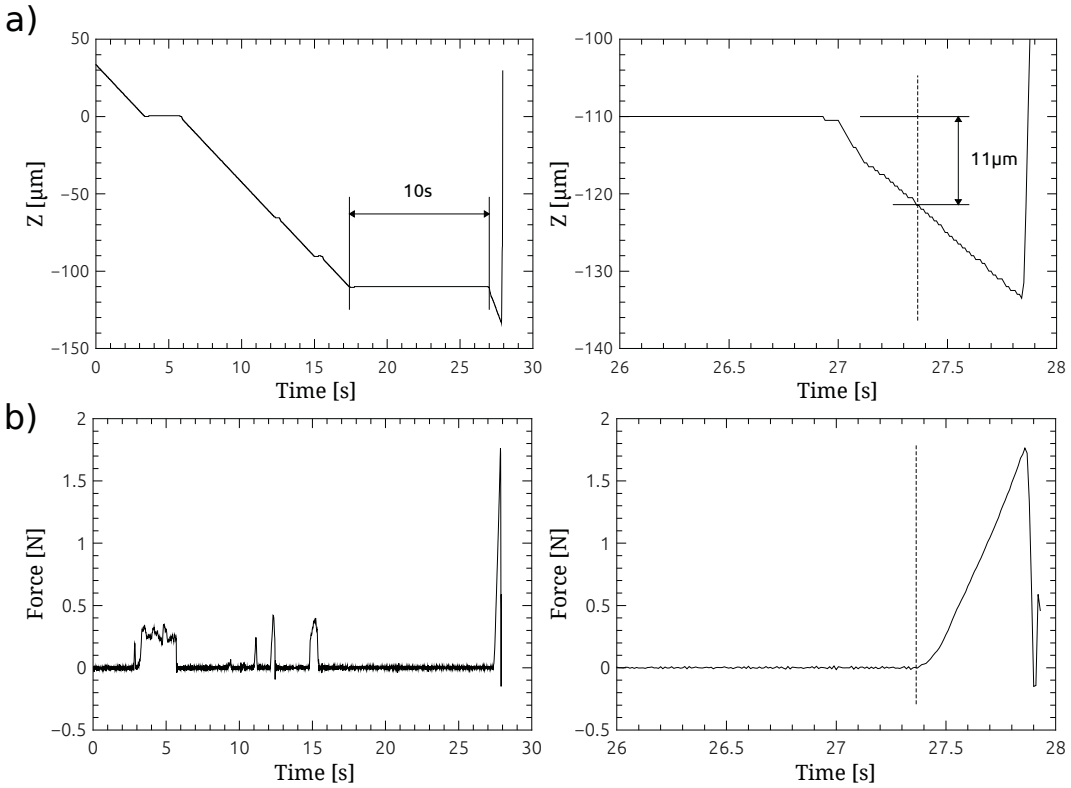

Figure 5.3: An example of the Z-stage motion and force signals recorded in function of time for one hole during the gap measurement. After drilling the hole, the tool is moved downwards until the glass surface is detected (seen through the force signal growth). a) Shows the Z-stage motion; b) Shows the force signal in function of time. The force is detected after a Z-stage motion of 11 μm.

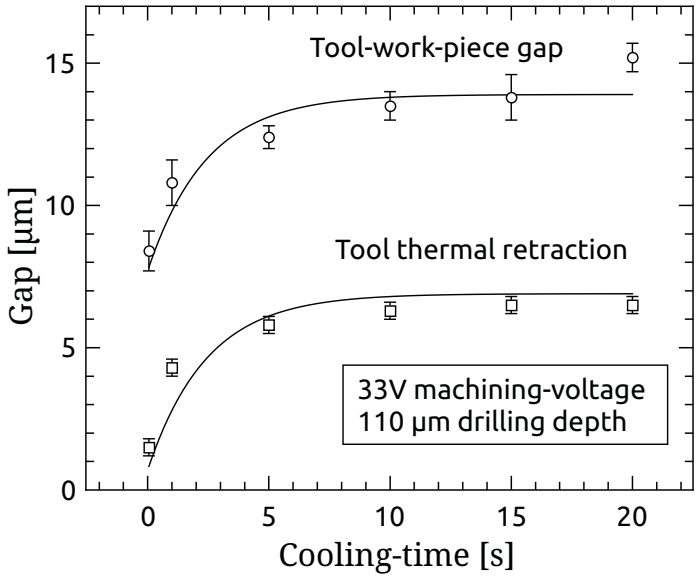

Figure 5.4: The measured gap and the tool thermal retraction in function of the cooling time for 110 μm drilling depth while applying 33 V. Both the gap and the tool retraction grow in the same manner.

conditions compared to the first measurement method (50 versus 300 measurements), it is used to quantify the machining gap in this work.

Based on Section 4.4, the hole bottom surface is deformed when the tool is pressed against it right after machining (both surfaces being hot). In this case, the two surfaces can even be bonded together. To avoid the occurrence of this phenomena during the gap measurement, it has to be ensured that sufficient time is allowed to cool down the machining zone. To determine the cooling time that has to be added before measuring the gap, the machined surface is examined after measuring the gap for different cooling times. For very low cooling times, the surface is expected to be deformed as soon as the tool contacts it while measuring the gap. However, for large enough cooling time, the surface has to remain unmodified.

To ensure that long enough cooling time is added such that the texture will not be affected by the gap measurement, different cooling times in the range of 50 ms to 20 s are applied and the corresponding surface texture is examined. For holes drilled using the same machining conditions, the measured gap must be independent of the cooling time. Figure 5.4 depicts the measured gap in function of the cooling time for the same set of machining conditions (110 μm deep holes machined using 500 μm tool while applying 33 V). Results show that the measured gap differs when varying the cooling time. In this case, the tool thermal retraction that changes in function of the cooling time (Figure 3.17), is not considered. Note that the thermal retraction for the various applied cooling times follows the same behaviour as the gap where it increases exponentially during the first 5 s and it reaches a stable value for

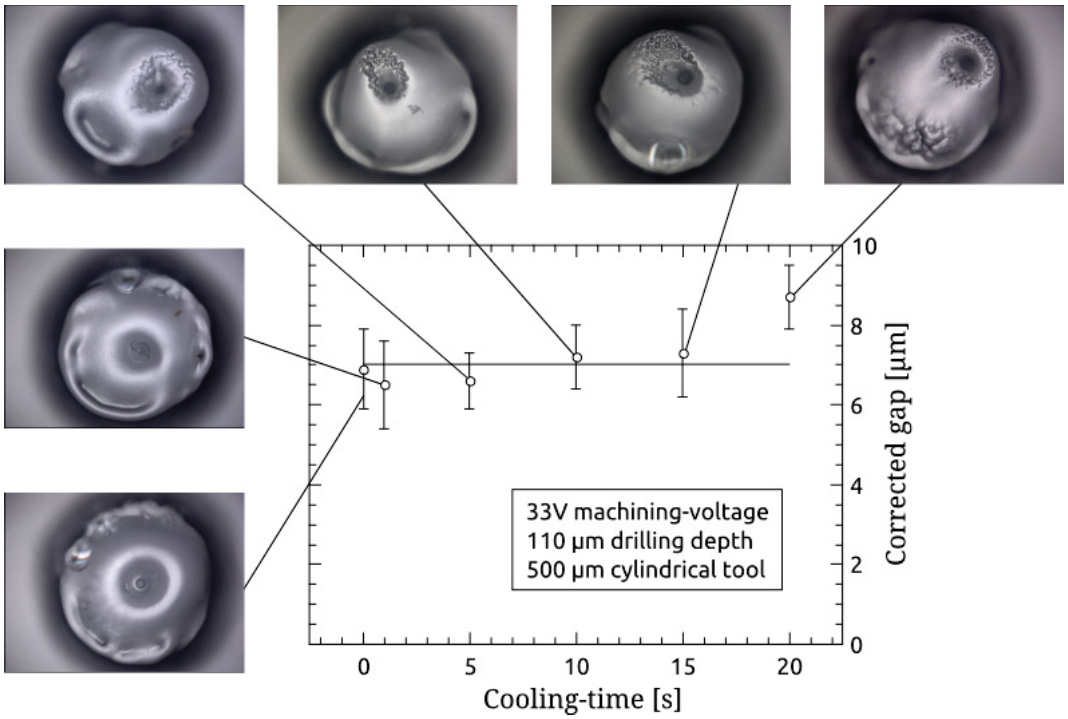

Figure 5.5: When correcting the gap for tool thermal retraction, a constant gap results for all cooling times. The bottom of the hole surface texture is the same for cooling times higher than 5 s and is smoother for lower cooling times.

cooling times above 5 s. The glass thermal expansion is considered negligible based on the discussion in Section 3.3.2. Figure 5.5 shows the corrected gap for tool thermal retraction where the gap is constant (around 7 μm in the present case) for all cooling times. These results validate the correctness of the developed gap measurement method.

Figure 5.5 also shows for different cooling times the typical resulting hole topography (taken with an optical microscope). For all cooling times, there is no clear imprint of the tool on the hole bottom surface. However, the surface patterns are different for low cooling times. In fact, the surface patterns that appear in the middle of the hole for cooling time above 5 s, are smoothed out for reduced cooling time. This is explained by the fact that the machining zone stays hot during a certain time after switching off the voltage (in this case during less than 5 s). Hence, the surface is further etched where the formed surface structures are smoothed out. Based on these results, a cooling time of 10 s is chosen while measuring the gap for various machining conditions.

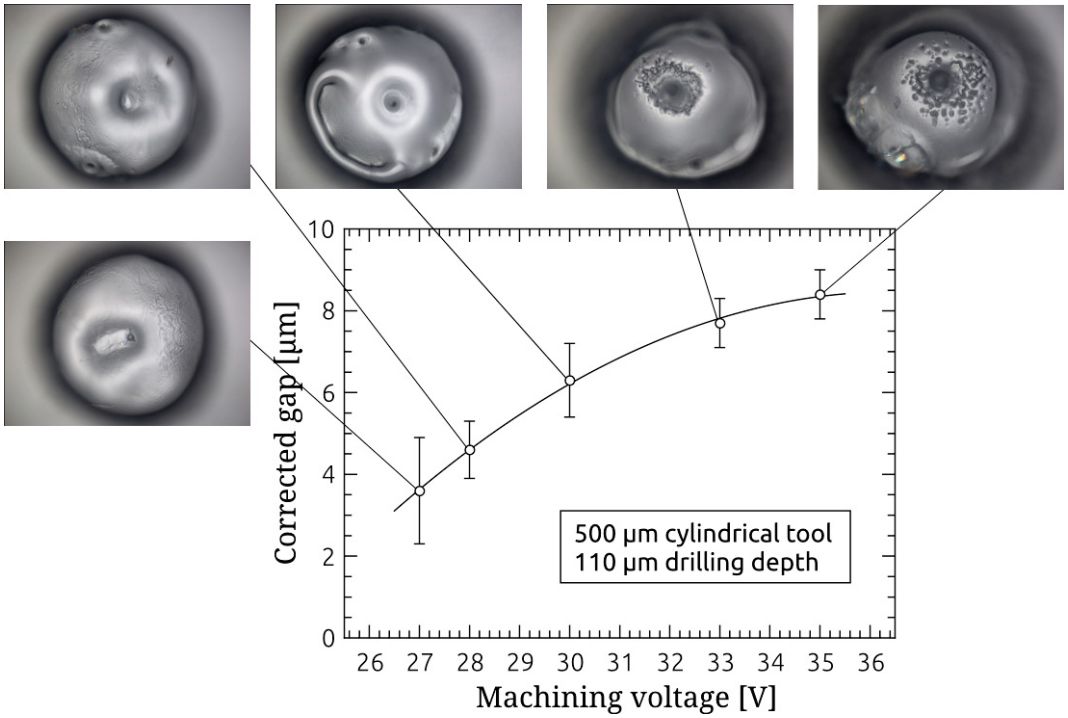

Figure 5.6: The tool-work piece gap vs. voltage magnitude for 110 μm deep holes while using 500 μm tool, 30 wt% NaOH and 10 s cooling time

5.3 Quantifying the machining gap

Chapter 4 showed that when increasing the machining voltage or when reducing the tool size forces appear at higher depths and the limiting tool feed-rate is larger. Based on Equation (5.5), the machining gap grows for higher tool temperature. Therefore, for increased voltage amplitude or duty cycle or when using tools with reduced diameter, larger gap is expected. In this case, the tool feed-rate limit must increase as the tool has to be moved faster before it contacts the glass surface. Chapter 4 also showed that for high machining depth, at which flushing limits material removal, the tool is always in contact with the glass surface (machining with zero forces is not possible). This has to be related to the size of the gap which must be reduced for higher depths (reduced material removal rate). All these arguments point out the link between the machining gap and both the local heating and flushing. To prove this claim, the machining gap is measured for different machining conditions allowing variable heating and flushing.

5.3.1 Effect of local heating on the machining gap

The local temperature is tuned by varying the machining voltage amplitude and duty cycle (Section 3.3.2). The correlation between the machining gap and the voltage amplitude

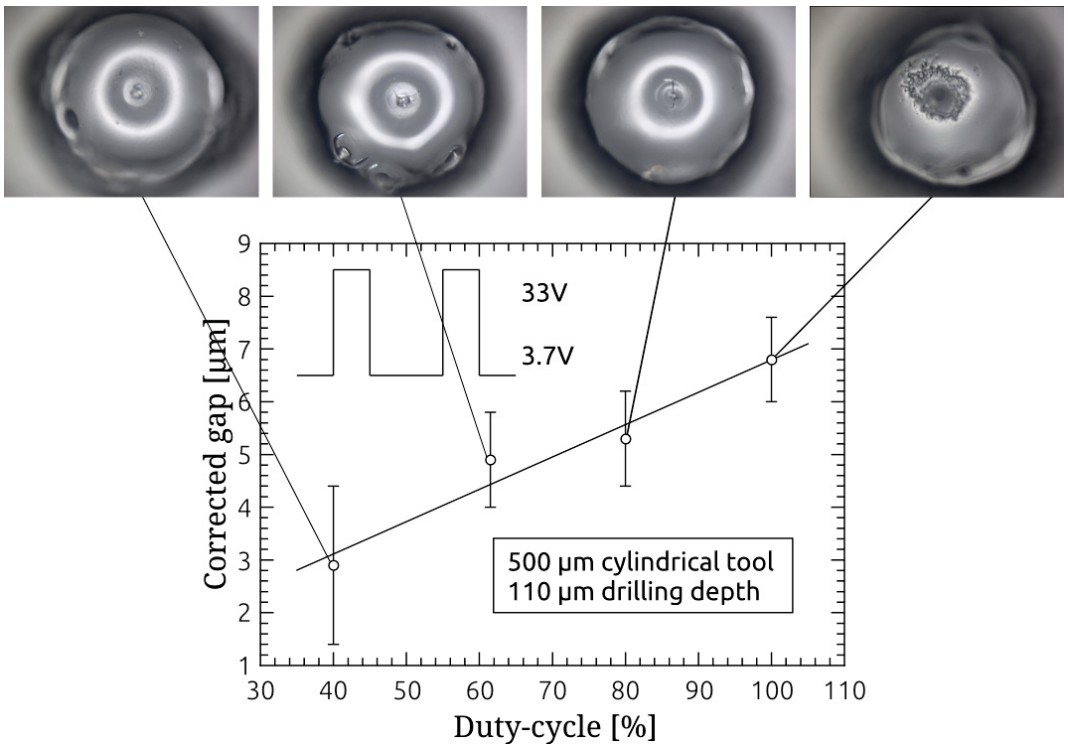

Figure 5.7: The tool-work piece gap vs. voltage duty-cycle for 110 μm deep holes drilled in 30 wt% NaOH while using 500 μm tool. 10 s cooling time and 33 V (3.7 V low edge) are applied.

and duty cycle is depicted in Figure 5.6 and Figure 5.7 respectively. The voltage is varied from 27 V to 35 V while the pulse duty cycle ranges from 20% to 80% (pulse-on-time 20 ms, pulse amplitude 30 V) for holes drilled in 30 wt% NaOH using 500 μm stainless steel tool. As claimed, the average gap increases for higher voltage amplitude and duty cycle. These results support the theory that higher local temperature results in a larger machining gap. As the pulsed voltage controls the gas film formation and breakdown, the resulting hole bottom surface patterns are smooth and defined for pulsed voltage when compared to DC voltage. Based on Figure 5.6, for DC voltage the surface patterns are different depending on the voltage amplitude. The bubble-like structures formed for high voltages are smoothed out for lower voltages (less than 30 V). The formation of these structures can be explained by the increased local turbulence due to the gas film breakdown for high applied voltage.

The tool thermal expansion is quantified following the method in Section 3.3.2 for the different applied voltage duty cycles and amplitudes. This allows estimating the tool temperature (Figure 3.18). Based on this, the gap measured for various voltage amplitudes and duty cycles is plotted in function of the local temperature (Figure 5.8). When taking λ_g to be equal to $0.17\lambda_l$, the calculated trend-line (Equation (5.5)) matches with the measured gap as shown in Figure 5.8. This indicates that the thermal conductivity in the machining

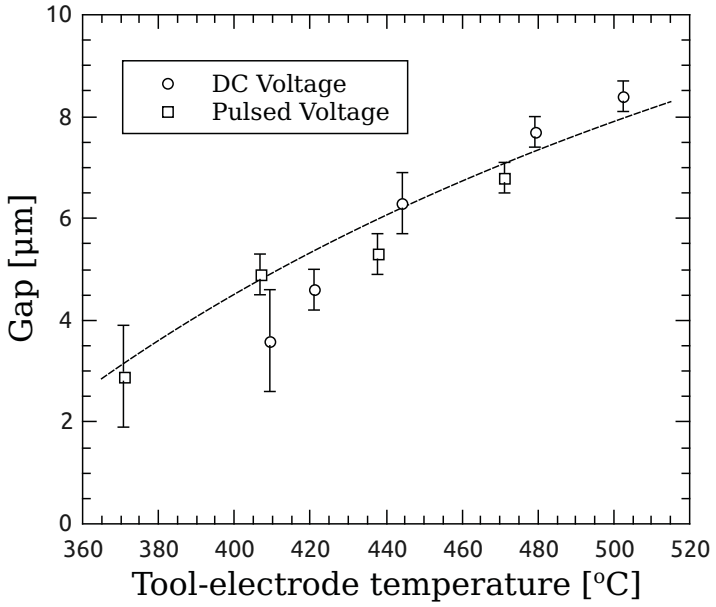

Figure 5.8: The measured and the calculated machining gap in function of the tool temperature. The gap measured for different voltage amplitude and duty cycle (Figures 5.6 and 5.7) is expressed in terms of tool temperature based on tool expansion measurement for each machining condition. The calculated trend-line (Equation (5.5)) matches with the measured gap for $\lambda_g = 0.17\lambda_l$.

gap is smaller than that of the electrolytic solution. In fact, the machined material and gas bubbles that are locally formed increase the thermal resistance in the gap. This proves the validity of the developed model.

The present results show that the gap is influenced by local temperature, where the last can be controlled by varying the machining conditions.

5.3.2 Effect of local flushing on the machining gap

Figure 5.9 shows the average measured gap for different machining depths ranging from 100 to 400 μm. The holes are drilled in 30 wt% NaOH using a 500 μm tool while applying 33 V. As expected, the gap is reduced for higher depths where flushing of hot electrolyte is limited. The resulting patterns formed on the machined hole bottom surface are similar for depths lower than 300 μm. For these depths, the surface is smooth and has some bubble-like surface structures that are formed due to the local turbulence caused by the gas film formation. More details about the surface texture are presented in Chapter 6. For higher depths, the machined surface has wavy-like patterns due to limited electrolyte flushing.

The present experimental results prove the theory that there exists a gap that is continuously formed during machining. The magnitude of this gap is in average less than 10 μm for holes drilled in 30 wt% NaOH when using a 500 μm tool and it depends on the local

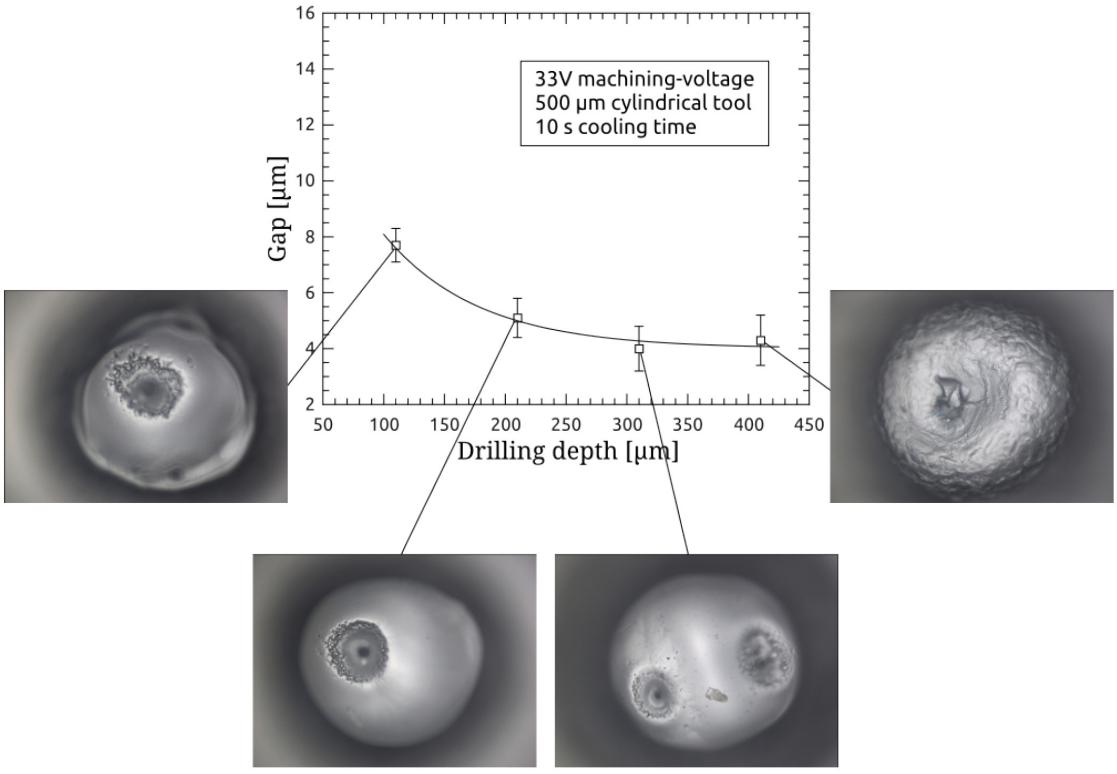

Figure 5.9: The tool-work piece gap vs. drilling depth for 500 μm tool, 30 wt% NaOH, 10 s cooling time and 33 V.

heating and flushing. Reduced local temperature and the shortage in the local electrolyte supply result in a smaller gap. This causes excessive tool-surface contact which deteriorates the machined surface geometry.

5.4 Conclusion

In this chapter, it is shown that during drilling a gap is created between the tool and the surface. This gap is dependent on the machining progress where it is reduced for limited material removal rate. The last is determined by the availability of local heating and flushing. In case of a small gap size, tool-work piece mechanical contact occurs resulting in machining forces.

A thermal heat transfer model that predicts the gap size is developed. The model is based on the idea that the gap stops growing when the local temperature drops to a value below the electrolyte salt melting point. The gap representation in normalized form shows its dependence on the local temperature. Further, a methodology to measure this gap is presented during which tool-surface gluing effect (Section 4.4) is prevented. Experiments show that for higher local temperature (higher voltage amplitude and duty cycle) the gap size is increased while it decreases for limited flushing (high hole depth). For a specific tool temperature, the measured gap matches with that predicted by the model which ensures the validity of the developed model.

Chapter 6

The machined surface and the mechanism of its formation

The question is not 'can you make a difference?' You already do make a difference. It's just a matter of what kind of difference you want to make, during your life on this planet....
(-Kitty Kolding)

Chapters 4 and 5 proved that both local heating and flushing are crucial for efficient drilling determined by increased machining gap size, implying enhanced material removal rate. As of today, there are still controversial opinions about the SACE machining process, even wrong conceptions exist. Some describe SACE as a combination of electrochemical machining (ECM) and electrical discharge machining (EDM) (Han et al., 2011; Panda and Yadava, 2009, 2012). These two processes are used to machine metals and the machining mechanism in both is different than that of SACE (e.g. in ECM the work-piece is dissolved anodically). Although it is generally agreed that during SACE the heat source from the discharges attacks the glass in some way, there is still confusion about the machining mechanism. In fact, three attack mechanisms are being debated in the literature:

- glass melting (Jain et al., 1999) (sic)
- localized glass sublimation by discharge impact (Kulkarni et al., 2003)
- high temperature etching (Yang et al., 2001)

Some of these theories are still vague while others are not yet verified. In this chapter the evolution of the machined surface is studied. Based on this and on a developed heat transfer

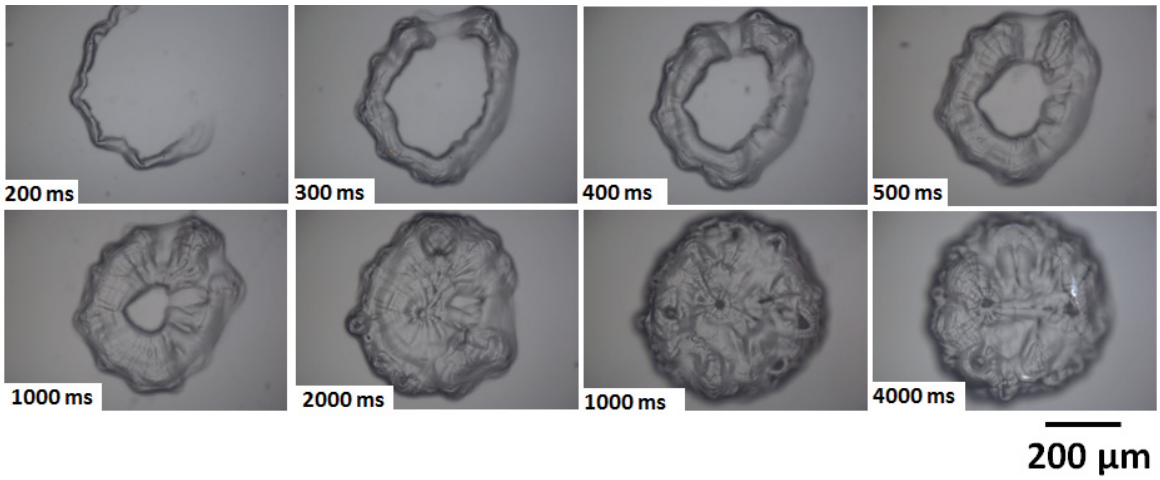

Figure 6.1: Evolution of the machined surface while using 500 μm tool 50 wt% KOH solution, 29 V and a range of machining durations (200 ms to 4 s).

model, the machining temperature during SACE is determined. Further, the origin of the formed surface texture is investigated and the SACE machining mechanism is clarified.

6.1 Machined surface evolution

It is well known in the field of SACE machining that high energy discharges are generated at the tool's sharp edges (Wüthrich, 2003). One can reasonably expect that the glass surface below these locations is heated. In case of a cylindrical tool, discharges are generated at the tool's circumference where the electrical field is the highest. Consequently, the glass has to be machined starting from the area below the tool's circumference (most heated spots) and must then grow radially towards the center of the hole.

Figure 6.1 shows the evolution of the glass surface machined in 50 wt% KOH solution using 500 μm diameter tool while applying 29 V for a range of machining durations starting from 200 ms up to 4 s. The tool is positioned 5 μm above the glass surface (detected using the profile-meter mode of the machining head) before switching on the machining voltage and it is kept at this position while machining. Note that when switching on the voltage the tool touches the glass surface since it expands by around 5 μm, measured based on the methodology developed in Section 3.3.2 (Figure 3.15). Results show that a ring is machined beneath the tool circumference during 300 ms and it grows radially towards the middle of the hole for longer machining time. For machining time less than 300 ms almost no etching occurs, where only a thin ring can be seen. This is in agreement with the thermal model in Section 3.3 predicting that 0.3 s are needed to heat up a 500 μm diameter stainless steel tool when 30 V is applied. Hence, the tool temperature has to be non-homogeneous for lower

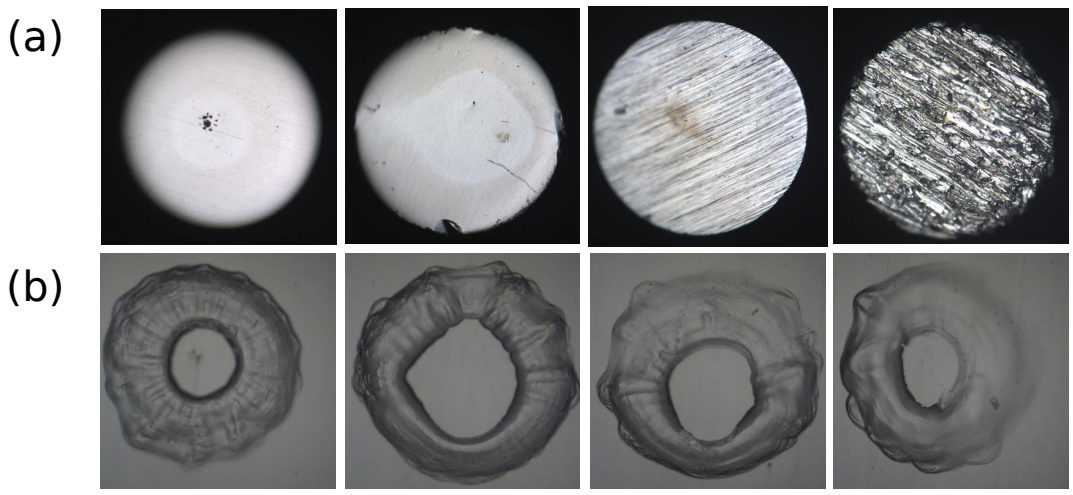

Figure 6.2: a) The bottom surface of 500 μm diameter tools polished using 320, 800, and 1200 grit sizes and using 1 μm-sized diamond paste suspension respectively. b) The resulting machined surface with each of these tools is shown (machining conducted in 50 wt% KOH solution while applying 29 V pulsed voltage, 20 ms on-time and 1 ms off-time, during 500 ms).

heating duration. As shown in Figure 6.1, the complete area beneath the tool is etched for machining duration above 1 s. These results indicate that the heat propagation on the glass surface is a significant factor in machining evolution. It is noticeable that irregularities appear on the machined surface. These irregularities may be caused by local turbulence or by discharges generated on the sharp edges of the tool bottom surface. In this case, for different tool bottom surface roughness the formed surface texture must change due to the different discharge activity.

To investigate this hypothesis, tools (500 μm in diameter) are polished with different grit sizes ranging from rough (320 grit) to smooth ones (1200 grit). Very smooth tool surfaces are obtained by polishing them with 1 μm-sized diamond particles suspension. The bottom surfaces of the polished tools and the corresponding glass surfaces machined using them in 50 wt% KOH while applying 29 V pulsed voltage (20 ms on-time and 1 ms off-time) during 500 ms are shown in Figure 6.2. It can be noticed that for some tools a semi-ring etched surface results. For these cases, the glass surface closest to the heat source, being the tool bottom surface, has to be initially etched[1]. The results shown on Figure 6.2c are in agreement with this claim, where the tool surface polished using the 1200 grit has a rectangular-shaped cavity and the glass surface area beneath this cavity is not machined. Only the glass surface area closest to the tool is machined (in this case this implies the area beneath the tool periphery where a ring-shaped area is etched).

[1]Misalignment exists between the tool bottom surface and the glass work-piece resulting in etching beneath the tool's bottom surface closest to the glass surface.

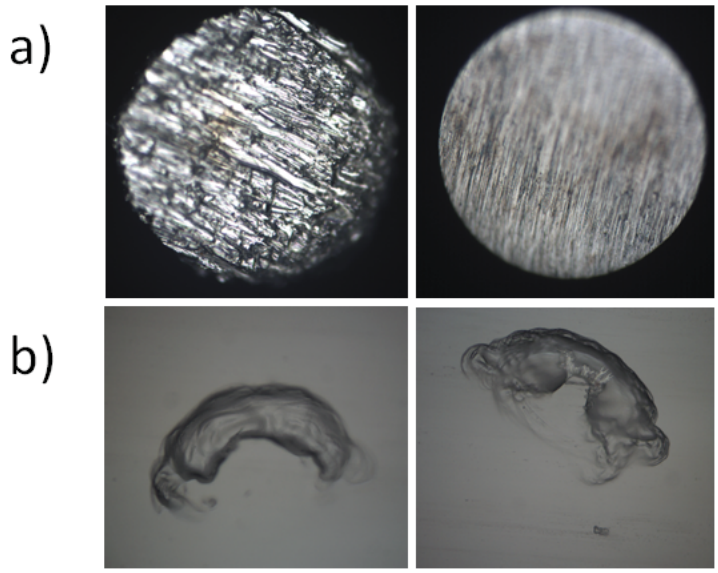

Figure 6.3: a) The bottom surface of 500 μm diameter tools polished using: 320 grit 1 μm-sized diamond particles, and b) the corresponding machined glass surfaces. Machining is done in 50 wt% KOH solution while applying 29 V pulsed voltage (20 ms on-time and 1 ms off-time) during 300 ms. For both tools the resulting glass surface is a partially etched ring. This is attributed to the non-flatness of the tool bottom surface and its misalignment with the glass surface.

Accordingly, the tool surface micro-roughness is not expected to influence the growth of the initially etched surface contrary to the flatness (macro-roughness) of the tool bottom surface and its alignment with the work-piece. The last influences how homogeneously the glass surface beneath the tool is initially heated. Figure 6.3 shows that a semi-ring is machined when using 500 μm diameter tools having different roughness (one tool is polished with 320 grit while the second is polished using 1 μm-sized diamond particles). Machining is done in 50 wt% KOH solution while applying 29 V pulsed voltage (20 ms on-time and 1 ms off-time) during 300 ms. In this case, as the bottom surface of both tools is not flat and the tools are not aligned with the glass work-piece, a non-homogeneously machined surface results for rough and smooth tools. This proves the validity of the mentioned hypothesis. All these observations show that the heat transferred to the glass surface is a significant factor in SACE machining.

6.2 Heat transfer model

Several methods were used to estimate the tool temperature during SACE machining including using thermocouples (Kellogg, 1950), performing spectroscopic measurements (Reghuram, 1994) and through local glass viscosity estimation (Jalali et al., 2009) in addition to the

new method proposed in this work (Section 3.3). However, no attempt was made to determine the glass local temperature for different machining conditions. Even the temperature needed for glass machining was assumed when developing models to predict the material removal rate. In fact, a different glass machining temperature was assumed in each model, for example 1193 K in (Fascio et al., 2004), 14000 K in (Bhondwe et al., 2006), 1423 K in (Panda and Yadava, 2009), and above 1093 K in (Jain et al., 1999). Still, similar machining rates were predicted by these models. This is due to the large number of variables that each model contains which can be tuned such that the estimated material removal rate matches with experimental findings for specific applied machining conditions.

The lack of a model that predicts reasonably the material removal rate is due to the limited understanding of the process, including the temperature required for glass machining by SACE. In this section, a simple heat transfer model is developed to estimate this temperature. The model considers that the heat source from the tool is located on the glass surface. The growth of the machined surface for certain machining conditions is simulated in ANSYS which allows obtaining the temperature gradient on the glass surface. Matching the temperature gradient and the size of machined surfaces allows estimating the temperature needed to machine glass assuming that flushing is not limited (depths at which no machining forces occur).

6.2.1 Model description

A semi-infinite thermal model is built to simulate the heat propagation in the work-piece. The simulated volume is taken to be infinitely larger than the size of the heat source to remove any external influence on the simulated heat generated.

For the thermal analysis, the following assumptions are made:

- The material (glass sheet) is homogeneous and isotropic where its properties are independent on temperature
- The thermal load distribution is uniform
- The heat transfer coefficient is constant
- The effect of natural convection and radiation is neglected

The temperature field $T(x, y, z, t)$ of the work-piece is obtained using a transient solution procedure governed by the following heat diffusion equation:

$$\lambda \left(\frac{\partial^2 T}{\partial^2 x} + \frac{\partial^2 T}{\partial^2 y} + \frac{\partial^2 T}{\partial^2 z} \right) = \rho C_p \frac{\partial T}{\partial t} \tag{6.1}$$

where λ is the thermal conductivity, ρ is the density and C_p is the specific heat of the work-piece. The initial temperature of the substrate is:

$$T(x, y, z, 0) = T_o \tag{6.2}$$

Boundary conditions on edges of the simulated volume are taken to be:

$$\frac{\partial T}{\partial n} = 0 \tag{6.3}$$

where n is the normal to the plane at which heat propagates. A different boundary condition is taken on a ring having the same diameter as the tool and a thickness of 10 μm:

$$\lambda \frac{\partial T}{\partial n} = -\dot{q} \tag{6.4}$$

where $\dot{q}$ is the heat flux generated by the discharges in the gas film during the SACE process.

The heat flux, which is circular, is taken as the thermal load where the heat source is considered to be located on the glass surface. The heat flux is the average discharge power divided by the heat source surface area A. The average discharge power is calculated based on Equation (3.19) as the product of the voltage U and the mean current I_A taken to be 29 V and 0.01 A respectively.

6.2.2 ANSYS simulation

The thermal analysis is conducted based on ANSYS simulations where the input parameters to the model are listed in Table 6.1. The heat source is taken to be a cylinder of outer diameter D_o (similar to the tool diameter) and inner diameter D_i, while the boundary volume is a cube of 10 mm side length. The initial temperature T_o of the glass is set at 22 °C. Tetrahedron elements and mapped face meshing were used in the model with a finer mesh around the heat source (applied circular thermal load) due to the larger temperature gradients around this zone. The final model consists of 382 elements.

An example of the simulation showing the temperature isotherms on the glass surface is depicted in Figure 6.4 for a machining duration of 1000 ms. The outer circular isotherm having the highest temperature, 450 °C, has a similar size as the tool diameter and the machined ring outer diameter (around 500 μm), while the isotherm in the center of the machined surface is at 190 °C. This simulation is done for different machining durations in order to estimate the temperature required to machine glass, considering that flushing is not limited (machining forces do not occur) as will be discussed in the following section.

Parameter	Value
Voltage U (V)	29
Mean current I_A (A)	0.01
Outer diameter source D_o (m)	$5 \cdot 10^{-4}$
Inner diameter source D_i (m)	$4.8 \cdot 10^{-4}$
Area A (m^2)	$1.54 \cdot 10^{-8}$
Heat flux q ($W \cdot m^2$)	$1.88 \cdot 10^7$
Work-piece density ρ ($Kg \cdot m^{-3}$)	2400
Work-piece thermal conductivity λ ($W \cdot m^{-1} \cdot K^{-1}$)	0.88
Specific heat C_p ($J \cdot Kg^{-1} \cdot °C^{-1}$)	840

Table 6.1: The input parameters to the ANSYS finite element model simulation.

6.2.3 Temperature needed for machining by SACE

In order to estimate the temperature needed to machine glass by SACE for the cases where flushing is not limited, the temperature isotherm having the same size as the machined surface (for defined machining durations) is found based on simulations. The surfaces are machined in 50 wt% KOH solution while the tool, 500 μm diameter, is in contact with the glass surface (errors caused by tool bending and thermal expansion are considered). A pulsed voltage supply (29 V, 20 ms on-time and 1 ms off-time) is used to have controlled local temperature (Figure 3.18b) and it is applied during different machining durations (100 to 1000 ms). To ensure a homogeneous heat transfer to the glass surface beneath the tool, the tool bottom surface has to be flat and aligned with the work-piece surface as demonstrated in Section 6.1. For this purpose, the tool is polished while mounted to the machining head in its regular position as while machining. The tool is moved downwards to slightly touch the sand paper, that is glued to the work-piece, and is rotated while being displaced on the paper during 1 min to polish its bottom surface. Following polishing, the tool is kept mounted inside the collet holder so that is stays aligned with the work-piece prior to machining (the sand paper is unglued). Figure 6.5 depicts the machined surfaces for the different machining times. It can be noticed that the rings are circular compared to the previously machined elliptical rings (Figure 6.1) resulting from tool-work piece misalignment and non-flat tool bottom surface.

Similar to the results obtained in Section 6.1, a ring is formed for small machining time and it grows into a fully etched circular surface for machining time above 700 ms. For any machining duration from 100 to 700 ms, the ring grows radially in the inward direction towards it center till reaching a certain diameter, called in this text *inner diameter* as presented on Figure 6.5 for the 300 ms machining time. The temperature corresponding to this diameter is extracted based on the finite element model simulations that show the temperature distribution on the glass surface for different machining durations. The size

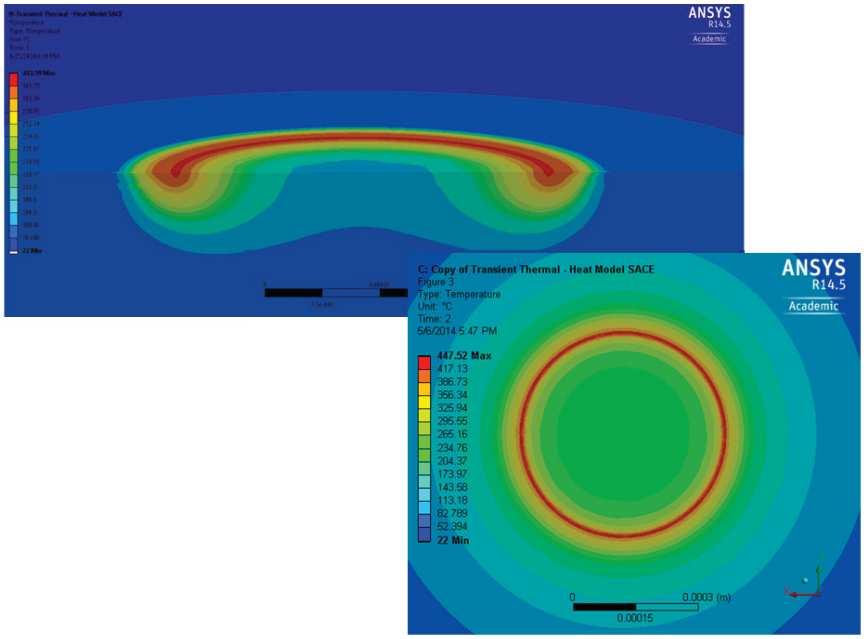

Figure 6.4: An example of the obtained heat isotherms from ANSYS simulation for 1000 ms machining time.

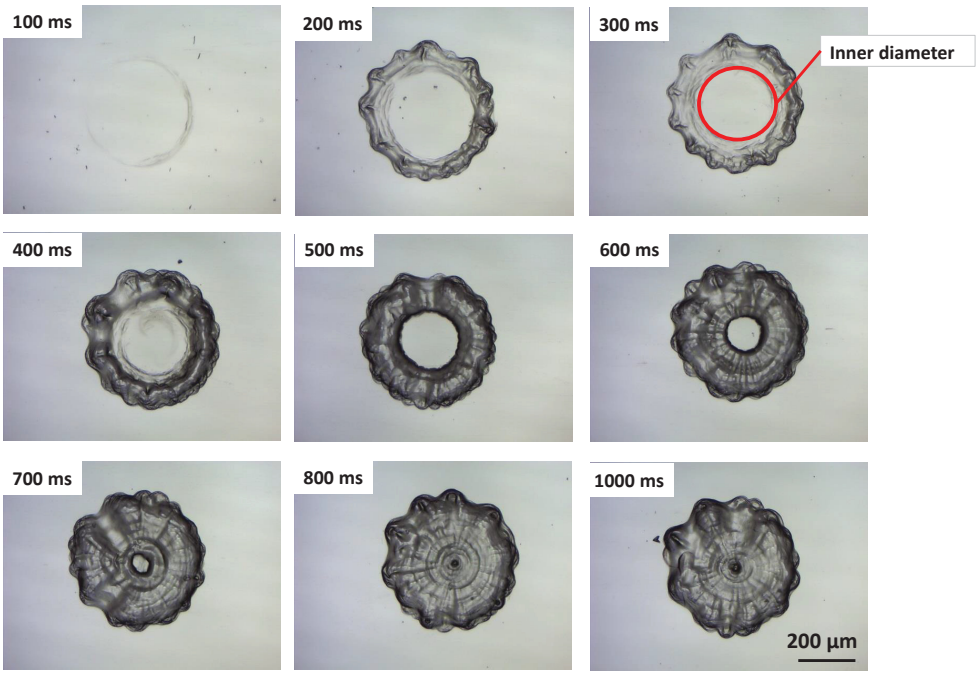

Figure 6.5: Evolution of the machined surface for different drilling durations ranging from 100 ms to 1000 ms using a 500 μm tool while applying 29 V pulsed voltage (20 ms on-time and 1 ms off-time).

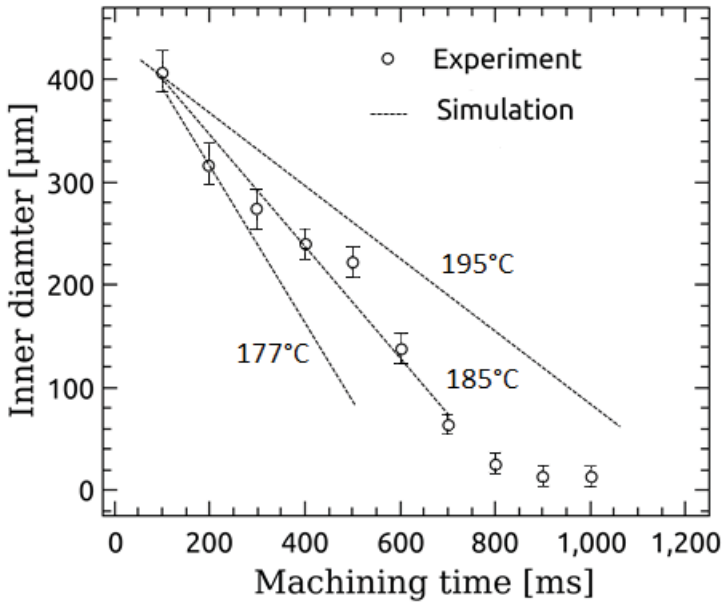

Figure 6.6: The machined ring inner diameter and the diameter corresponding to the most matching temperature isotherm, predicted by the model, for the various machining durations. The surface is not machined for temperature lower than 185 °C.

of the isotherm that best matches with the inner diameter corresponds to the machining temperature for depths where flushing is not limited.

The actual inner diameter found experimentally and the three closely matching diameters of temperature isotherms 177, 185 and 195 °Care plotted in Figure 6.6 for all the machining durations. It is found that the actual inner diameter corresponds to a temperature of around 185 °Cwhich is around the electrolyte vaporisation temperature. The imperfect match between the size of the 185 °C isotherm and the actual inner diameter, especially at high machining time, is due to the fact that the model neglects the effect of flow (natural convection) which becomes more dramatic for high machining time.

Based on these results, the machining temperature during SACE for cases where flushing is not limited is around the electrolyte vaporisation temperature.

6.2.4 Effect of the tool-glass gap on machined surfaces evolution

Based on the previous sections, the heat transfer from the tool to the glass surface proved to be an important factor in SACE machining where for higher machining time the machined surface grows. It was also demonstrated that the flatness of the tool bottom surface and its alignment with the work-piece surface influence the initially machined surface where the glass surface closest to the tool bottom surface is etched first. Therefore, varying the distance between the tool and the work-piece must affect the machined surface. In fact, when the

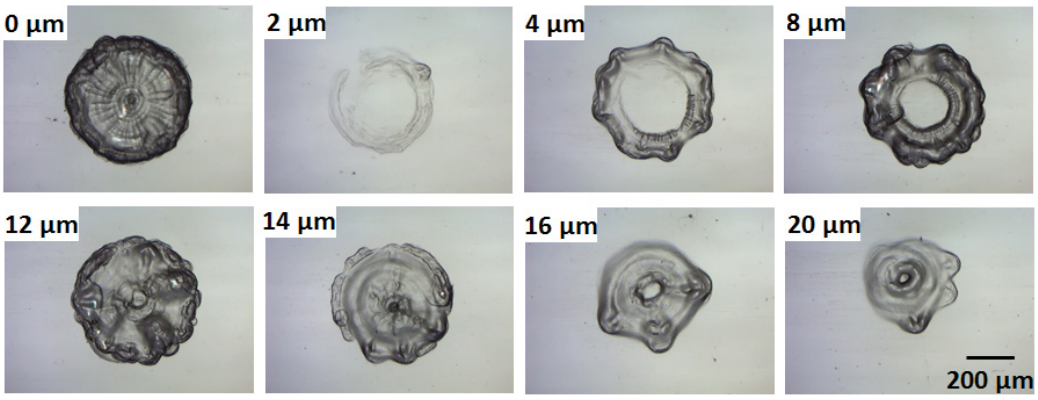

Figure 6.7: Evolution of the machined surface for different tool-work piece gaps (0 to 20 μm). The surface is machined while keeping the tool at a certain position above the work-piece (as indicated on each image). Surfaces are machining in 50 wt% KOH while applying 29 V during 2 s (pulse on-time 20 ms and 1 ms off-time).

tool (heat source) is on the glass surface machining must be very efficient since the heat is well transferred to the glass (as in gravity-feed drilling). If a small distance exists between the tool and the glass surface, machining must still occur given that this distance is large enough to allow evacuating the gas bubbles (heat resistance) from beneath the tool and small enough to allow heat transfer to the glass.

Figure 6.7 shows the evolution of the surface machined in 50 wt% KOH solution, while applying 29 V pulsed voltage (on-time 20 ms and 1 ms off-time) during 2 s, in function of the distance between the tool and the work-piece. The glass surface is detected using the profile-meter function of the machining head and the tool is positioned at different distances away from the surface (0 to 20 μm after correcting for tool bending and expansion). Machining is conducted while the tool is fixed at the same Z-position.

Results show that for 0 μm distance the surface is completely machined. A thin ring is machined for 2 μm distance after which it becomes more pronounced for larger distance up to around 12 μm. Beyond this distance, the machined surface area becomes smaller. These results are, as expected, due to the trade-off between allowing enough space for both the gas film to form properly and the electrolyte to flow beneath the tool on one side, and keeping the heat source (tool) close enough to the glass surface to ensure proper surface heating, on the other side.

This trade-off explains the negligible machining for 2 μm distance. For this specific gap the bubbles ejected due to the gas film breakdown are trapped beneath the tool, hence filling up the gap. The bubbles isolate the tool from the glass surface resulting in almost no machining. This is in agreement with the theory presented by (Basak and Ghosh, 1996) where when modelling the discharge generation from the tool, the flow of the current through

the bottom surface area of the tool was neglected by considering that this area is permanently blanketed by the entrapped bubbles. The situation is different for 0 μm distance, where in this case the tool presses on the glass surface leaving almost no room for gas bubbles to get trapped beneath it.

The results presented in this section prove that the local heat transfer to the glass surface is a crucial factor in the machining evolution. By matching the experimentally measured growth of the machined surface with the simulated one, it is found that the temperature below which machining does not occur, for the case where flushing is not limited, is similar to the electrolyte vaporisation temperature. It is also demonstrated that the tool-work piece gap affects the machined surface evolution where it enhances machining if it is large enough to allow flushing the locally generated bubbles and small enough to permit transferring heat to the glass surface.

6.3 Origin of the surface texture

One of the yet not explained phenomena of SACE micro-machining is the formation of various surface textures. In fact, the origin of the surface texture has never been investigated previously. It is known that during the SACE process the gas film forms and breaks down every few milliseconds, causing local turbulence in the tool vicinity (Wüthrich, 2009) which results in complex local flow (Ghorbani, 2012). In Chapter 5, it is shown that the machined surface patterns resulting from applying pulsed voltage are more uniform than those obtained using DC voltage. This was attributed to both controlled gas film dynamics (breakdown and formation) and local heat generation for pulsed voltage supply contrary to DC voltage. In fact, the difference in the surface patterns in both cases must be caused by the local flow. Further, the jagged contours formed for small machining time, as small as 200 ms (Section 6.2, Figure 6.5) must be the result of local turbulences. Hence, it is expected that during drilling the electrolyte flows in the tool's vicinity where this flow has to be the result of the gas film continuous formation and breakdown in addition to being affected by convection and possibly by the high local magnetic and electric fields. Figure 6.8 shows the bottom surface of a 300 μm deep hole machined in 30 wt% NaOH while applying 30 V. Two bump-like structures surrounded with tiny bubble-like structures appear on the surface. The location of these bumps on the machined surface changes for different holes, as shown in Figure 6.8, although both holes are machined using the same tool and in absence of tool rotation. This indicates that these structures are not a result of the tool texture, rather they must be caused by the local flow of hot electrolyte in the tool vicinity. A likely possibility is that the surface formed bump-like structures are a result of the last gas film breakdown

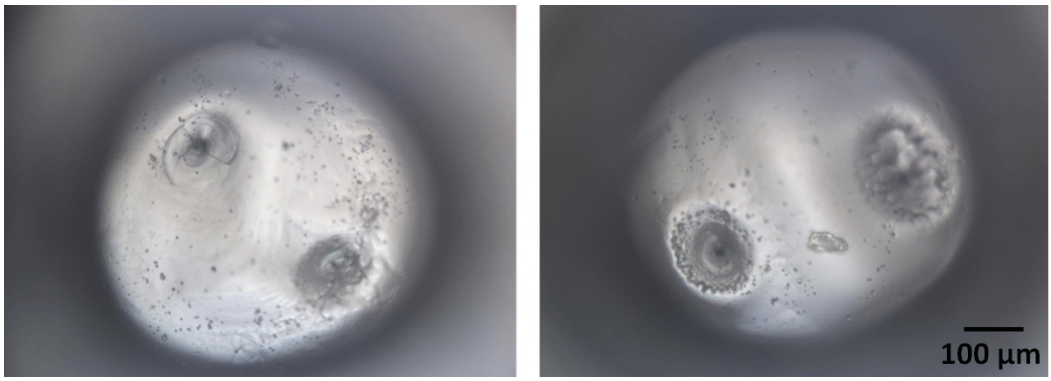

Figure 6.8: Micro structures formed on the bottom surface of 300 μm deep holes machined in 30 wt% NaOH using 30 V and a 500 μm tool.

at the instant the voltage is switched off. In this case, the final generated bubbles jet causes local turbulence, hence leaving an imprint on the surface in the form of structures.

6.3.1 Effect of imposed tool motion

Following these findings, one expects to see a different surface texture if a forced flow is added by rotating the tool. In this case, the texture will be the result of two flows: one due to the gas film dynamics and the second due to the tool motion.

To examine the correctness of this claim, machining is conducted in low viscosity electrolyte such that the flow can be easily affected by the tool motion. For the present experiments, 50 wt% KOH solution is chosen while 29 V is applied during 10 s for various tool rotational speeds (0 to 2500 rpm). The tool is positioned 5 μm above the glass surface (using the profile-meter) and is fixed at the same position while the voltage is turned on. To prevent vibration of the flexible structure due to spindle rotation, the machining head stiffness is made very high using the second mode of the force sensor (operated based on the zero displacement force measurement principle). A PID controller is implemented for this purpose where the forces resulting from vibrations are compensated using the voice coil actuator. The flexible structure displacement z is recorded in function of time (Figure 6.9) for the different rotational speeds used (500 to 3000 rpm). For all rotational speeds the amplitude of vibration is well below 2 μm. Hence, the implemented controller is sufficient for the purpose of the present experiments.

Figure 6.10 shows the surfaces machined in 50 wt% KOH while rotating the tool at different speeds (0 to 2400 rpm, increments of 300 rpm) and applying 29 V during 10 s. For rotational speeds lower than 900 rpm crater-like and bump-like structures appear on the machined surface. Starting from 900 rpm the middle area is smoother and feathery patterns

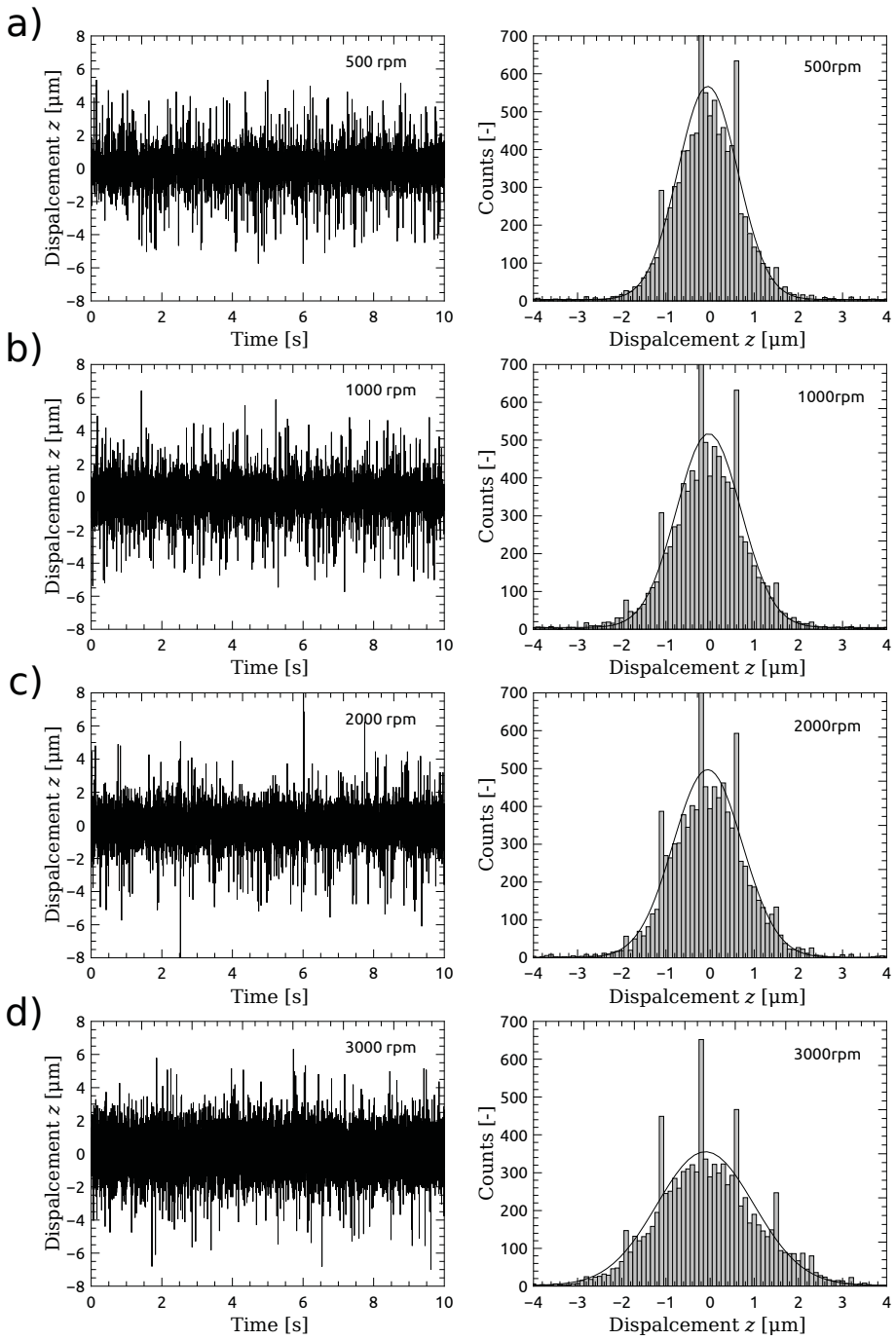

Figure 6.9: Flexible structure displacement z in function of time for various tool rotational speeds: a) 500, b) 1000, c) 2000 and d) 3000 rpm. The vibration amplitude caused by tool rotation is below 2 μm.

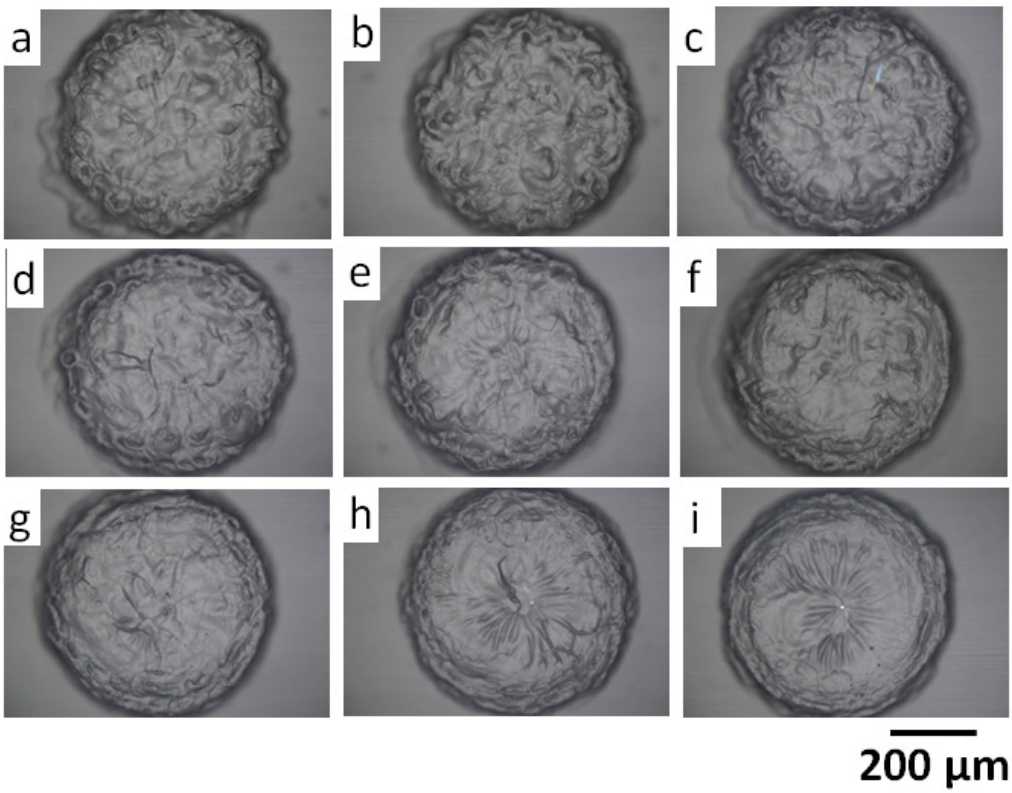

Figure 6.10: Surface texture for holes machined during 10 s in 50 wt% KOH solution while keeping the tool at the same position (it initially touches the surface). 29 V is applied while rotating the tool at different speeds (0 to 2400 rpm, increments of 300 rpm).

result. For rotational speeds higher than 1500 rpm, feathery patterns formed in the middle area of the machined surface become more pronounced while spiral-like patterns appear on the hole's circumference. This texture must be the result of two types of flow: radial and rotational. The first is attributed to the pressure created by the gas film reformation that pushes the electrolyte radially away from the center of the hole, while the second is caused by the tool rotation. Crater-like structures and bumps appear on the surface for low tool rotational speeds as the temperature is higher compared to high speeds. In this case, the intense discharge activity (more etching) and the unstable gas film cause highly turbulent flow which results in forming crater-like structures. These results support the claim that the texture is indeed created by the local flow.

The appearance of spirals starting from rotational speeds higher than 1500 rpm, for the applied machining conditions, has to be directly related to the machining zone temperature. This link has already been highlighted in Chapter 4, where it is shown that for high rotational speeds flushing is intensive which causes a reduced machining zone temperature due to forced convection. This results in a reduced gap size (Equation (5.5)). For small gap, the flow in the tool vicinity has to be clearly imprinted on the surface. Thus, spiral-like patterns are expected for high tool rotational speeds (small gap). For low tool rotation speeds, a larger gap must be formed (higher local temperature) causing the spiral-like flow patterns, in the tool vicinity, to be most likely flushed away before being imprinted on the surface. Therefore, radial feathery-like flow patterns, caused by the pressure the gas film creates upon its reformation, are imprinted on the surface. This effect is enhanced for large gaps as the gas film has more space to properly form. Therefore, it becomes reasonable to claim that the surface patterns are to some extent an imprint of the local flow patterns in the machining gap. This is further investigated in the next section.

6.3.2 Effect of tool-surface gap

So far, observations point out that the local flow of hot electrolyte determines the surface texture. This flow is influenced by the gas film dynamics and the forced flow due to tool rotation and must be also affected by the tool geometry and the machining gap. The last is influenced by the local temperature (Equation (5.5)) which can be tuned by varying the heat source from the discharges (Equation (3.19)) through adjusting the voltage amplitude and duty cycle. However, the local temperature is not only determined by the heat source but is also affected by the local convective flow. Therefore, controlling the local flow is a highly coupled problem.

Based on the previous section, it is expected that the formed surface texture is a result of

imprinting local flow patterns either completely or partially on the surface which depends on the machining gap. For a small gap, local flow patterns are expected to be fully imprinted on the surface while they must be less pronounced for higher gaps.

As the gap size is influenced by the applied voltage (Chapter 5, Figure 5.6), different surface patterns must be formed when varying the voltage. In presence of tool rotation, the local temperature resulting from applying high voltages and high tool rotational speeds has to be similar to that caused in case the voltage and tool rotational speed are reduced. This is based on the idea that the enhanced heat transferred to the machining zone, due to the increase in voltage, must be counteracted by increased heat dissipation, due to the higher tool rotational speeds. Therefore, in both cases mentioned a similar gap must result and, hence, a similar surface texture.

Figure 6.11 shows the surface texture for 400 μm deep holes machined in 50 wt% KOH for various tool rotational speeds (300 to 1800 rpm, increments of 300 rpm) and voltages (29, 30 and 33 V). The typical recorded force signal for each set of machining conditions is also plotted. Prior to drilling, the tool is initially positioned 50 μm above the glass, and the voltage is switched on during 20 s to heat the electrolyte and the tool. Drilling proceeds by moving the tool downwards at 10 μm/s. Whenever the force exceeds 0.5 N, the tool is moved upwards by 10 μm to remove the forces. Figure 6.11 shows that for the highest machining voltage (33 V) crater-like structures form on the surface for all the tool rotational speeds. This can be explained by the high local temperature which causes more intense discharges, a larger machining gap and a turbulent flow locally. Therefore, crater-like and bump-like structures are expected to be imprinted on the surface. As the voltage is reduced to 30 V, crater-like patterns appear for low rotational speeds (less than 600 rpm) and for higher speeds spiral-like patterns (with some feathery-like radial patterns in the center) are formed. For very low voltage (29 V), spiral patterns appear clearly on the surface for all rotational speeds. The trend in the surface texture relative to the tool rotational speed and the applied voltage is as expected. The key idea is that the gap size, which is dependant on the local temperature, affects the imprinted surface patterns. This supports the claim that the texture is an imprint of the local flow patterns in the machining gap where they are more pronounced for reduced gap size.

During drilling at a constant tool feed-rate, the measured forces are due to the tool-glass contact and their occurrence is dictated by how large the average size of the gap is. If the rate of gap formation is faster than the tool feed-rate, zero forces must result. As the gap controls the surface texture and is related to the drilling forces occurrence, it becomes possible to use the force signal in order to predict the formed surface texture on-line while machining. In fact, Figure 6.11 shows the typically measured force signal for each voltage. For low voltage,

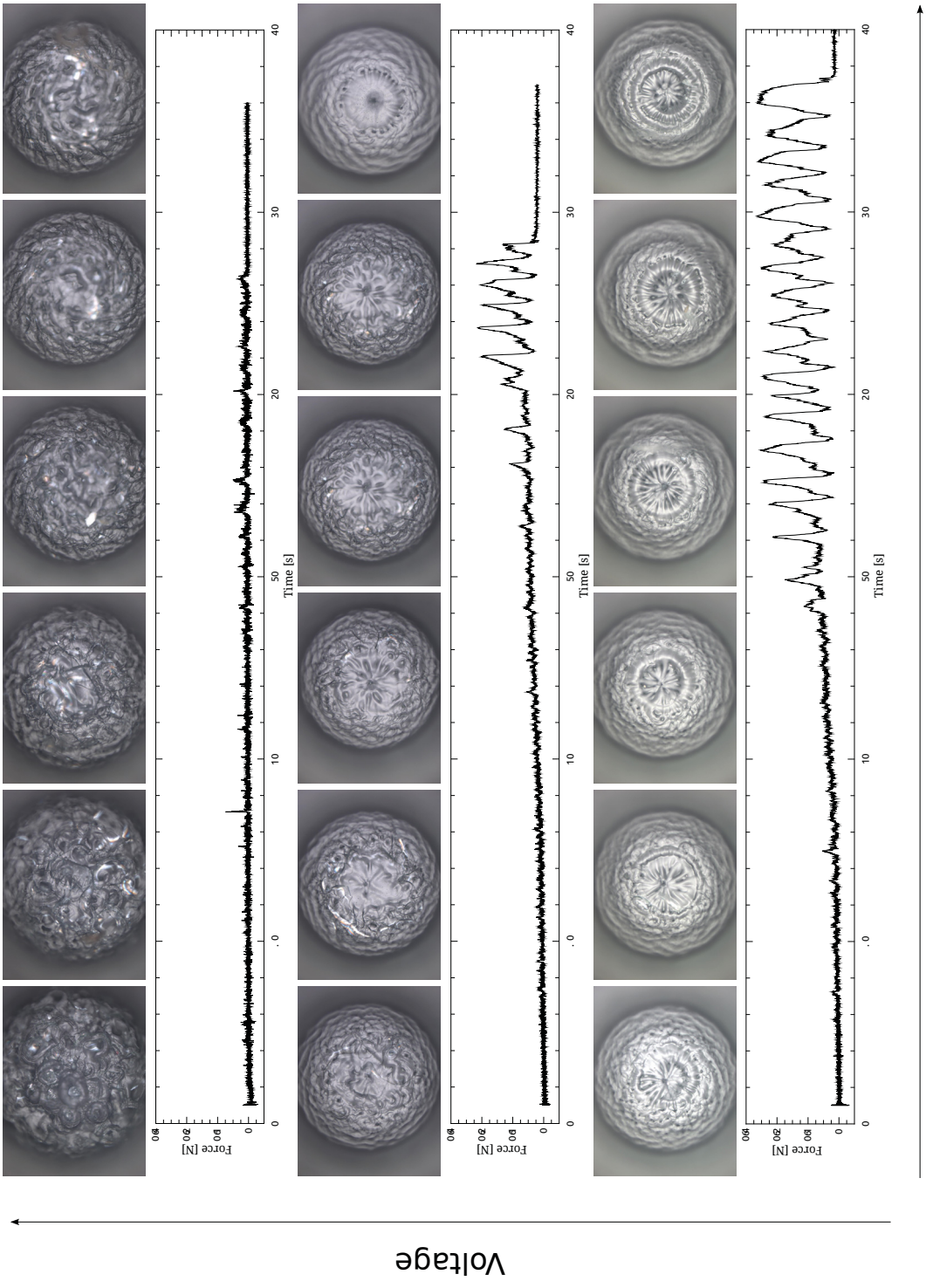

Figure 6.11: Surface texture for 400 μm deep holes machined in 50 wt% KOH while applying different tool rotational speeds (300 to 1800 rpm, increments of 300 rpm) and voltages (29, 30 and 33 V). For each set of machining conditions the typical recorded force signal is shown.

forces occur frequently resulting in several tool upward movements. This ensures that the gap is small where the local flow patterns are generated near the machined surface. In this case, spiral-like patterns caused by tool rotation get imprinted on the surface. For high voltages spiral-like patterns will be flushed since a larger gap, ensured by the existence of little forces, is formed. In this case, the spiral-like flow patterns are away from the machined surface where they get flushed before being imprinted on it. Therefore, only bumps and crater-like structures appear on the surface. The outcome of these experiments further supports the theory that the local flow in the machining gap is responsible for the formed texture.

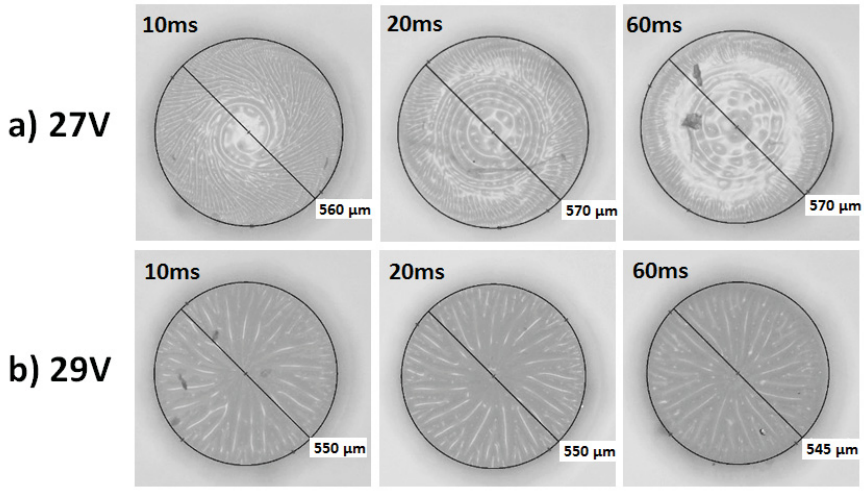

Figure 6.12: The bottom surface of 300 μm deep holes machined using 50 wt% KOH while rotating the tool at 1500 rpm and applying pulsed voltage (27 and 29 V) of variable duty cycle (2 ms pulse off-time). The low-pulse edge is fixed to 7 V.

Based on these findings, different surface pattens must be formed when applying pulsed voltage with various duty-cycles as the machining gap must differ in this case (Chapter 5, Figure 5.7). Figure 6.12 shows the bottom surface of 300 μm deep holes machined using 50 wt% KOH while rotating the tool at 1500 rpm and applying pulsed voltage (27 and 29 V) of variable duty cycle (2 ms pulse off-time). The low pulse edge is fixed to 7 V to prevent tool dissolution. Results show that for 27 V spiral-like patterns are pronounced on the surface for the lowest duty cycle (10 ms on-time) and they become less apparent for higher duty-cycles. This is, as expected, due to the higher machining gap formed for increased pulse duty-cycle (around 15 μm compared to less than 10 μm for the lowest duty cycle) which results in flushing the flow patterns created in the tool tip vicinity.

For increased voltage amplitude, a larger gap must result where spirals have to be even less pronounced than for low voltage. This is indeed the case as shown in Figure 6.12 where radial feathery-like patterns are formed on the hole bottom surface for all applied duty-cycles (10 to 60 ms on-time) when increasing the voltage to 29 V. This is attributed to the gas film

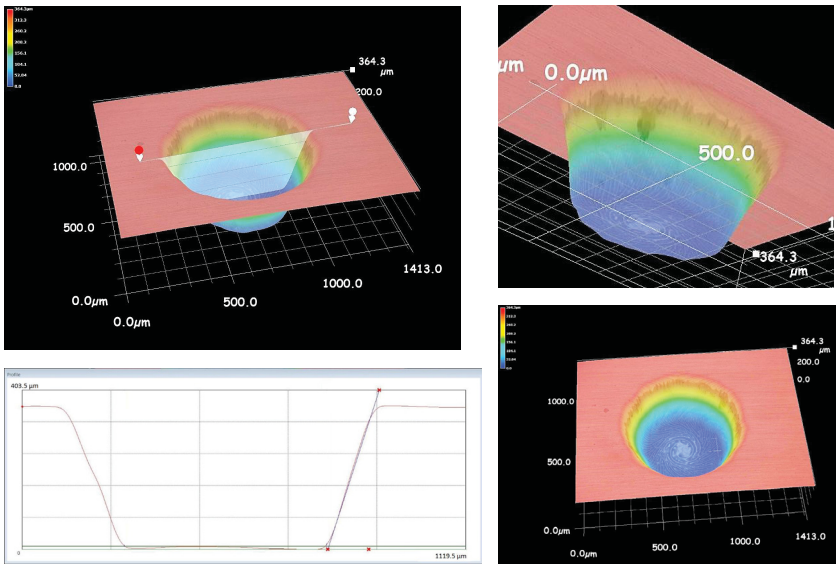

Figure 6.13: An example of a 3-D image showing the flatness of the hole bottom surface machined in 50 wt% KOH while applying 29 V pulsed voltage (10 ms on-time and 2 ms off-time).

dynamics where its reformation pushes the electrolyte radially away from the center of the hole. The gap in this case is higher than that for 27 V (above 20 μm).

A collection of 3-D views showing a hole machined while applying 1500 rpm, 10 ms duty-cycle and 27 V and the corresponding measured profile are shown in Figure 6.13. The image is taken using a 3-D optical microscope (Keyence: VH-Z500W lens, VHX-1100 camera). The microscope builds an image of the hole profile by assembling a series of images that it takes while moving in the Z-direction along the hole depth (5 μm steps). The 3-D profile views of the hole demonstrate that the hole bottom surface, on which the spirals are imprinted, is flat and that the hole has a V-shaped profile.

All the observations in this section show that the key in the local formed surface texture is the flow of hot electrolyte in the machining gap. How well these patterns are imprinted on the surface highly depends on the size of the machining gap (more pronounced patterns for reduced gap).

6.3.3 Flow in 2-D machining

To better visualize the local flow patterns, 2-D channels are machined. Similar to holes, the texture of 2-D machined surfaces must be determined by the local flow. The last has to be influenced by global electrolyte properties as this was the case for holes where flushing is more limited. In fact, the surface texture of drilled holes is found to change from feathery-like to smooth when increasing the electrolyte viscosity. Therefore, a variety of textures must

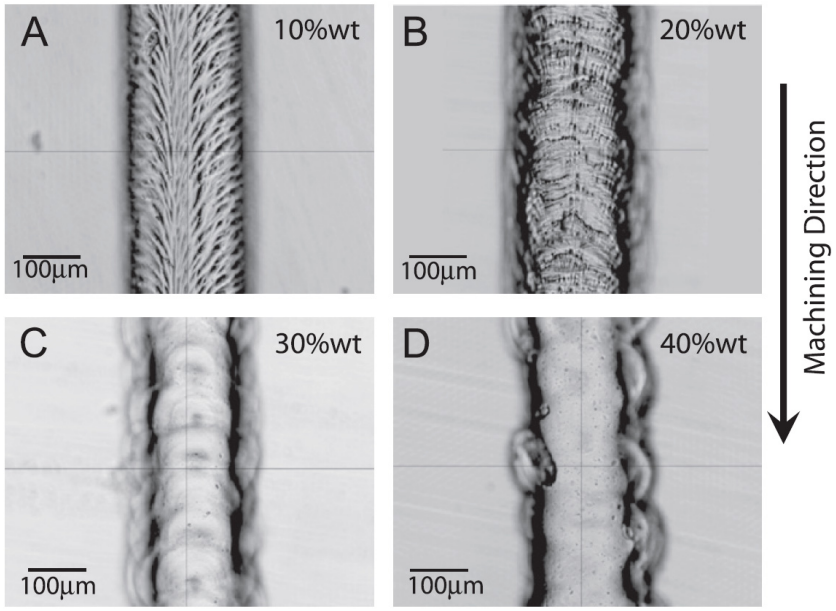

Figure 6.14: The channel surface texture obtained using different NaOH electrolyte concentration ranging from 10 to 40 wt% and while applying 28 V and 5 μm/s tool-travel speed. The texture is feathery-like for low electrolyte concentration and becomes smoother for increased electrolyte concentration. Reprinted from (AbouZiki et al., 2012) with permission from Elsevier.

form on channel surfaces when using electrolyte of various viscosities, due to the different resulting local flow patterns in each case.

The viscosity is varied using different NaOH concentrations, from a viscosity similar to that of water (10 wt%) to a viscosity more than 20 times higher (40 wt%). Figure 6.14 depicts typical 2-D micro channels machined for each concentration, ranging from 10 to 40 wt% NaOH, for applied 28 V and 5 μm/s tool-travel speed. The texture evolves from feathery-like for the lowest electrolyte viscosity to spongy-like smooth texture for the highest one. This is explained by the different local flow, caused by gas film dynamics, occurring in electrolytic solutions of various viscosities. For 10 wt%, the feathery-like patterns diverge in the direction opposite to that of the tool-travel direction. In this case, the feathers are dragged by the tool where they converge in the center of the channel where the tool tip passes. These patterns behave in a manner similar to Kelvin wake patterns left behind a body moving in water. The angle the feathery-patterns make with respect to the tool-travel direction is around 37 °, similar to that created by Kelvin wake patterns (Reed and Milgram, 2002). Therefore, the flow in 2-D channels is also caused by the gas film dynamics and the tool motion. Note that 10 wt% NaOH has similar viscosity as 50 wt% KOH and for both feathery-like patterns are obtained (on hole and channel surfaces). This shows that the local flow patterns are indeed affected by the global electrolyte viscosity.

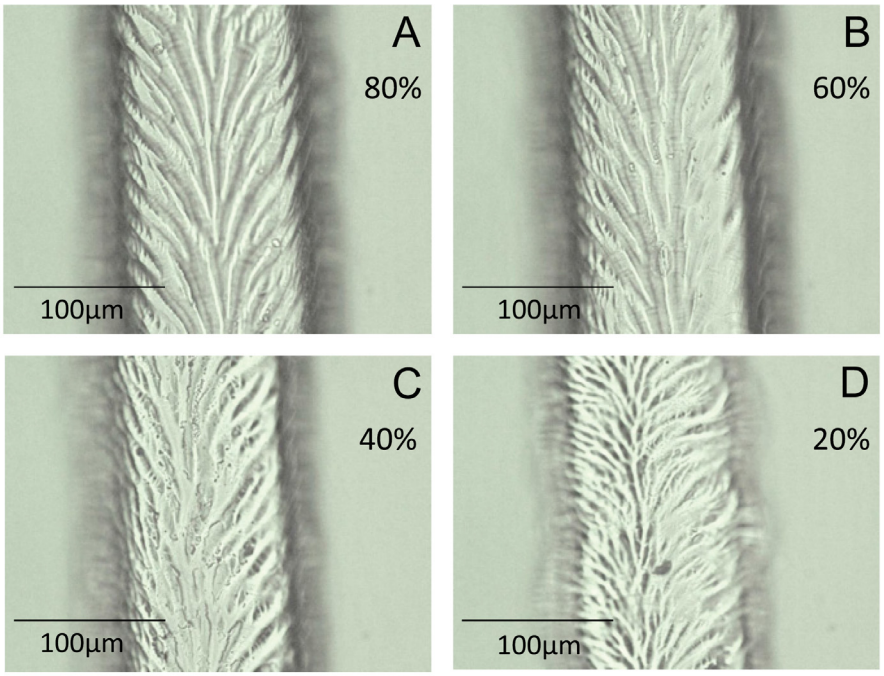

Figure 6.15: The channel surface texture obtained for 10 wt% NaOH solution, 28 V and 5 μm/s tool-travel speed while applying different voltage duty cycles ranging from 80 to 20 % (80 ms pulse-on-time). Reprinted from (AbouZiki et al., 2012) with permission from Elsevier.

As flushing is not limited in 2-D machining, the surface must be flushed the same way. Hence, local temperature fluctuations must be reduced compared to the case of a hole. To examine the correctness of this claim, channels machined using pulse voltage, which results in different local temperature, are compared. Figure 6.15 shows the resulting patterns when applying duty cycles ranging from 20 % to 80 % (80 ms pulse-on-time) for 10 wt% NaOH solution, 28 V and 5 μm/s tool-travel speed. Figure 6.15 shows that for the same electrolytic solution (in this case 10 wt%), all the textures belong to the feathery-like family of patterns. Only a non-pronounced difference in the structure of the feathers could be observed when comparing the highest and lowest duty cycles.

These results further prove the theory that the surface patterns in 1-D and 2-D machining are an imprint of the electrolyte flow patterns in the tool vicinity. These flow patterns have two sources: the gas film dynamics and the tool motion and they are influenced by the bulk electrolyte properties.

6.4 Machining mechanism

Based on the findings in this chapter, the machining mechanism is hypothesized to be a combination of (Figure 6.16):

- Thermal assisted etching
- Physical bombardment with hot discharge channels

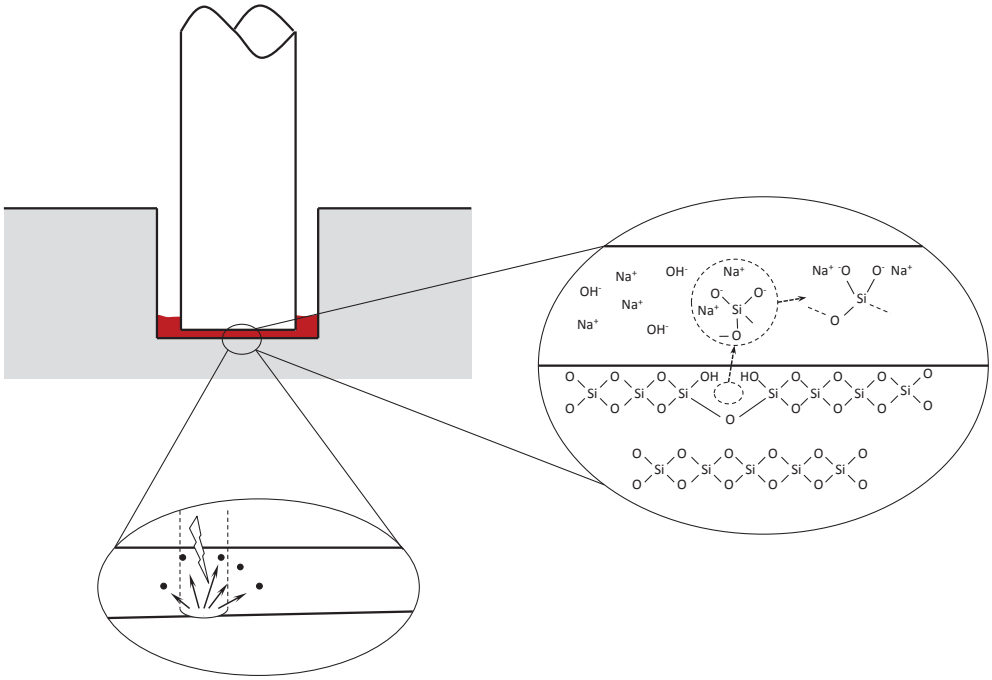

Figure 6.16: Schematic of the machining mechanism which is a combination of thermal assisted etching (breaking the Si-O-Si bonds) and physical bombardment of the surface by discharge channels.

6.4.1 Thermal assisted etching

The OH radicals are known to attack the glass surface thus breaking the Si-O-Si bond. Based on Section 6.1 and Chapter 5 machining can exist in different modes depending on the state of the local electrolyte (aqueous or molten salt) which is determined by the ability to flush the machining zone (hole depth) as follows:

- For high depths the tool is in frequent contact with the glass surface where the electrolyte may be in a molten or aqueous state. For limited flushing, the electrolyte is in a molten state where the glass temperature is higher than the electrolyte salt melting temperature (318 °C for NaOH and 406 °C for KOH). In this case the tool may contact the glass surface (Figure 6.17a) if the machining rate is lower than the tool feed-rate,

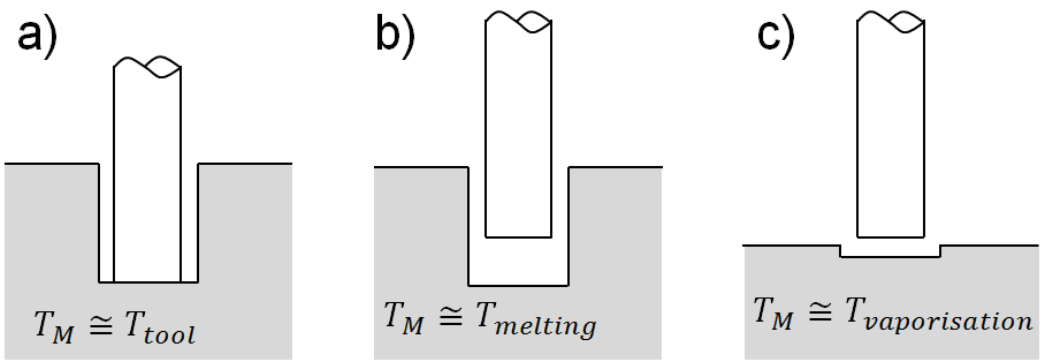

Figure 6.17: Schematic of the drilling configurations for three cases relevant to SACE machining: a) for high machining depth, the tool contacts the glass frequently where the machining temperature is similar to that of the tool ($T_M = T_{tool}$), b) when a machining gap is formed during drilling the machining temperature is similar to the electrolyte salt melting temperature ($T_M = T_{melting}$), and c) for shallow structures the machining temperature is similar to the electrolyte vaporisation temperature ($T_M = T_{vaporisation}$).

similar to gravity-feed drilling where the machining temperature reaches that of the tool ($T_M = T_{tool}$). If the machining rate is higher than the tool feed-rate a gap forms between the tool and the machined surface where the machining temperature may reach the electrolyte salt melting temperature in this case ($T_M = T_{melting}$) a shown in Figure 6.17b. This is apparent in Chapter 5 where the measured gap matches with that estimated from the developed thermal model. The last is based on the idea that the gap remains growing up to a limit where the surface temperature is similar to the electrolyte salt melting temperature. For enhanced flushing, the electrolyte may also be in an aqueous form while the machining gap is being formed.

- When flushing does not limit the machining process, especially on the work-piece surface (depths smaller than 100 μm) the electrolyte in the machining zone is in aqueous form but highly concentrated. Etching can occur in this case where the machining temperature is similar to the electrolyte vaporisation temperature ($T_M = T_{vaporisation}$) as shown in Figure 6.17c where $T_{vaporisation}$ is between 100 and 200 °C for KOH and NaOH depending on the electrolyte concentration. This explains the machining temperature of 185 °C estimated in Section 6.1 by finding the temperature isotherm, based on the developed heat transfer model, that has a size matching with that of the machined surfaces. In this case, flushing was not limiting machining (shallow structures, depth less than 100 μm). A high energy is transferred from the tool to the machining zone where significant part of it is dissipated due to the enhanced flushing. In fact, this is apparent from the simulations which showed that the glass surface temperature

reaches 450 °C, when not considering the effect of convective flow (flushing). The high energy transferred from the tool and the non-limited flushing cause the electrolyte to be in aqueous state where it reaches the maximum vaporization temperature just below its solidification temperature (electrolyte solidifies starting from 200 °C and stays in a solid state up to the electrolyte salt melting temperature). This is not surprising as it is physically impossible to have solid electrolyte salt locally for shallow structures where flushing is not limited.

Whenever the local temperature is low enough (between vaporisation and electrolyte salt melting temperature) to allow electrolyte to solidify, machining is hindered. This may be caused by accumulation of gas bubbles and of machined material beneath the tool which act as thermal resistors hence decreasing heat transfer to the glass. Another phenomena that can stop machining during a certain time is the tool-glass bonding as shown in Chapter 4 (Section 4.4).

Based on these results, it can be concluded that for low hole depth where machining is not limited by flushing, machining temperature is similar to the electrolyte vaporisation temperature. For high depths, machining temperature is similar to that of the tool or is around the electrolyte salt melting temperature, depending on whether a machining gap is formed or not. This explains the high drilling time obtained when adding tool rotation and specifically for high rotational speeds where drilling is expected to be in the second mode in this case. When tool rotation is not added, machining is expected to happen often in the first mode. For high depth, as the flushing is most of the times limited, it is expected that machining gets interrupted due to the accumulation of machined material and bubbles, acting as thermal resistors, beneath the tool hence decreasing heat transfer to the glass. It may be also possible that the electrolyte molten salt solidifies or a tool-glass bonding is formed as the temperature drops.

Therefore, during gravity-feed drilling due to the tool-glass continuous contact machining must be in the first mode. This is in agreement with the results in (Jalali et al., 2009) which predicted that glass temperature can reach 600 °C which is similar to the tool temperature. Similar to constant-velocity feed, for high depths at which flushing is more limited electrolyte can be solidified beneath the tool or a tool-glass bond may form. This results in hindering machining where etching becomes negligible (hydrodynamic regime) and high drilling result. The stair-case evolution for gravity-feed is caused by switching from the first machining mode to non-machining caused by tool-glass bond or local material solidification during a short time after which machining progresses normally (once the machined material is evacuated or the bond is released). The switching back and forth between machining and non-machining causes the stair-case evolution of the hole depth versus drilling time plots in gravity-feed.

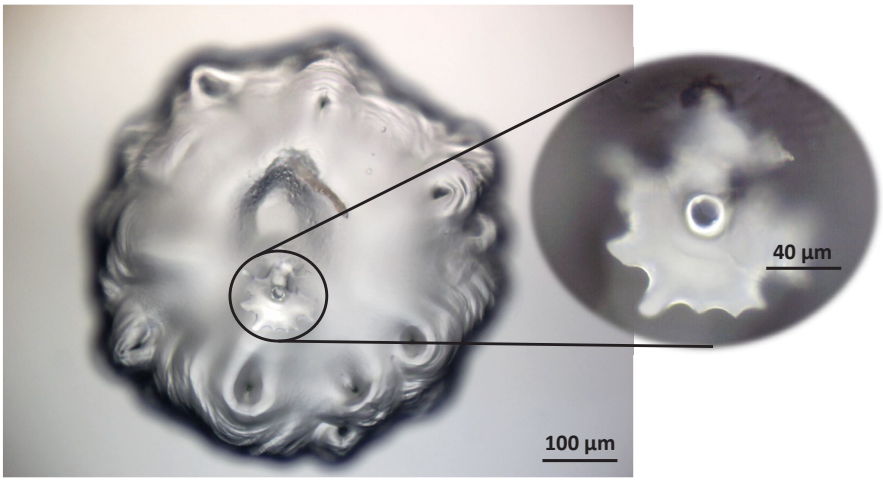

Figure 6.18: A crater with solidified material around it that have different optical properties.

6.4.2 Physical bombardment with discharge channels

When machining is done under extreme conditions causing high local temperature, crater-like structures are observed on the surface (Figure 6.11). These craters must be the result of bombardment of the surface with electrolyte hot jets resulting from the high-energy discharges generation. These jets are called in this text *discharge channels*. The glass surface area stroked with the discharge channels may become less viscous where it gets sublimated. Since the product of the etching reaction is sodium silicate, which is a glass forming melt, it is expected that glass is chemically reformed on the surface during the machining process. Hence, glass may be redeposited on the surface either thermally (hot discharge channel impact) or chemically (sodium silicate solidification).

Figure 6.18 shows an image of a hole bottom surface where material of different optical properties than those of the machined glass is scattered around a crater. This material is most likely formed due to the bombardment of the glass with a discharge channel which forms a cavity on the surface. The process leading to formation of this material may be either thermal (reducing the glass surface layer viscosity and its sublimation) or chemical (solidification of sodium silicate) or a combination of both.

6.4.3 Glass surface layer: Can it be softened?

Chapter 5 showed that when machining is stopped while the tool contacts the glass surface, the tool and the glass are bonded together (indicated by the occurrence of negative forces where the tool is pulled towards the glass as shown in Figure 6.19). For a high contact force, a smooth machined surface is obtained (Figure 6.19). Smoothing of the surface must

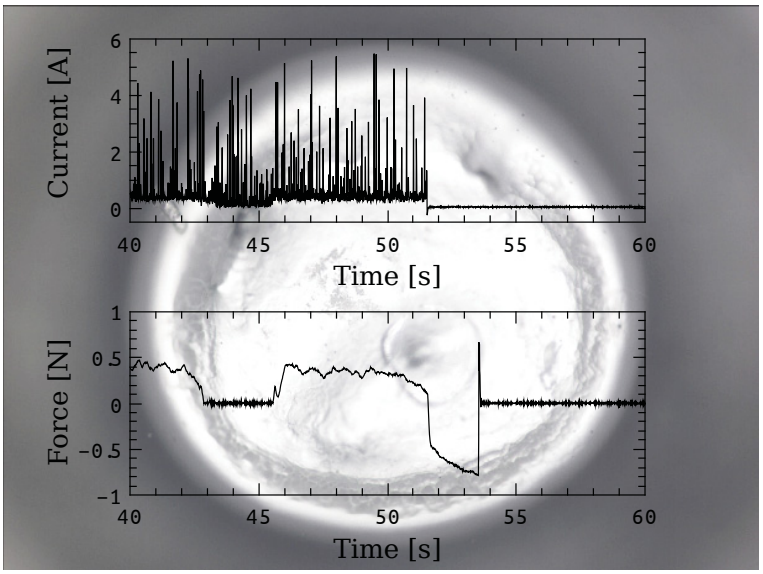

Figure 6.19: An example of a flat bottom surface of a hole drilled in 30 wt% NaOH solution while applying 33 V and for a tool feed-rate of 10 μm/s. In this case a negative force signal is measured, indicating tool-glass surface bond.

be caused by uniform etching as the heat source is brought in contact with the glass. The same effect is seen while measuring the machining gap in Chapter 5 during which a tool-glass mechanical contact was established after a certain cooling time following machining. The inspection of the machined surface after performing these measurements revealed no surface deformation where the resulting surfaces were similar for all cooling times. Only a slight difference exists between low and high cooling times, where surface bubble-like structures and non-uniformities existing for high cooling times were smoothed out for lower cooling time. This smoothing is explained by further surface etching by the hot electrolyte.

The idea that the surface is softened and mechanically deformed upon pressing the tool against it, is directly eliminated as the local heat cannot reach a temperature higher than that provided by the tool, which is shown to reach around 600 °C (Section 3.3.2). This temperature is not sufficient to cause a softened or a viscous glass layer as claimed by (Jain et al., 1999; Fascio et al., 2004; Jalali et al., 2009). In fact, the term *glass melting* used by several authors in the SACE machining field is a wrong one since glass does not melt. Another supporting proof that the local temperature does not reach the glass softening or melting temperature, is the difficulty in mechanically incorporating alumina particles into the glass surface layer. These particles (1 and 3 μm average size) are initially added to the electrolyte (alumina is chosen as it cannot be machined by SACE) and the tool is made to press on the glass surface while machining to mechanically press the particles inside the surface layer. Only some traces of particles of alumina particles could be seen on the

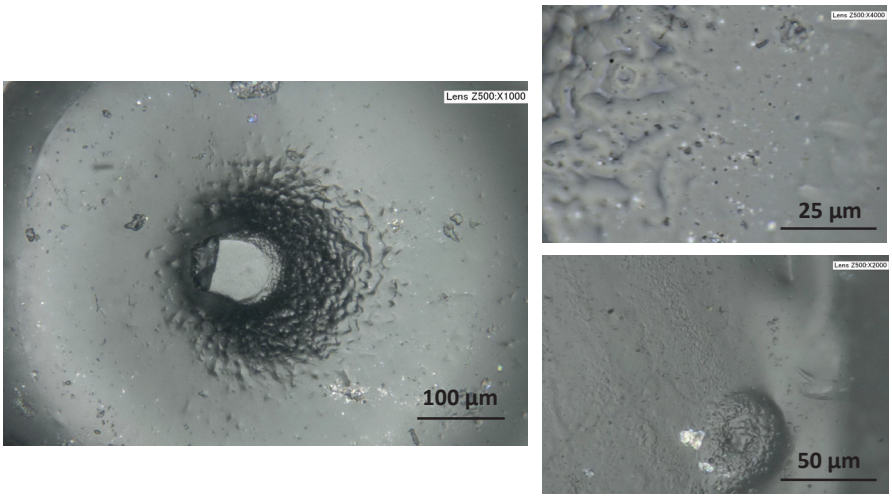

Figure 6.20: Incorporated alumina particles (1 and 3 μm-sized) in the machined surface layer.

machined surface (Figure 6.20). This indicates further the non-existence of a softened layer, as more particles must be pressed into the surface if this layer exists. The incorporation of some particles into the surface is due to bonding them to the surface in a similar way as the tool is bonded to the glass (Section 4.4).

All these arguments show that the glass surface cannot be thermally softened during machining. However, during the machining process the local machined surface properties may change. Previous studies reported that while 2-D machining the surface of the channel has different hardness and density (Didar et al., 2009) which shows that a modified surface layer exists. However, no deep investigation about the reasons behind this or about the surface layer properties was carried out. Since the product of the etching reaction is sodium silicate which is a glass forming melt, it may be that glass is reformed on the surface during machining. The sodium silicate formed may be the reason of tool-glass bonding (Section 4.4) that is most likely chemical.

6.4.4 Machining mechanism: Concluding remarks

Based on the results of the present work, the machining mechanism is proved to be caused by thermal assisted etching by OH radicals, that break the Si-O-Si bonds, and physical bombardment of the surface with electrolyte hot channels resulting from the high-energy discharges generation. It is also shown that there exist two machining modes during which the machining process differs. These modes are defined based on the local electrolyte state which is determined by the local temperature, that is highly influenced by local flushing.

The electrolyte can be aqueous, up to 200 °C, for non-limited flushing or in a molten salt state, above 300 °C, for limited flushing.

The aqueous or the molten electrolyte fills up the machining gap where the pool of OH radicals etch the glass surface (faster etching for molten electrolyte salt) by breaking the Si-O-Si bonds resulting in detachment of (SiO_3^{2-}) which together with Na^+ form sodium silicate which is a glass forming melt. For limited flushing this product stays in the machining zone where it solidifies on the glass surface, hence reforming glass while machining. This may be responsible for the tool-glass bond formed during machining. Moreover, for limited flushing, due to accumulation of machined material and gas bubbles, the local temperature may drop and the electrolyte may solidify. The formation of tool-glass bond or the solidification of electrolyte hinders machining which may explain the occurrence of forces that stay during a certain time while machining, before being removed. The switch from machining state (first or second mode) to non-machining explains the stair-case evolution of the hole depth versus drilling time plots in gravity-feed drilling. The results also show that the maximal attainable glass temperature can reach the tool temperature (around 600 °C) and therefore the machined surface layer cannot be thermally softened during machining.

6.5 Conclusion

In this chapter it is shown that the machining is due to thermal assisted etching in addition to bombardment of discharge channels with the surface, forming crater-like structures. The glass may be also reformed during the machining process since the etching product is a glass forming melt.

The evolution of the machined surface is caused by the local heat propagation on the glass surface. Matching of the machined surface growth with the calculated temperature isotherms for different machining durations showed that in case of non-limited flushing (low depths), glass temperature is around the electrolyte vaporisation temperature. In this machining mode, the local electrolyte is aqueous. For high machining depths where flushing limits the machining process, the electrolyte is in a molten salt state (above 318 °C). Etching progresses faster in this case and the glass temperature can reach the tool temperature (around 500-600 °C depending on the machining voltage) due to the frequent tool-glass contact. Accumulation of machined material in the machining zone may cause a reduction in local temperature to below the electrolyte salt melting temperature which results in solidifying the molten electrolyte. Both solidification of molten electrolyte and tool-glass bonding hinder the machining progress. Therefore, during drilling machining can be in one of the two modes and may be stopped occasionally due to tool-glass bond and electrolyte solidification.

As for the local surface texture, its origin is identified to be the local flow patterns formed in the tool vicinity. The local flow is caused by gas film dynamics and tool kinetics.

Chapter 7

Enhancing drilling by force feed-back

Twenty years from now you will be more disappointed by the things you did not do than by the ones you did. So throw off the bowlines. Sail away from the safe harbour. Catch the trade winds in your sails. Explore.. Dream.. Discover..
(-Mark Twain)

As pointed out in Chapters 2 and 4, gravity-feed drilling is limited by the depth that can be drilled which is less than 300 μm for 500 μm tool diameter. In this case, tool breakage and hole deformation may result due to the tool continuous contact with the glass surface. Similarly, during constant velocity-feed drilling large unrecoverable forces may result, causing tool bending and surface deformation. Hence, for these strategies the usage of tools smaller than 250 μm in diameter is not possible. In fact, these problems should be eliminated by minimizing the contact between the tool and the glass. Previous research showed that it is not straight forward to find a feed-back signal for this purpose (Wüthrich et al., 2006b). Still, trials were made to enhance drilling, where in gravity-feed drilling the voltage was adjusted based on the drilling progress causing a higher repeatability in drilling time for a given hole depth (Morrison, 2009; Morrison et al., 2008). Further, the force signal was proposed as a feed-back signal (Wüthrich et al., 1999) during constant-velocity-feed drilling where a preliminary algorithm that stops the tool motion in presence of a machining force allowed using high tool feed-rates up to 30 μm/s and drilling through holes (1 mm deep with a 700 μm diameter tool). In this case, no surface cracks on the exit of hole could be observed. This preliminary research about SACE feed-back algorithms showed that tools smaller than 100 μm can be used. Recently, force feedback drilling has been applied to machine smooth holes with 31 μm diameter tools (Cao et al., 2009) where an aspect ratio of

around 1:2 was achieved. However, the potential of the implemented algorithm to fabricate high-aspect-ratio holes was not investigated. In fact, the SACE drilling ability to achieve high-aspect-ratio holes (1:11 for 30 μm tool and 40 V machining voltage) was demonstrated when using constant-velocity-feed drilling while applying very low tool feed-rates (1 μm/s), resulting in long drilling time (Jui et al., 2013). Some methods exist to enhance drilling rate (Chapter 2, Section 2.3.2) which are based on finding the optimal machining conditions by trial and error, but these are specific to machining requirements (such as depth, diameter, etc..). No work has been carried out so far to build and compare performance of various feedback algorithms based on understanding the reasons behind slow drilling, knowing that fast drilling is a requirement for many applications.

Based on Chapter 4, flushing and heating proved to be two important factors for drilling to progress. Further, it is shown that the main problem of limited drilling rate is the unavailability of electrolyte in the machining zone, especially for depths higher than 250 μm. In this chapter, and for the first time in the field of SACE, various force feed-back algorithms are developed based on the knowledge built up about the process. The algorithms' efficiency is compared by examining the resulting machining performance. This is done with the aim to test the potential of force feed-back algorithms on enhancing local flushing while balancing both flushing and heating. The efficiency of the built algorithms is measured in terms of their ability to reduce the drilling time. The long-term goal is drilling high-aspect-ratio holes with good surface finish with tools smaller than 100 μm diameter within few seconds.

7.1 Reducing the electrolyte viscosity

Since the circulation of the electrolyte in the micro-hole plays an important role in enhancing drilling progress, this work explores in a first step the idea of reducing the electrolyte viscosity for speeding up machining. The amount of OH radicals in the electrolytic solution must be kept the same as in case of highly viscous solution so that the etching rate would not differ enormously. This allows comparing the effect of flushing on accelerating the drilling rate. Therefore, drilling is done in 50 wt% KOH solution of molarity around 10 M, similar to that of the commonly used 30 wt% NaOH electrolyte. The solution is chosen such that the viscosity is dramatically lowered compared to the case of the commonly used 30 wt% NaOH electrolyte (5 cP for 50 wt% KOH compared to 15 cP for 30 wt% NaOH at room temperature (OxyChem, 2009, 2000).

As a basic algorithm, the hole is machined at a constant feed-rate. Whenever a force higher than a pre-set threshold is exerted on the tool, the tool motion is stopped until the force completely recovers. In this text this action is called a *counter-action*. Figure 7.1a

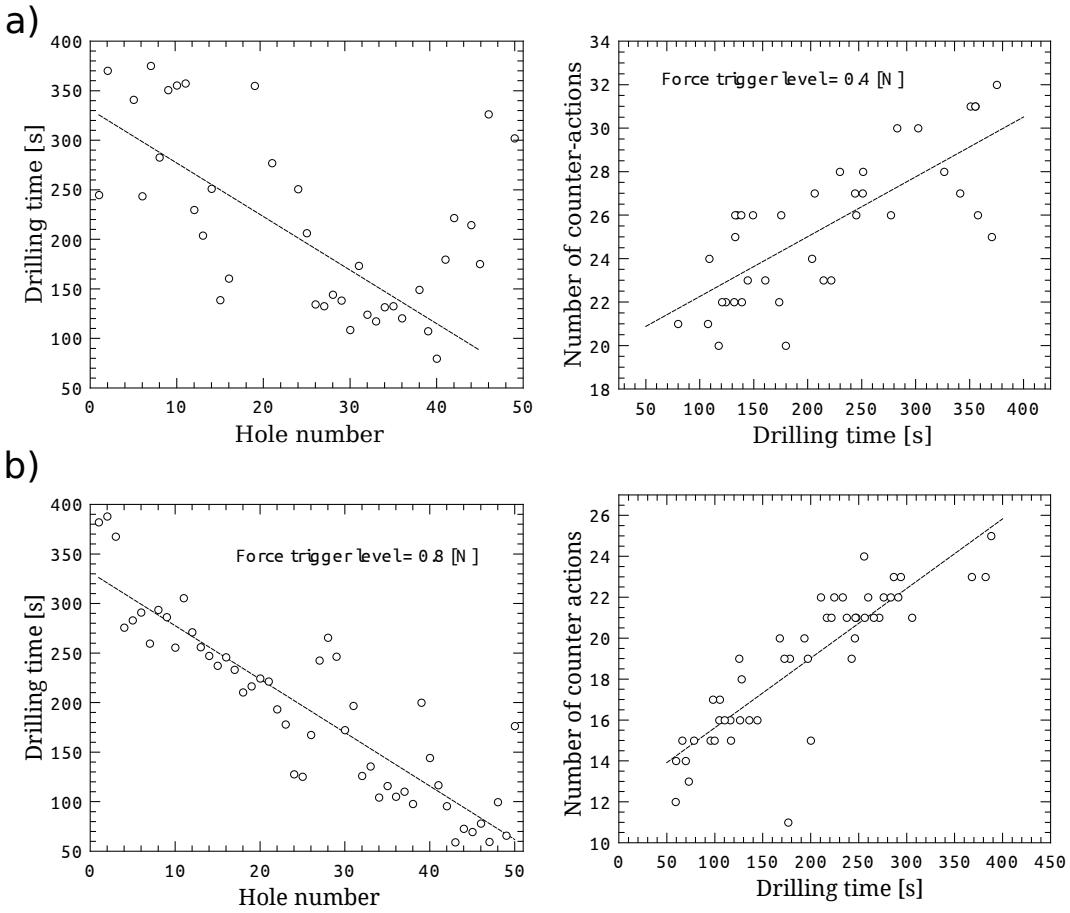

Figure 7.1: Drilling time in function of the hole number and the number of counter actions taken during the drilling duration for an array of holes drilled on a single slide. A counter action, which is stopping the tool motion, is taken when the force exceeds the trigger level of: a) 0.4 N and b) 0.8 N. The tool motion is restored when the force goes back to zero.

shows the drilling time evolution for fifty 400 μm deep holes drilled using 50 wt% KOH while applying low machining voltage. The holes could be drilled in a reasonable amount of time which is not possible to achieve when using the more viscous 30 wt% NaOH electrolyte. This shows that machining using low viscous electrolyte is a good solution for accelerated drilling.

Like for any machining technique, during SACE it is desired to machine while zero forces are exerted on the tool. This is desired to minimize tool bending, hole deformation and work-piece surface damage. While the present feed-back algorithms cannot result in zero-machining forces since they rely on reading a force signal (exerted on the tool), they allow cutting the growth of the force. It is desired to cut these forces while they are still at low amplitude to minimize tool bending and work-piece surface damage. Since the local heat proved to be a key in the machining process (Chapter 4), a high force threshold is also desired because it implies longer contact duration between the tool and the surface, hence more surface heating. Thus, the choice of the force threshold must consider both aspects. Two force thresholds, 0.4 and 0.8 N, are chosen such that to allow low and high pressing force. The effect of machining using both thresholds on the drilling time is investigated. Figure 7.1 shows an example of drilling time for two thresholds: 0.4 and 0.8 N while drilling 400 μm deep holes using 30 V machining voltage. Although for both thresholds the drilling time is similar, the number of counter-actions differed where they are less for the higher force threshold. As hypothesized, this is attributed to the more efficient heating of the work-piece. Indeed, high force threshold implies more heating and less flushing since the tool is more often in contact with the glass surface. Thus, upon lowering the force threshold, less heating and more flushing result.

The importance of local heating on enhancing the machining efficiency can be seen on Figure 7.1b, where the drilling time deceases as more holes are drilled. This is due to the progressive heating of the electrolyte and the glass work-piece. All this evidence highlights once more that both heating and flushing are important factors for SACE machining. For the rest of the experiments, the low force threshold (0.4 N) is chosen.

7.2 Combining gravity-feed drilling and tool upward motion

During gravity-feed drilling the tool is always in contact with the glass surface. This helps in transferring the heat to the surface and enhances machining where drilling rate reaches 100 μm/s during the first 100 μm (Wüthrich, 2009). However, machining rate is significantly reduced for deep holes since flushing becomes a major problem. Knowing the

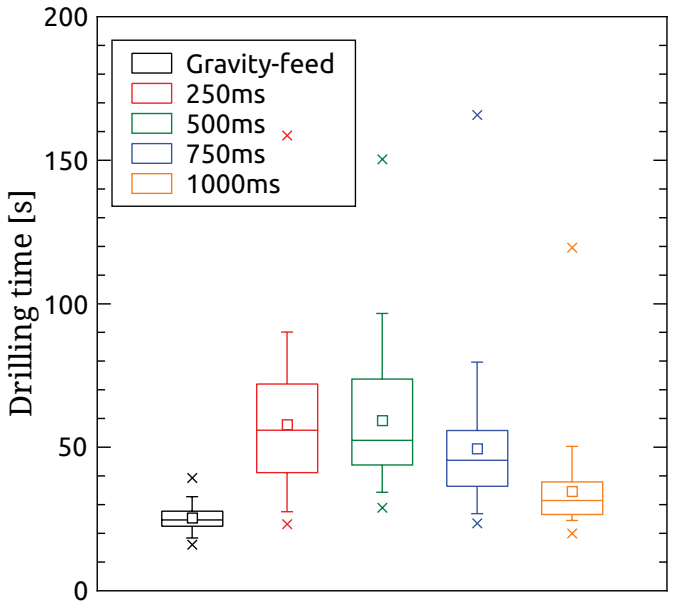

Figure 7.2: Variation of drilling time for holes machined in gravity-feed mode while adding a flushing time ranging between 0 and 1000 ms.

significance of combined heating and flushing on the machining progress, an algorithm that adds flushing to the gravity-feed drilling is developed. To compare the effectiveness of this algorithm to gravity-feed drilling in terms of resulting drilling time, experiments are done in 30 wt% NaOH. This viscous electrolytic solution is chosen because it allows testing the impact of the proposed algorithm on local flushing since, as shown in the previous section, the less viscous electrolyte (50 wt% KOH) facilitates local flushing. Moreover, 30 wt% NaOH is normally used during gravity-feed so using it during the present experiments permits comparing the results with those obtained during gravity-feed drilling.

It was shown in gravity-feed drilling that for depths higher than 200 μm drilling enters the hydrodynamic regime where flushing becomes problematic (Jalali et al., 2009). Hence, 250 μm deep holes are drilled to test the effect of the algorithm on enhancing flushing. Drilling is done while applying 30 V and moving the tool towards the surface at constant feed-rate of 50 μm/s. When a force higher than 0.4 N is detected, the tool is pushed towards the glass surface, as in gravity-feed mode, to heat up the surface. Since in this case the tool is always in contact with the surface, the force sensor mode of the machining head was used repeatedly during a short defined time interval to check if the force recovered. Investigated time intervals denoted by *probing time* ranged from 250 ms to 1000 ms. When the force recovers the tool is moved 10 μm away from the surface to allow flushing the machining zone. Drilling then proceeds while moving the tool at the pre-set feed-rate. Figure 7.2 compares the application of this algorithm for 50 drilled holes. Results show that with increased probing time the

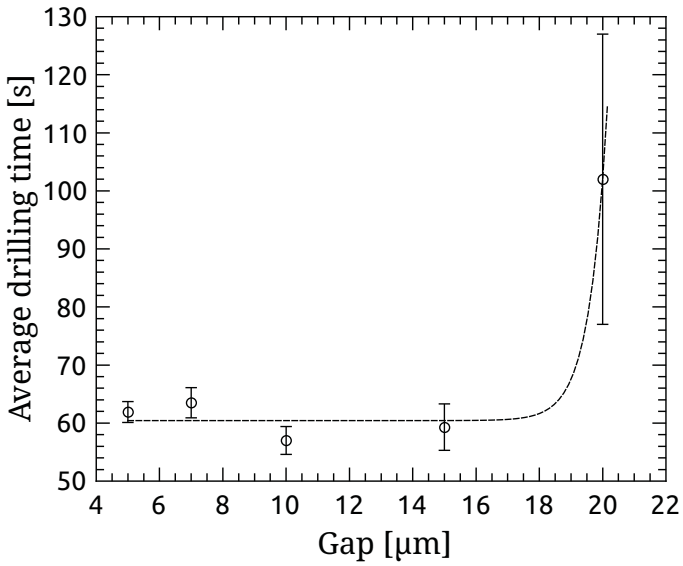

Figure 7.3: Average drilling time in function of the tool-work piece gap for 250 μm deep holes drilled in 30 wt% NaOH for 50 μm/s feed-rate and 30 V machining voltage. The gap is created whenever a force threshold of 0.4 N is exceeded.

performance of the algorithm becomes more similar to gravity-feed drilling. This is due to the fact that, for high probing times, drilling remains in the gravity-feed mode most of the time. Figure 7.2 also shows that gravity-feed drilling is faster than the used algorithm where, unexpectedly, the addition of the 10 μm gap does not speed up the drilling.

7.3 Adding a tool-work piece gap

Based on the previous algorithm, a more detailed investigation on the influence of maintaining a specific tool-work piece gap on flushing the machining zone is done. Holes, 250 μm deep, are drilled while moving the tool at a constant feed-rate of 50 μm/s. Machining is done using 30 wt% NaOH and 30 V machining voltage. Whenever a force higher than 0.4 N is exerted on the tool, the last is moved upwards (away from the surface) until the force is recovered. In this case, the tool will just slightly contact the hole's bottom surface. A further upwards motion follows to keep a defined gap between the tool and the surface. The investigated gap ranged from 5 to 20 μm.

Figure 7.3 shows the resulting drilling time for the investigated gaps where 50 holes are machined for each condition. For gaps smaller than 15 μm, the drilling time remains essentially the same but increases dramatically when the gap exceeds 20 μm. This shows that, creating a gap between the hole and the tool each time a machining force appears, is not sufficient to accelerate drilling. On the contrary, this may cause heat dissipation, hence

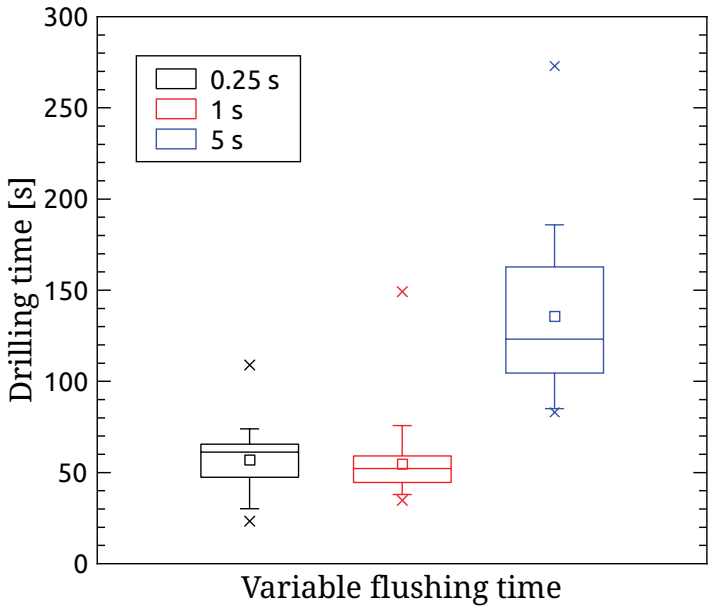

Figure 7.4: Drilling time for variable flushing time ranging from 0.25 to 5 s. Whenever a force exceeds 0.4 N the tool is moved upwards by 10 μm and a waiting time, called flushing time, is added.

decreasing the etching rate. These results are in agreement with the knowledge acquired in Chapter 6 (Section 6.2.4) where moving the tool away from the glass surface causes the heat to be concentrated on a narrower area on the glass surface beneath the tool. Therefore, the machined surface area in this case is smaller than the bottom surface area of the tool (Figure 6.7). Thus, when feeding the tool again towards the surface it will contact the non-etched circular edge.

Based on these results, creating a small gap can help in flushing but, by itself, it does not accelerate drilling. Further a gap higher than 20 μm causes non-uniformly etched surface and a cooled down machining zone.

7.4 Adding a flushing interval

Since a large gap slows down machining, a 10 μm gap is chosen to be used for the rest of the algorithms. The next element to investigate is the influence of adding a waiting time, once the gap is established, on the flushing. As for the previous algorithm, 250 μm deep holes are machined using 30 wt% NaOH and 30 V machining voltage. The same algorithm as the last one is done while a defined waiting time (called flushing time in this text) is added once a gap of 10 μm is established, before drilling further. The flushing time is varied between 0.25 and 5 seconds. Figure 7.4 compares the results of the various flushing times considered. Similar drilling times are observed for flushing times up to 1 s. The result is similar to that

obtained with the previous algorithm (for the same gap of 10 μm). However, the frequency of execution of the algorithm (re-establishing the gap and waiting) is reduced with increased flushing time, as long as the last is less than 1 s. This shows that adding a flushing time after creating a gap between the glass surface and the tool enhances drilling. However, a long waiting time is not constructive since it slows down the machining and may result in decreasing the surface temperature.

7.5 Increasing the local turbulence

Since the drilling time resulting from the previous two algorithms (keeping a tool-surface gap in the presence or absence of a waiting time) is similar, a more complex algorithm has to be developed to enhance the flushing. The present algorithm is built based on the idea of taking advantage of the gas film dynamics to enhance the local flow. It is known that, when the gas film breaks, a strong jet of bubbles is generated below the tool (Ghorbani, 2012). This jet can potentially be used to enhance the local flow inside the hole in order to evacuate the machined material more efficiently. Based on this concept, the following experiment is done while keeping the same machining conditions as before (250 μm depth, 30 wt% NaOH, 30 V). As for the previous algorithm, whenever a machining force appears, the tool is moved upwards to remove the force and a gap of 10 μm is established. The voltage is then switched off for 20 ms and on again to force a jet to form in order to allow local flushing. To induce a stronger flow, a higher voltage pulse, 34 V, which is 50 ms long is applied to compare it to the case of the lower amplitude pulse, 30 V.

Figure 7.5 compares the drilling time of 50 successively machined holes for the cases where no pulse, an off-pulse of 20 ms and an on-pulse of 34 V amplitude and 50 ms duration are applied. Adding an off-pulse improves the drilling time compared to the case where no pulse is applied. On the other hand, a high voltage pulse causes an increase in the drilling time compared to the off-pulse. This can be explained by the fact that for the higher pulse more material is evacuated from the machining zone due to the stronger jet created. This material includes the hot electrolyte. In this case, cold electrolyte is brought into the machining zone more frequently resulting in cooling of the glass surface and increasing the drilling time. For this algorithm, the minimal drilling time is similar to that achieved using the previous algorithm. Therefore, more sophisticated algorithms are needed to enhance machining.

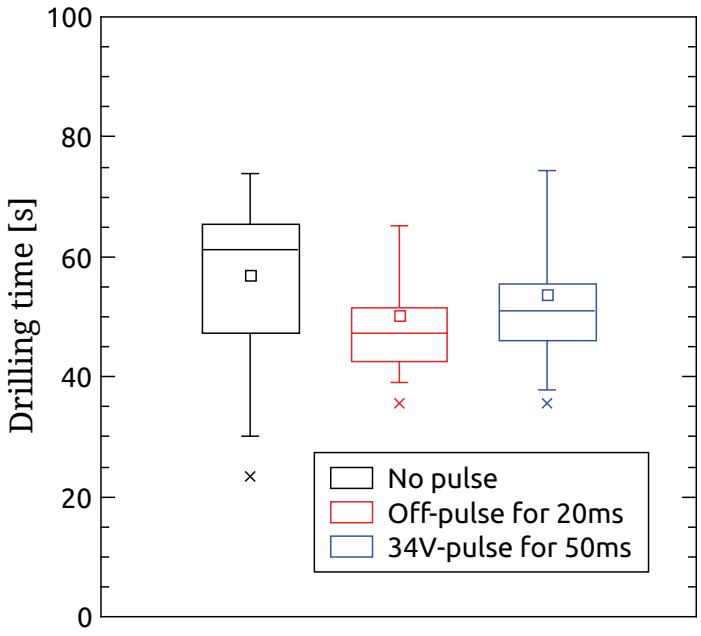

Figure 7.5: Drilling time when varying the local turbulence through varying the voltage duty cycle and amplitude.

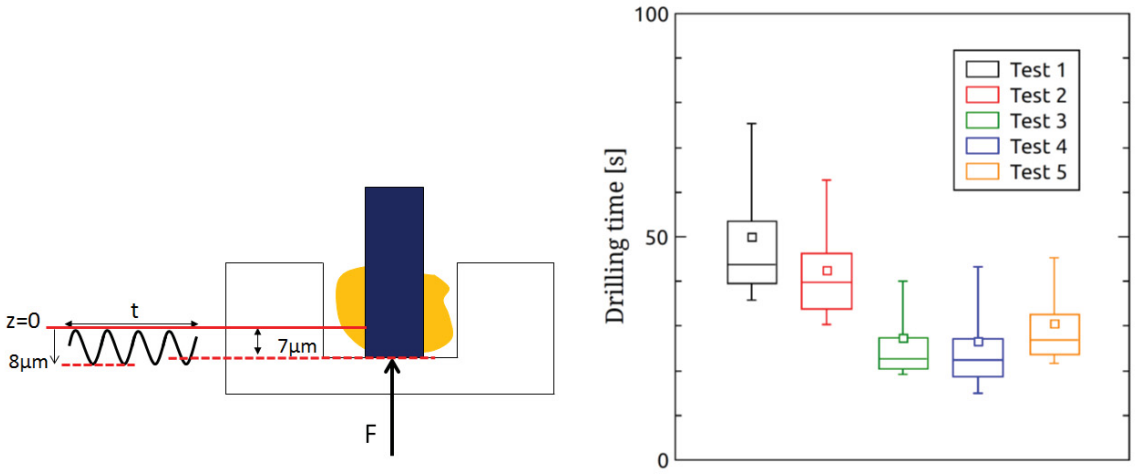

Figure 7.6: a) Schematic of the algorithm that applies vibrations to the tool after moving it upwards by 7 μm as soon as the force exceeds the pre-set threshold. The vibrations are 8 μm in amplitude (applied in the downward direction) and of different duration and frequency. b) The drilling time for the different applied vibrations. For Tests 1 and 2 slow vibrations are applied during 1 s and 0.2 s respectively when 0.8 N is exceeded. For Tests 3, 4 and 5 quick vibrations are applied during 0.2 s when the force exceeds 0.8 N, 0.4 N and 0.2 N respectively.

7.6 Adding tool vibrations

In order to force local flushing while maintaining the surface heat, vibrations are superposed on the tool vertical motion. After the force is recovered, the tool is moved upwards by 7 μm and then sinusoidal vibrations of 8 μm in amplitude are applied in the downward direction. Note that in this configuration, the tool will, in each vibration, shortly contact the work-piece hence maintaining the surface heat. Different vibration durations are investigated as shown in Figure 7.6. First, ten successive vibrations lasting for 1 s, are used following the detection of a force exceeding 0.8 N (Test 1). Decreasing the number of vibrations to two (lasting for 0.2 s) results in a shorter drilling time (Test 2). This shows that even a short duration of vibrations enhances the local flushing. Quicker vibrations are also applied to examine their effect on flushing. In Test 3, ten vibrations are applied during 0.2 s. Drilling time is reduced even more reduced. Since in both Tests 2 and 3 the vibration time is the same but the drilling time is reduced for Test 3, it is concluded that quicker vibrations remove the material from the machining zone more efficiently. This statement is further validated when comparing Test 1 (10 vibrations during 1 s) and Test 3 (10 vibrations during 0.2 s) which result in the same average number of counter-actions (around 20) over the drilling duration. This shows that quicker vibrations are more efficient since they result in faster drilling. Note that for Test 1, twenty counter actions will take at least 20 s, which represents the time gain between Test 1 and 3. To further improve the drilling time, two additional tests are done while varying the force threshold. The thresholds are chosen to be 0.4 N and 0.2 N for Tests 4 and 5 respectively. The drilling time is slightly reduced for Test 4 whereas it increases for Test 5. This is due to the fact that for Test 5 heating the machining zone becomes less efficient compared to the case when a higher force threshold is used (as discussed in the first group of algorithms).

7.7 Adding tool rotation and vibration

The next step is to investigate if the last developed strategy (recover the gap whenever the tool touches the work-piece followed by quick vibrations for a short time) can enhance constant-velocity feed drilling when rotation is added and low viscous electrolyte is used. To test the efficiency of the algorithm, the machined depth is chosen to be 500 μm which is twice the depth at which the hydrodynamic regime starts. The holes are machined using 50 wt% KOH and 30 V machining voltage. Figure 7.7 compares the drilling time for the case where only rotation is applied (rotational speed around 1000 rpm) and when both rotation and vibrations are used. In both cases, the same force threshold (0.4 N) is used and a gap

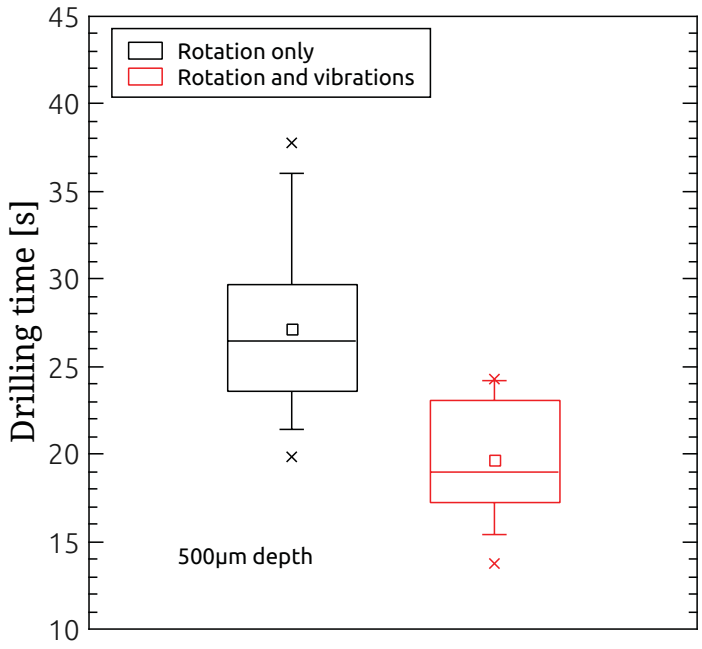

Figure 7.7: The influence of adding only tool rotation (1000 rpm) and combined rotation (1000 rpm) and vibration (10 vibrations during 0.2 s) on the drilling time. For both cases, the tool motion is added when the force exceeds 0.4 N where a gap of 7 μm is created and tool motion is added afterwards.

of 7 μm is recreated. As shown in figure 7.7, adding tool vibrations reduces the drilling time to 20 s in average compared to an average value of 27 s when just tool rotation is applied.

7.8 Combining the knowledge from the present algorithms

In a last step, the knowledge acquired from doing the various algorithms is combined in order to drill high-aspect-ratio micro-holes during a short time. For these experiments a low viscosity electrolyte (50 wt% KOH) and a small tool (100 μm diameter tungsten carbide micro-drill bit) are used for drilling 900 μm deep micro-holes. The algorithm uses a force threshold of 0.4 N and recreates a gap of 7 μm followed by ten vibrations during 200 ms whenever the threshold is exceeded. Tool rotation, 1000 rpm rotational speed, is also added.

Figure 7.8 shows the achieved drilling time for various tool feed-rates. Results show that high aspect-ratio-holes (1:9) are drilled during few seconds. For the present algorithm, the shortest drilling time resulted for a tool feed-rate of 70 μm/s which is around 12 s since these conditions ensured the best balance between local heating and flushing. Compared

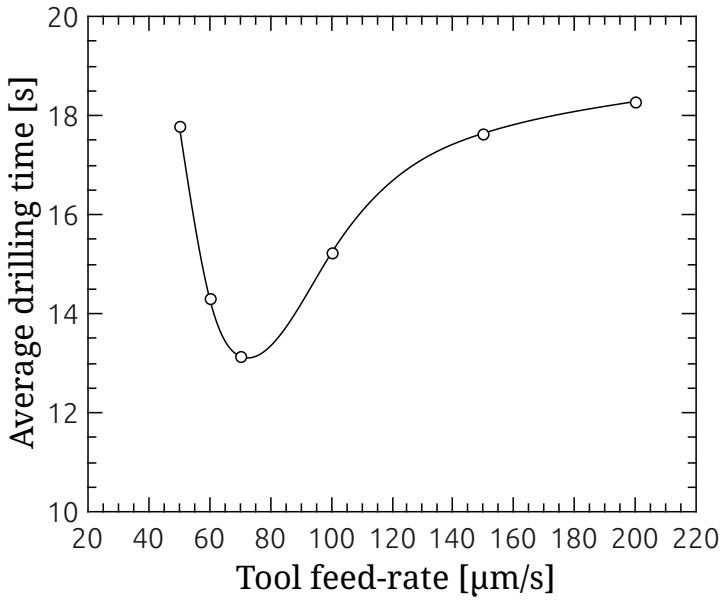

Figure 7.8: Average drilling time in function of the tool feed-rate for holes drilled in 50 wt% KOH using 100 μm drill bits while applying 30 V. Deep holes (100 μm, 1:9 aspect-ratio) could be drilled during 13 s.

to this result, drilling time achieved with gravity-feed is much larger where it can take several minutes to drill such deep holes, if even possible (most often the tool breaks or the glass work-piece cracks). Using constant-velocity-feed drilling, such depths are impossible to attain (tool will break).

7.9 Conclusion

Previous chapters showed that balancing both local heating and flushing is a key in efficient machining evolution. In this chapter, various force feed-back algorithms are built based on this idea and their influence on the drilling progress is investigated by considering the resulting drilling time. As flushing limits machining progress for depths typically higher than 200 μm, different ways to enhance local flushing based on developing force feed-back algorithms were investigated. Results showed that maintaining a gap between the tool and the glass surface is counter-productive since it causes a less heated surface and a non-uniform etching beneath the tool. Adding various tool motions (high frequency vibrations, rotation) proved to enhance flushing. In fact, the idea of developing algorithms that use tool vibration to enhance drilling seems promising as a balance between local flushing and heating could be established when adding tool vibration. By combining tool rotation and vibration while using a less viscous electrolyte, high-aspect-ratio holes (1:9) could be drilled during few seconds.

This result was not possible to achieve using the conventional SACE drilling modes, where in case the tool or the substrate do not break, drilling can last for several minutes before reaching this depth. The present results provide a preliminary study about the potential of SACE force feed-back drilling on enhancing drilling performance (reducing drilling time) by balancing both local heating and flushing.

Chapter 8

Conclusions

Fear is a poison for which you have an antidote, but you don't know it yet. The antidote is knowing how strong you are, how much you can handle, how you bend; but do not break no matter how difficult the things around you become.
(-Kitty Kolding)

Spark assisted chemical engraving (SACE) micro-machining is a complex machining process where the knowledge about it is limited up to the present day. Although the fundamentals about the electrochemical process and discharge generation are explored up to an advanced level, the phenomenon of glass micro-machining is still vague and fuzzy. In fact, no research has been devoted to understand the mechanism behind machining, the variables in the machining zone and the reasons that hinder the machining performance. Finding the appropriate machining conditions that can result in a good surface finish for a certain drilling depth is based on trial and error. Up to the current date, the drilling process is still blind and no feedback signal is available to monitor the drilling progress.

In the present thesis work the force exerted on the tool-electrode during SACE micro-machining is proposed as a monitoring signal. A methodology that relies on this signal is developed to quantify measurement errors and to measure the machining zone parameters. Based on characterizing the machining forces, local heating and flushing are identified to be the drilling limiting factors. Using this knowledge, a dimensionless curve is constructed that allows choosing the machining parameters in function of the required hole depth such that drilling can be done with minimal forces. The force signal also allowed discovering the existence of a tool-glass bonding phenomena during machining. The bond was explained as a physical or chemical bond, where this requires further investigation. In this work,

the machining temperature was found to differ depending on the machining geometry and configuration. In fact, this temperature depends on the electrolyte state, i.e. aqueous or molten, which is directly related to how well the local flushing is. The reduced material removal rate during the machining process was explained to be caused by local accumulation of machined material and gas bubbles beneath the tool. Further, as a tool-glass bonding may form during machining this can also hinder machining progress. Based on the knowledge acquired throughout this work, the machining mechanism and the origin of the machined surface layer texture are identified. The potential of improving the drilling performance based on the developed knowledge is investigated by implementing preliminary force feedback algorithms which allowed increasing the aspect-ratio five times while decreasing drilling time by a factor of six compared to the conventional SACE machining.

8.1 Highlights

The key contributions of this work are summarized in the following:

1. The tool-glass surface contact force is suggested as a monitoring signal for SACE machining. This approach is done for the first time in the SACE field. Based on the analysis and characterization of the machining forces, the machining limiting factors are identified to be the local surface heating and flushing. Considering these limiting factors, a dimensionless curve that predicts the depth at which forces occur is constructed. This curve allows appropriate choice of machining conditions such that for any desired hole depth drilling can be done with zero contact forces which avoids forming deteriorated machined surfaces.

2. A methodology is developed to quantify the measurement errors and the machining zone parameters based on the force signal. The errors resulting from tool wear, bending and thermal expansion are identified experimentally. Further, the machining gap formed between the tool and the glass surface for deep holes (above $100\,\mu$m) during constant-velocity-feed drilling is measured for different machining conditions. Both the tool expansion and the gap evolution are predicted based on a developed thermal model. The model predicts the tool temperature in function of the machining conditions. As the heat is transferred from the tool to glass surface, material removal rate is enhanced and a tool-glass surface gap results. The model predicts that the maximal gap is established when the machining zone temperature drops below the electrolyte salt melting point. This gap is directly related to the machining progress as the last must depend on the trade-off between a small enough gap that allows efficient heat

transfer to the glass and a large enough gap that allows properly forming the gas film and freeing the bubbles (thermal resistors) from beneath the tool.

3. The machining mechanism is proved to be the result of physical bombardment of the surface with high-energy discharge channels and of thermal assisted etching by OH radicals, that break the Si-O-Si bonds. It is also shown that there exist two machining modes during which the electrolyte appears either in aqueous or molten salt state. The occurrence of machining in one mode rather than the other is determined the ability to flush the hole.

    - Physical bombardment of the surface with discharge channels causes high glass local temperature. This causes crater-like structures to be formed on the surface especially at high voltages as the discharge activity is more intense. A layer of optical properties different than those of the glass could be seen in the vicinity of the crater. This layer may be due to sublimation of softened glass or to solidified sodium silicate, which is the product of the etching reaction and a glass forming melt. Therefore, glass may be reformed on the surface during machining.
    - Mode 1: For low hole depths during which no contact forces between the tool and the glass surface occur (less than 100 μm based on Chapter 4) electrolyte is in aqueous state due to enhanced flushing. The thermal assisted etching is realized through the growth of the surface in the radial direction from an etched ring having the same diameter as that of the tool to a completely etched hole during less than 1 s. The growth of the machined surface is simulated in ANSYS based on a developed heat transfer model where matching it with the experimental results showed that machining does not occur below a temperature of around 185 °C. This temperature is around the vaporisation temperature of the electrolyte.
    - Mode 2: For high depths, where flushing is limited, electrolyte is mostly in a molten salt state but can be also in aqueous state for periods of enhanced flushing during machining. Therefore, machining progresses while the tool contacts the surface (like in gravity-feed drilling) or while there is a machining gap which depends on how well flushing is.
    - The machining is interrupted when the electrolyte solidifies (temperature between 200 and 300 °C). The solidification of electrolyte, can be due to inappropriate flushing especially for small machining gap where the machined material and bubbles accumulate beneath the tool, acting as thermal resistors (reduce heat transfer to the glass). Based on these explanations, the stair-case evolution of

hole depth versus drilling time is most likely caused by the switching between the second machining mode and interrupted machining.

- It is shown that the tool and the glass surface may sometimes bond together during a short time while machining. This is witnessed by the measured negative forces indicating that the tool is pulled towards the glass surface. This bond is most likely chemical. The present finding demonstrates the potential to use the force signal in order to control the machined surface texture.

4. The origin of the machined surface texture is proved to be the local flow of hot electrolyte in the machining gap. It was found that for narrow gap the local electrolyte flow patterns are imprinted on the surface and they are less pronounced as the gap is larger.

5. The feasibility of using force feedback algorithms to enhance the drilling performance is deeply investigated for the first time in the field of SACE. Several algorithms, built based on the idea of balancing both local heating and flushing, succeeded in increasing the hole aspect-ratio by a factor of 5 compared to the state-of-the-art SACE drilling and allowed using tools 7 times smaller than the normally used ones (70 μm diameter). Further, the resulting drilling time is dramatically reduced to few seconds compared to several minutes in the state-of-the-art SACE drilling.

8.2 SACE: from the laboratory to industry

The developed knowledge about the SACE drilling process is transferred to a company, Posalux SA that placed this year the first machine operated by this technology on the market (Figure 8.1). The designed machine is user-friendly as it is programmed to perform drilling operations, based on the knowledge we transferred about the process, with minimal user interference. Further, it incorporates all the various elements that allow high-quality and efficient drilling including high accuracy positioning stages, controllable electrolyte circulation system, a multiple degree of freedom machining head allowing tool translation and rotation (range of defined speeds and eccentricities). The machining head can hold tools as small as 100 μm diameter and has a clamping system that allows continuously feeding the tool during machining to compensate for any errors resulting from tool wear. The moving part of the machining head is so light, ensuring negligible tool bending, and has almost zero damping (frictionless air bearing used). As a first step, the preliminary force-feedback algorithms developed in this work were successfully implemented on Posalux machine which allowed drilling 1:10 aspect-ratio-holes and 100 μm in diameter with minimal surface damage and

Figure 8.1: The SACE machine placed this year by Posalux,SA on the market. Photo taken from Posalux SA website (Posalux).

high repeatability and accuracy. More complex algorithms are being currently built and tested for drilling optimization.

The SACE machine has so far been demanded for several applications, the most common ones being fabrication of through vias for electrical circuits, optical wave-guides and interconnects for photonics applications, grooves and large wall thickness holes for micro-fluidic devices, and micro-structures for watch industry applications.

8.3 Outlook

8.3.1 Controlling the surface texture

The present work showed that the texture is determined by the flow of hot electrolyte in the machining gap. For small enough gap, the electrolyte flow patters in the tool vicinity get imprinted on the surface. By changing the electrolyte properties and the tool geometry and by imposing tool motion, different electrolyte flow patterns can be produced. More investigation is required to know the minimal gap needed to imprint the local flow patterns on the surface. Control algorithms can be built based on this knowledge to control the resulting surface texture.

8.3.2 Investigating the type of tool-glass surface bonding

Chapter 4 shows that the glass and the tool could be bonded together during a short interval of time. This is witnessed by the appearance of negative forces implying that the tool is pulled towards the glass. It is proved that the tool-glass bond is not created at a fixed tool temperature and that it detaches when the tool is pulled away from the glass by a specific force amplitude. Therefore, the tool detachment is due to exceeding the bond strength where the bond is expected to be either chemical or physical. Further investigation is needed to identify the type of the bond. A possible way to check this is by using tools of different bottom surface roughness. If the tool and the glass are physically bonded, the resulting negative force magnitude is expected to differ when varying the surface roughness (higher force for smoother tool). However, if no difference results, the surfaces are most likely chemically bonded.

8.3.3 Advancing force-feedback algorithms

Preliminary built force feedback algorithms (Chapter 7) showed their potential in enhancing the machining performance. These algorithms can be developed to achieve fast drilling of high-aspect-ratio holes improve the machined surface finish. The dimensionless plot (Figure 4.7) in Chapter 4 show that forces occur at different depths while drilling. A proposed idea is using adaptive control strategies where different actions can be taken based on the drilling depth. For example, for low depths high voltages can be applied to heat up the surface to remove surface forces while for high depths flushing can be enhanced by switching to pulse voltage or by adding tool motion like vibrations or rotation. The range of tool rotational speeds that can enhance flushing while preserving the local temperature must be investigated. It is shown in this work that tool-glass bonding can form during machining which may be responsible for hindering the machining progress. Therefore, one solution would be increasing the voltage or reversing the voltage polarity once drilling rate decreases dramatically.

8.3.4 Detecting glass breakthrough

It is proposed to use the force signal for building algorithms to detect glass breakthrough (for through holes). The purpose is preventing exit cracks from forming and achieving the smallest possible exit diameters (for producing vias and nozzles in glass).

This idea is based on finding in the measured force signal patterns at the moment of glass break-through or close to its occurrence. In order to increase the measurement sensitivity,

it is proposed to analyse the forces based on the force derivative signal. As a further step, small vibrations can be applied to the tool-electrode where the vibrations frequency has to be close to the natural frequency of a glass membrane having a certain thickness t_{surf}. Equation 8.1, which shows the relation between the resonance frequency f_{mn} and t_{surf} for a circular membrane clamped on the edges, can be used as a starting point to approximate the vibrations frequency for a chosen t_{surf}:

$$f_{mn} = \frac{a_{mn}}{2\pi R}\sqrt{\frac{T}{\rho t_{surf}}} \tag{8.1}$$

where f_{mn} is the resonance frequency for vibration mode a_{mn}, T is the tension, ρ is the density, R is the membrane radius and t_{surf} is its thickness.

While drilling, as the glass thickness approaches t_{surf}, a change in the force signal must be detected. The idea is detecting the depth at which glass breakthrough is about to occur. This allows taking actions such that the hole will be opened smoothly where a tiny opening, free of surface cracks, can be produced.

8.3.5 Modifying the machined glass surface

It is shown in Chapter 6 that alumina micro-particles are incorporated into the machined surface layer. Therefore, it is proposed to investigate the possibility of modifying the machined surface in a controlled manner. The modification is suggested to be done either physically or chemically by incorporating micro-particles or network modifiers to the surface layer. For both approaches, two key parameters will have to be controlled: the contact between the tool-electrode and the glass and the local temperature.

Physical incorporation

The particles can be incorporated into the surface by tool-surface mechanical contact. The particles can be added to the electrolytic solution or they can be generated from the tool by sputtering or they can be formed in the machining zone based on electrochemical reduction of precursor ions.

1. Incorporation of alumina micro-particles:

   It is shown in this work that alumina particles, could be incorporated in the surface layer. A deep investigation about incorporating a defined quantity of alumina particles on the surface can be further done. The first step is finding, for each particle size, the appropriate tool-surface gap such that particles would be available inside the machining

zone. Force feedback algorithms can be built to allow particles to be flushed inside the gap and to engrave them inside the surface layer. Alumina particles are particularly chosen because they cannot be machined by SACE and have the same coefficient of thermal expansion as glass which prevents their detachment from the surface after it cools down. Metal particles are not recommended to be used since they may be attracted during machining to the tool by electrical forces.

2. Generation of metal clusters at machining spot:

   - *Mechanical detachment:* Coating the stainless steel tool-electrode with metals (such as Iron, Cobalt, Copper and Silver) allows detaching the corresponding metal particles from the tool by electrochemical discharges during machining. It is proposed to study the thickness of the surface layer, in which the particles are incorporated, in function of two parameters: the coating thickness and the machining gap. While the first determines the amount of particles available in the machining zone, the second affects the amount of particles incorporated into the surface as it influences the local flow and temperature.
   - *Electrochemical reduction by ECD:* Another proposed idea to modify the local glass surface is electrochemically reducing precursor ions into nano-particles. The precursor ions can be supplied by adding salts to the electrolyte. Recent studies showed that the mass of nickel oxide nano-particles synthesized by electrochemical reduction at 30 V during 3 hr in sulphuric acid using 0.5 mm diameter nickel cathode is around 1.1 mg (Allagui, 2011) implying that 1 μg is generated after 10 s. Based on (Combes et al., 2003) iron oxide (Fe_2O_3) and cobalt oxide (CoO) must constitute 1.4-4wt% and 0.02-0.05wt% of the glass composition respectively in order to color it, hence modify it. This implies that for an area of 1 mm^2, less than 1 μg of the metal is enough to color the glass surface. This amount of particles is similar to that generated by electrochemical reduction of precursor ions during 10 s. Therefore, the quantity of generated nano-particles in the machining zone must be sufficient to modify the machined surface layer.

     Using the Pourbaix diagrams the required pH to prevent precipitation can be known. For example, for Cobalt and Iron the pH has to be lower than 9 to avoid precipitation. This issue can be addressed by adjusting the electrolyte pH by adding to it a buffer, such as lactic acid. From the Henderson-Hasselbalch equation, 3.25 mg of lactic acid ($C_3H_6O_3$) should be added in 500 ml solution of 30 wt% NaOH for lowering the pH to 9. Another proposed idea is using pulsed voltage supply where for the high pulse H^+ ions electro-migrate to the tool vicinity, hence

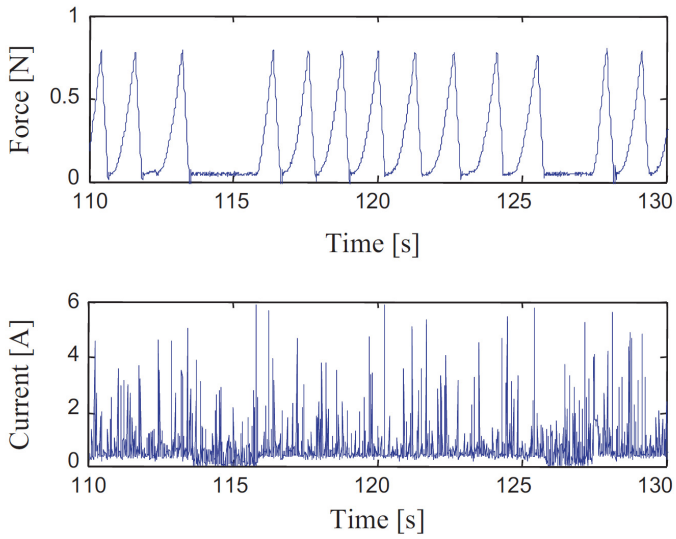

Figure 8.2: The force and current signals in function of drilling time for a hole drilled using constant-velocity feed drilling. whenever a force occurs due to tool-glass surface contact, the current shifts upwards by about 20 mA. The current shift disappears as soon as the force goes back to zero. Reprinted from (AbouZiki and Wüthrich, 2013) with permission from Elsevier.

lowering the pH beside the tool. The feasibility of this idea must be investigated as this occurs for a very short time before H^+ ions are transformed to hydrogen gas.

Chemical incorporation

The glass surface may be chemically modified as well by incorporating inside it network modifiers from the electrolytic solution. For example, if machining is conducted in potassium hydroxide (source of K^+ ions), K^+ are expected to replace Na^+ ions. In this case, hardness must increase if K^+ ions are incorporated into the surface due to the higher resulting compressive stresses.

8.3.6 Using current signal for detecting tool-work piece contact

In the frame of the research covered by this thesis, a correlation between the current signal and occurrence of forces during constant-velocity-feed drilling was observed but not further investigated for time reasons. Figure 8.2 shows the force and the corresponding current signal in function of time for 33 V machining voltage and 15 μm/s tool feed-rate. During drilling, when a force higher than 850 mN is exerted on the tool-electrode the tool is moved upwards (away from the glass surface) by 10 μm. The current signal shows that whenever a tool-glass contact occurs, the current signal is shifted upwards by about 20 mA independently

of the force amplitude while the discharge activity remains unaltered. When the tool is moved away from the glass surface, the shift disappears. A possible explanation for this observation is that the tool-glass surface contact prevents the gas film formation at the tool tip. Therefore, the tool tip acts as a second path for the current besides the gas film. More research is required to investigate if this current shift can be influenced or used to detect tool-work piece contact, similar to the case of EDM (Luo, 1997; Davis and Kauffman, 1972).

Bibliography

AbouZiki, J. D. and Wüthrich, R. Tool wear and tool thermal expansion during micro−machining by spark assisted chemical engraving. *The International Journal of Advanced Manufacturing Technology*, 61(5 - 8):481–486, 2012.

AbouZiki, J. D. and Wüthrich, R. Forces exerted on the tool-electrode during constant−feed glass micro-drilling by spark assisted chemical engraving. *International Journal of Machine Tools and Manufacture*, 73(0):47 – 54, 2013.

AbouZiki, J. D., Didar, T. F., and Wüthrich, R. Micro-texturing channel surfaces on glass with spark assisted chemical engraving. *International Journal of Machine Tools and Manufacture*, 57(0):66 – 72, 2012.

Allagui, A. *On the Electrochemical Discharges for Nanoparticles Synthesis*. PhD thesis, Montreal, Canada, 2011.

Allagui, A. and Wüthrich, R. Gas film formation time and gas film life time during electrochemical discharge phenomenon. *Electrochimica Acta*, 54(23):5336 – 5343, 2009.

Babnik, A., Petkovsek, R., and Mozina, J. Influence of laser beam image-plane position on geometry of through−holes in percussion-drilled glass using excimer laser. *Maejo International Journal of Science and Technology*, 7:48 – 59, 2013.

Baek, D. K., Ko, T. J., and Yang, S. H. Enhancement of surface quality in ultrasonic machining of glass using a sacrificing coating. *Journal of Materials Processing Technology*, 213(4):553 – 559, 2013.

Basak, I. and Ghosh, A. Mechanism of spark generation during electrochemical discharge machining: a theoretical model and experimental verification. *Journal of Materials Processing Technology*, 62(1−3):46 – 53, 1996.

Basak, I. and Ghosh, A. Mechanism of material removal in electrochemical discharge machining: a theoretical model and experimental verification. *Journal of Materials Processing Technology*, 71(3):350 – 359, 1997.

Bhattacharyya, B., Doloi, B., and Sorkhel, S. Experimental investigations into electrochemical discharge machining (ecdm) of non−conductive ceramic materials. *Journal of Materials Processing Technology*, 95(1-3):145 – 154, 1999.

Bhondwe, K., Yadava, V., and Kathiresan, G. Finite element prediction of material removal rate due to electro−chemical spark machining. *International Journal of Machine Tools and Manufacture*, 46(14):1699 – 1706, 2006.

Bu, M., Melvin, T., Ensell, G., Wilkinson, J., and Evans, A. A new masking technology for deep glass etching and its microfluidic application. *Sensors and Actuators A: Physical*, 115(2−3):476 – 482, 2004. The 17th European Conference on Solid-State Transducers.

C-P Cheng, C.-C. M. Y.-S. H. B.-H. Y., K-L Wu. Magnetic field assisted electrochemical discharge machining. *Journal of Micromechanics and Microengineering*, 20:075019, 2010.

Cao, X. D., Kim, B. H., and Chu, C. N. Micro-structuring of glass with features less than 100 mu by electrochemical discharge machining. *Precision Engineering*, 33(4):459 – 465, 2009.

Chak, S. and Venkateswara Rao, P. Trepanning of al2o3 by electro−chemical discharge machining (ecdm) process using abrasive electrode with pulsed dc supply. *International Journal of Machine Tools and Manufacture*, 47(14):2061 – 2070, 2007.

Cheng, C.-P., Wu, K.-L., Mai, C.-C., Yang, C.-K., Hsu, Y.-S., and Yan, B.-H. Study of gas film quality in electrochemical discharge machining. *International Journal of Machine Tools and Manufacture*, 50(8):689 – 697, 2010.

Choi, J., Jeon, B., and Kim, B. Chemical-assisted ultrasonic machining of glass. *Journal of Materials Processing Technology*, 191(1−3):153 – 156, 2007.

Combes, P., Massol, J., and Alvarez, P. Colored glass composition for producing glazings for use, e.g., as automobile sunroofs. the colored glass according to the invention is a soda-lime-silica glass comprising, as coloring agents, 1.4 to 4% iron oxide expressed as fe2o3 and, 2003. URL `http://www.google.ca/patents/USRE37998`. US Patent RE37,998.

Cook, N., Foote, G., Jordan, P., and Kalyani, B. Experimental studies in electro-machining. *Journal of Manufacturing Science and Engineering*, 95(4):945 – 950, 1973.

Daridon, A., Fascio, V., Lichtenberg, J., Wüthrich, R., Langen, H., Verpoorte, E., and de Rooij, N. Multi−layer microfluidic glass chips for microanalytical applications. *Fresenius Journal of Analytical Chemistry*, 371(2):261 – 269, 2001.

Davis, M. and Kauffman, H. Edm process a method and apparatus for controlling the flow rate of dielectric as a function of gap impedance, 1972. URL `http://www.google.ca/patents/US3699303`. US Patent 3,699,303.

Didar, T., Dolatabadi, A., and Wüthrich, R. Local hardness and density variation in glass substrates machined with spark assisted chemical engraving (sace). *Materials Letters*, 63 (1):51 – 53, 2009.

Egashira, K. and Masuzawa, T. Microultrasonic machining by the application of workpiece vibration. {*CIRP*} *Annals - Manufacturing Technology*, 48(1):131 – 134, 1999.

Esashi, M., Matsumoto, Y., and Shoji, S. Absolute pressure sensors by air−tight electrical feedthrough structure. *Sensors and Actuators A: Physical*, 23(1−3):1048 – 1052, 1990. Proceedings of the 5th International Conference on Solid-State Sensors and Actuators and Eurosensors III.

Evans, A., Bieberle-Hütter, A., Rupp, J., and Gauckler, L. Review on microfabricated micro−solid oxide fuel cell membranes. *Journal of Power Sources*, 194(1):119 – 129, 2009.

Fascio, V. *Etude de la microstructuration du verre par etincelage assiste par attaque chimique: une approche electrochimique*. PhD thesis, Lausanne, Switzerland, 2002.

Fascio, V., Wüthrich, R., Viquerat, D., and Langen, H. 3d microstructuring of glass using electrochemical discharge machining {ECDM}. pages 179 – 183, Nagoya, 1999. Micromechatronics and Human Science, Proceedings of 1999 International Symposium.

Fascio, V., Wüthrich, R., and Bleuler, H. Spark assisted chemical engraving in the light of electrochemistry. *Electrochimica Acta*, 49(22-23):3997 – 4003, 2004. The role of electrochemistry in the sustained development of modern societies.

Gautam, N. and Jain, V. Experimental investigations into {ECSD} process using various tool kinematics. *International Journal of Machine Tools and Manufacture*, 38(1−2):15 – 27, 1998.

Ghorbani, Z. A study on gas evolving electrodes under extreme current densities. Master's thesis, Montreal, Canada, 2012.

Ghosh, A. Electrochemical discharge machining: principle and possibilities. *Sadhana*, 22 (3):435 – 447, 1997.

Han, M.-S., Min, B.-K., and Lee, S. J. Improvement of surface integrity of electro−chemical discharge machining process using powder-mixed electrolyte. *Journal of Materials Processing Technology*, 191(1-3):224 – 227, 2007.

Han, M.-S., Min, B.-K., and Lee, S. J. Geometric improvement of electrochemical discharge micro-drilling using an ultrasonic-vibrated electrolyte. *Journal of Micromechanics and Microengineering*, 19(6):065004, 2009.

Han, M., Min, B.-K., and Lee, S. Micro−electrochemical discharge cutting of glass using a surface-textured tool. {*CIRP*} *Journal of Manufacturing Science and Technology*, 4(4): 362 – 369, 2011.

Henein, S. *Conception des structures articulées a guidages flexibles de haute précision*. PhD thesis, Lausanne, Switzerland, 2000.

Jain, V. and Adhikary, S. On the mechanism of material removal in electrochemical spark machining of quartz under different polarity conditions. *Journal of Materials Processing Technology*, 200(1-3):460 – 470, 2008.

Jain, V., Rajurkar, K., Sreenivasa Rao, P., and Choudhary, S. Experimental investigations into traveling wire electrochemical spark machining (tw-ecsm) of composites. *Journal of Manufacturing Science and Engineering*, 113(1):75 – 84, 1991.

Jain, V., Dixit, P., and Pandey, P. On the analysis of the electrochemical spark machining process. *International Journal of Machine Tools and Manufacture*, 39(1):165 – 186, 1999.

Jain, V., Choudhury, S., and Ramesh, K. On the machining of alumina and glass. *International Journal of Machine Tools and Manufacture*, 42(11):1269 – 1276, 2002.

Jalali, M., Maillard, P., and Wüthrich, R. Toward a better understanding of glass gravity-feed micro-hole drilling with electrochemical discharges. *Journal of Micromechanics and Microengineering*, 19(4):045001, 2009.

Jiang, B., Lan, S., Ni, J., and Zhang, Z. Experimental investigation of spark generation in electrochemical discharge machining of non−conducting materials. *Journal of Materials Processing Technology*, 214(4):892 – 898, 2014.

Jui, S. K., Kamaraj, A. B., and Sundaram, M. M. High aspect ratio micromachining of glass by electrochemical discharge machining (ecdm). *Journal of Manufacturing Processes*, 15 (4):460 – 466, 2013.

Kellogg, H. Anode effect in aqueous electrolysis. *Journal of Electrochemical Society*, 97:133 – 142, 1950.

Khan Malek, C., Robert, L., Boy, J.-J., and Blind, P. Deep microstructuring in glass for microfluidic applications. *Microsystem Technologies*, 13(5−6):447 – 453, 2007.

Kim, D.-J., Ahn, Y., Lee, S.-H., and Kim, Y.-K. Voltage pulse frequency and duty ratio effects in an electrochemical discharge microdrilling process of pyrex glass. *International Journal of Machine Tools and Manufacture*, 46(10):1064 – 1067, 2006.

Kubota, M. page 51, Tokyo, Japan, 1974. Proceedings of the International Conference on Production Engineering.

Kulkarni, A., Sharan, R., and Lal, G. An experimental study of discharge mechanism in electrochemical discharge machining. *International Journal of Machine Tools and Manufacture*, 42(10):1121 – 1127, 2002.

Kulkarni, A., Sharan, R., and Lal, G. Measurement of temperature transients in electrochemical discharge machining process. *Measurement and Control in Science and Industry*, 7:1069, 2003.

Kurafuji, H. Electrical discharge drilling of glass i. *Ann. CIRP*, 16:415 – 419, 1968.

Lal, A., Bleuler, H., and Wüthrich, R. Fabrication of metallic nanoparticles by electrochemical discharges. *Electrochemistry Communications*, 10:488–491, 2008.

Lee, E., Howard, D., Liang, E., Collins, S., and Smith, R. Removable tubing interconnects for glass-based micro−fluidic systems made using ecdm. *Journal of Micromechanics and Microengineering*, 14(4):535 – 541, 2004.

Lim, H. J., Lim, Y. M., Kim, S. H., and Kwak, Y. K. Self−aligned microtool and electrochemical discharge machining (ecdm) for ceramic materials. volume 4416, pages 348 – 353, 2001.

Luo, Y. The dependence of interspace discharge transitivity upon the gap debris in precision electrodischarge machining. *Journal of Materials Processing Technology*, 68(2):121 – 131, 1997. Processing of Advanced Materials.

Maillard, P., Despont, B., Bleuler, H., and Wüthrich, R. Geometrical characterization of micro-holes drilled in glass by gravity−feed with spark assisted chemical engraving (sace). *Journal of Micromechanics and Microengineering*, 17(7):1343, 2007.

McLellan, G. and Shand, E. *Glass engineering handbook*. McGraw−Hill, NY, USA, 1984.

Mochimaru, Y., Ota, M., and Yamaguchi, K. Micro hole processing using electro−chemical discharge machining. *Journal of Advanced Mechanical Design, Systems, and Manufacturing*, 6(6):949 – 957, 2012.

Morrison, A. Quantifying and reducing variability in spark assisted chemical engraving gravity feed drilling in glass. Master's thesis, Montreal,Canada, 2009.

Morrison, A., Rodrigues, L., and Wüthrich, R. Reducing variability in spark assisted chemical engraving gravity feed drilling of glass. In *Microsystems and Nanoelectronics Research Conference, 2008. MNRC 2008. 1st*, pages 161–164, 2008.

Moussa, M. Quality assessment and improvement on spark assisted chemical engraving gravity feed micro−drilling. Master's thesis, Montreal,Canada, 2008.

OxyChem. Oxychem caustic potash handbook, 2000. URL `http://www.oxychile.cl/ingles/`.

OxyChem. Oxychem caustic soda handbook, 2009. URL `http://www.cheresources.com/invision/uploads/images/technical database/oxycaustic.pdf`.

Panda, M. and Yadava, V. Finite element prediction of material removal rate due to traveling wire electrochemical spark machining. *The International Journal of Advanced Manufacturing Technology*, 45(5−6):506 – 520, 2009.

Panda, M. and Yadava, V. Intelligent modeling and multiobjective optimization of die sinking electrochemical spark machining process. *Materials and Manufacturing Processes*, 27(1):10 – 25, 2012.

Park, B., Choi, Y., and Chu, C. Prevention of exit crack in micro drilling of soda−lime glass. {*CIRP*} *Annals−Manufacturing Technology*, 51(1):347 – 350, 2002.

Paul, L. and Hiremath, S. S. Response surface modelling of micro holes in electrochemical discharge machining process. *Procedia Engineering*, 64(0):1395 – 1404, 2013. International Conference on Design and Manufacturing (IConDM2013).

Peng, W. and Liao, Y. Study of electrochemical discharge machining technology for slicing non−conductive brittle materials. *Journal of Materials Processing Technology*, 149(1-3): 363 – 369, 2004. 14th International Symposium on Electromachining (ISEM XIV).

Plaza, J., Lopez, M., Moreno, A., Duch, M., and Cane, C. Definition of high aspect ratio glass columns. *Sensors and Actuators A: Physical*, 105(3):305 – 310, 2003.

Posalux. URL `http://www.posalux.net/site/en`.

Reed, A. and Milgram, J. Ship wakes and their radar images. *Annual Review of Fluid Mechanics*, 34(1):469 – 502, 2002.

Reghuram, V. *Electrical and spectroscopic investigations in electrochemical discharge machining*. PhD dissertation, Indian Institute of Technology, Madras and Indian Institute of Technology, Kanpur, India, 1994.

Shiuan, L. Y. and Yang, P. W. The dependence of interspace discharge transitivity upon the gap debris in precision electrodischarge machining. *Materials Science Forum*, 505-507 (2):1207 – 1212, 2006.

Spaelter, U., Wüthrich, R., and Bleuler, H. Spark assisted chemical engraving (sace) machining haptic device for the operator. pages 657 – 660, Monpellier, France, 2005. Proceedings of the European Society for Precision Engineering and Nanotechnology conference.

Stefanescu, D. *Handbook of Force Transducers: Principles and Components*. Springer, 2011.

Thoe, T., Aspinwall, D., and Wise, M. Review on ultrasonic machining. *International Journal of Machine Tools and Manufacture*, 38(4):239 – 255, 1998.

Tokura, H., Kondoh, I., and Yoshikswa, M. Ceramic material processing by electrical discharge in electrolyte. *Journal of Materials Science*, 24(3):991–998, 1989.

Tsutsumi, C., Okano, K., and Suto, T. High quality machining of ceramics. *Journal of Materials Processing Technology*, 37(1−4):639 – 654, 1993.

Wallis, G. and Pomerantz, D. Field assisted glass-metal sealing. *Journal of Applied Physics*, 40:3946, 1969.

Wei, C., Xu, K., Ni, J., Brzezinski, A., and Hu, D. A finite element based model for electrochemical discharge machining in discharge regime. *The International Journal of Advanced Manufacturing Technology*, 54(9−12):987 – 995, 2011.

Wu, W., Rezai, P., Hsu, H., and Selvaganapathy, P. 1−materials and methods for the microfabrication of microfluidic biomedical devices. In Li, X. J. and Zhou, Y., editors, *Microfluidic Devices for Biomedical Applications*, Woodhead Publishing Series in Biomaterials, pages 3 – 62. Woodhead Publishing, 2013.

Wüthrich, R. *Spark assisted chemical engraving - A Stochastic Modelling Approach*. PhD thesis, Lausanne, Switzerland, 2003.

Wüthrich, R. *Micromachining using electrochemical discharge phenomenon*: *fundamentals and applications of spark assisted chemical engraving*. William Andrew, Norwich, NY, USA, 2009.

Wüthrich, R. and Fascio, V. Machining of non−conducting materials using electrochemical discharge phenomenon - an overview. *International Journal of Machine Tools and Manufacture*, 45(9):1095 – 1108, 2005.

Wüthrich, R. and Hof, L. The gas film in spark assisted chemical engraving *sace* a key element for micro−machining applications. *International Journal of Machine Tools and Manufacture*, 46(7-8):828 – 835, 2006.

Wüthrich, R., Fascio, V., Viquerat, D., and Langen, H. In situ measurement and micromachining of glass. pages 185 – 191, Nagoya, 1999. Micromechatronics and Human Science, Proceedings of 1999 International Symposium.

Wüthrich, R., Comninellis, C., and Bleuler, H. Bubble evolution on vertical electrodes under extreme current densities. *Electrochimica Acta*, 50(25-26):5242 – 5246, 2005a.

Wüthrich, R., Fujisaki, K., Couthy, P., Hof, L. A., and Bleuler, H. Spark assisted chemical engraving (sace) in microfactory. *Journal of Micromechanics and Microengineering*, 15 (10):276, 2005b.

Wüthrich, R., Hof, L. A., Lal, A., Fujisaki, K., Bleuler, H., Mandin, P., and Picard, G. Physical principles and miniaturization of spark assisted chemical engraving (sace). *Journal of Micromechanics and Microengineering*, 15(10):268, 2005c.

Wüthrich, R., Despont, B., Maillard, P., and Bleuler, H. Improving the material removal rate in spark-assisted chemical engraving (sace) gravity−feed micro-hole drilling by tool vibration. *Journal of Micromechanics and Microengineering*, 16(11):28 – 31, 2006a.

Wüthrich, R., Spaelter, U., and Bleuler, H. The current signal in spark-assisted chemical engraving *sace*: what does it tell us? *Journal of Micromechanics and Microengineering*, 16(4):779, 2006b.

Wüthrich, R., Spaelter, U., Wu, Y., and Bleuler, H. A systematic characterization method for gravity−feed micro−hole drilling in glass with spark assisted chemical engraving *sace*. *Journal of Micromechanics and Microengineering*, 16(9):1891, 2006c.

Yang, C.-K., Wu, K.-L., Hung, J.-C., Lee, S.-M., Lin, J.-C., and Yan, B.-H. Enhancement of ecdm efficiency and accuracy by spherical tool electrode. *International Journal of Machine Tools and Manufacture*, 51(6):528 – 535, 2011.

Yang, C., Ho, S., and Yan, B. Micro hole machining of borosilicate glass through electrochemical discharge machining *ecdm*. *Key Engineering Materials*, 196:149 – 166, 2001.

Zhang, C., Rentsch, R., and Brinksmeier, E. Advances in micro ultrasonic assisted lapping of microstructures in hard−brittle materials: a brief review and outlook. *International Journal of Machine Tools and Manufacture*, 45(7−8):881 – 890, 2005.

Zheng, Z., Su, H., Huang, F., and Yan, B. The tool geometrical shape and pulse-off time of pulse voltage effects in a pyrex glass electrochemical discharge microdrilling process. *Journal of Micromechanics and Microengineering*, 17(2):265, 2007.